Microscopic Strain Localization and Damage in Multi-phase Alloys

by

Jiyun Kang

B.S., Pohang University of Science and Technology (2013)
M.S., Pohang University of Science and Technology (2016)

Submitted to the Department of Materials Science and Engineering
in partial fulfillment of the requirements for the degree of

Doctor of Science in Materials Science and Engineering

at the

MASSACHUSETTS INSTITUTE OF TECHNOLOGY

September 2022

Author . . . .
Department of Materials Science and Engineering
August 22, 2022

Certified by . . . .
C. Cem Tasan
Thomas B. King Associate Professor of Metallurgy
Thesis Supervisor

Accepted by . . . .
Frances M. Ross
Chairman, Department Committee on Graduate Studies

Microscopic Strain Localization and Damage in Multi-phase Alloys

by

Jiyun Kang

Submitted to the Department of Materials Science and Engineering
on August 22, 2022, in partial fulfillment of the
requirements for the degree of
Doctor of Science in Materials Science and Engineering

Abstract

Identifying critical factors for microscopic strain localization and damage in multi-phase alloys is challenging. In addition to distinct phase-specific properties, extra complexities arise from a broad spectrum of morphology and spatial distribution of phases. Multiple deformation mechanisms can also occur simultaneously, which renders it difficult to spatially and temporally resolve their contributions to strain heterogeneity. In this thesis, a comprehensive correlative approach is developed to address these challenges, which utilizes *in situ* scanning electron microscopy, *in situ* synchrotron X-ray diffraction, and various mapping techniques to analyze microstructure and micro-strain evolution. We reveal the governing microstructural mechanisms that control strain localization and damage in two most widely highlighted multi-phase alloys, an (α+β) titanium alloy and (α+α'+γ) transformation-induced plasticity (TRIP)-assisted steel. This thesis focuses especially on the effects of local texture, mechanical twinning, and mechanically-induced phase transformation. First, we study the influence of local crystallographic orientation in the two-phase titanium alloy. Quantitative analyses of local strain distribution demonstrate that the boundaries surrounded by soft and hard α grains are the most prone to strain localization. Second, we explore the role of mechanical twinning in modulating strain localization mechanisms during deformation and propose its potential use to retard damage development. The last focus of the thesis is the effects of mechanically induced martensitic transformation in a multi-phase quenching and partitioning (QP) steel. Our *in situ* tracking of metastable retained austenite unravels strong influences of neighborhood microstructure on its mechanical stability and also post-transformation behaviors. Based on our findings, micromechanically-guided microstructure design strategies to better optimize properties of these alloys are discussed.

Thesis Supervisor: C. Cem Tasan
Title: Thomas B. King Associate Professor of Metallurgy

Acknowledgments

There have been many people who contributed directly to my thesis, as well as countless others who provided indirect support. Without their contributions, this thesis would have hardly been achieved.

Above all, I would like to express my deepest gratitude to my advisor, Professor C. Cem Taşan. Under Cem's supervision, I learned how to plan and carry out research and, more importantly, how to enjoy every moment of doing research. Aside from uncounted hours of discussions on my projects, I am deeply indebted to Cem for his consistent encouragements and insights in the face of failure. It is his trust that helped me believe in myself, push my limits, and overcome lots of challenges during my doctoral study. I am incredibly lucky to have had him as my supervisor, and I believe that many aspects that I learned from Cem, enthusiasm for research, rigorousness in science, and openness towards the community, will continue to inspire me during the upcoming scientific journey.

I would like to extend my sincere thanks to my committee members, Professor Lorna J. Gibson and Professor Ju Li, for always being supportive and providing thoughtful comments and suggestions at every critical milestone of my study. I especially appreciate your generous support and encouragement in the last stage of my program, which strengthened me to continue moving forward to the next steps and successfully complete this long journey.

I owe a special thanks to my previous advisors and mentors in South Korea, Professor Hyoung Seop Kim and Professor Byeong-Joo Lee at Pohang University of Science and Technology (POSTECH). Thank you for guiding me to the exciting world of Materials Science and Engineering, especially the field of metallurgy, and also for your genuine support and advice on my personal growth and academic career.

I am also grateful to my collaborators for their significant contributions to my thesis. I especially want to thank Dr. Hyun Seok Oh and Dr. Shaolou Wei for insightful discussions on strain localization mechanisms and titanium plasticity. I thank Dr. Gaoming Zhu for modeling work and Mr. Ikuho Nakahata and Dr. Onur

Güvenç for their generous help with the experiments. I also appreciate Dr. Narayan S. Pottore and Dr. Hong Zhu at ArcelorMittal for their thought-provoking suggestions and comments on the study on steel. It was such a great pleasure to work with you all, and I look forward to the next cross path in our journey of discovering new science and broadening our academic horizons.

I also would like to thank my funding sources, Kwanjeong Educational Foundation, ArcelorMittal, and TA fellowships. Your financial support was the ground of all research activities in this thesis.

I wish to express my sincere thanks to the staff members in the Department of Materials Science and Engineering, Dr. Michael J. Tarkanian, Dr. Shaymus W. Hudson, Dr. James Hunter, and Dr. Alan F. Schwartzman, for their tireless support in all parts of my daily research activities. I also thank Dr. Yong Zhang in CMSE for his kind assistance.

I thank all members of the Tasan group for being my greatest colleagues and friends. I owe a special thanks to Dr. Jinwoo Kim and Dr. Hyun Seok Oh who taught me many essential skills in the lab and also have always been very supportive and helpful. Thanks to Shaolou for always motivating, encouraging, and reassuring me whenever I was in stagnant periods. To Haoxue, Menglei, Julian, and Berk, thank you all for making my everyday life in the office and in the lab more enjoyable and cheerful. I was extremely lucky to be in such an inclusive, supportive, and hard-working group during my doctoral study.

I am also thankful to my friends, near and far, for being my source of joy and strength during my study at MIT. I especially thank Minhyeok, Doyoub, So Yeon, Jimin, Junghwa, Dongha, William, and my figure skating buddies, Andy, Jonathan, Yifan, Phillip, and Kimberly, for giving me so many fun and wonderful memories on and off the ice. I also appreciate all members and alumni of the Korean Graduate Student Association in Materials Science and Engineering (KGMSE) for their consistent efforts to create an inclusive and welcoming atmosphere among Korean students in the department. Your friendship is one of the most meaningful achievements I have made during my time at MIT.

At this moment, my warm and heartfelt thanks go to my parents, Seungheon Kang and Misuk Kim, for their unconditional, selfless, and endless love. It is your understanding and support at every step of my life that bring me to where I am today. I am very lucky and proud to be a daughter of such dedicated parents as you. I also thank my brother, Junhu Kang, and my parents-in-law, Jungryul Seo and Eunseo Park, for their unlimited love and support.

Last but not least, to my husband, Woosuk Seo, this thesis stands as a testament to your unfailing love and support. Thanks for coming into my life, cheering me on, and becoming the strongest supporter of what I have dreamed of.

Contents

List of Figures

List of Tables

Chapter 1

Introduction

1.1 Why multi-phase alloys?

As the societal demand for high-performance alloys is ever-increasing, there has been a growing need for more durable, sustainable, and cost-effective solutions to structural materials across industries. In the automotive industry, for example, the development of stronger and tougher but lighter steels for vehicles is still an active research interest [1–3]. Improving fatigue resistance and high-temperature tolerance of titanium alloys for aircraft or spacecraft is necessary to ensure safer and more reliable aviation [4–6]. In energy sectors, especially for fusion reactors, producing higher thermal creep- and radiation-resistant refractory metals is a key [7–9]. As the physical limits of mankind have been expanded towards more extreme environments, such as offshore, cryosphere, or even space, the need for advanced metals and alloys is expected to gain stronger momentum [10–13].

An essential material design strategy to meet these global demands is to produce alloys with microstructures consisting of different, mechanically contrasting phases. The mechanical performance of metals and alloys, which is commonly evaluated by strength, ductility, toughness, or fatigue resistance, is determined by their microstructures. A primary advantage of such a multi-phase microstructure design approach is its flexibility to tune and optimize combinations of these properties. By adjusting the individual properties of phases, their fractions, morphology, distributions, and interface conditions, we can broaden the spectrum of properties and eventually find the optimum property combinations that meet industrial needs. Examples of successful development and applications of such multi-phase design are profuse across industries: α/α' dual-phase (DP) steels [14–16], α'/γ or α/α'/γ transformation-induced plasticity (TRIP) assisted steels [17–19], α/β titanium alloys [20–22], and γ/γ' Ni-based superalloys [23, 24]. Some of these examples are shown in Fig. 1-1.

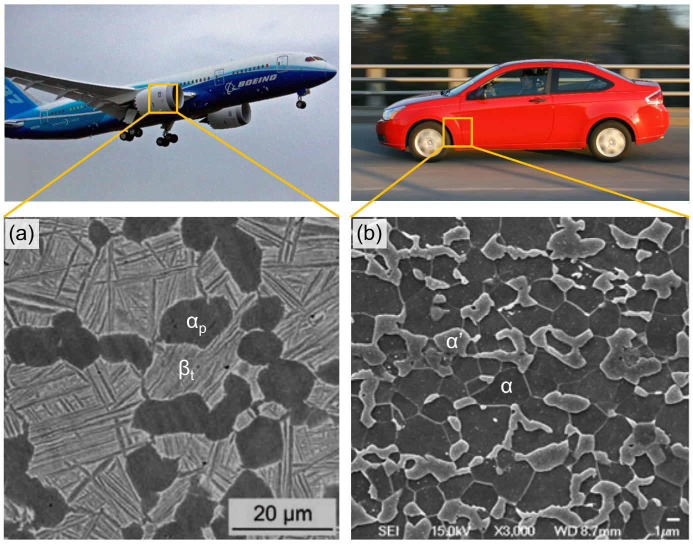

Figure 1-1: Multi-phase alloys in commercial use. (a) ($\alpha+\beta$) titanium alloy (Ti-6264) in an airplane engine (adapted from [25] (airplane) and [26] (microstructure)). (b) ($\alpha+\alpha$') dual-phase (DP) steel in a car (adapted from [27] (car) and [15] (microstructure)). The micrographs in (a) and (b) are adapted with permission granted through a license between MIT and Elsevier (https://libraries.mit.edu/scholarly/publishing/using-published-figures/) from [15, 26].

1.2 Complexities in multi-phase microstructures

Despite the enlarged property design space of multi-phase microstructures, structural complexities of such alloys also create challenges in characterizing and understanding their mechanical response. In general, the complexities in multi-phase alloys arise from the following two aspects: (i) intrinsic properties of individual phases (e.g., crystal structure, texture, or chemistry), and (ii) extrinsic factors affecting phase interactions (e.g., phase fractions, distributions, or interface characteristics).

Intrinsic or phase-specific properties determine the resistance of crystals to plastic deformation. For example, crystal structures, texture, or chemistry of individual phases can create substantial variations in the relative strengths of phases. Such mechanically distinct phases respond differently to the same macroscopically applied load, and, as a consequence, a different amount of stress or strain is partitioned into phases. Furthermore, depending on compositions and local stress states, different deformation modes, such as dislocation plasticity, mechanical twinning, or even mechanically-induced phase transformation (Fig. 1-2), can be activated simultaneously. As a result, different levels of stress are required to initiate plastic deformation locally, and disparate strain hardening behaviors are expected between phases. Temporally and spatially resolving the contributions of these plasticity mechanisms to macroscopic properties is therefore extremely challenging. Characterization of defects and their interactions often requires a high-resolution microscopy technique that is intrinsically limited in statistics.

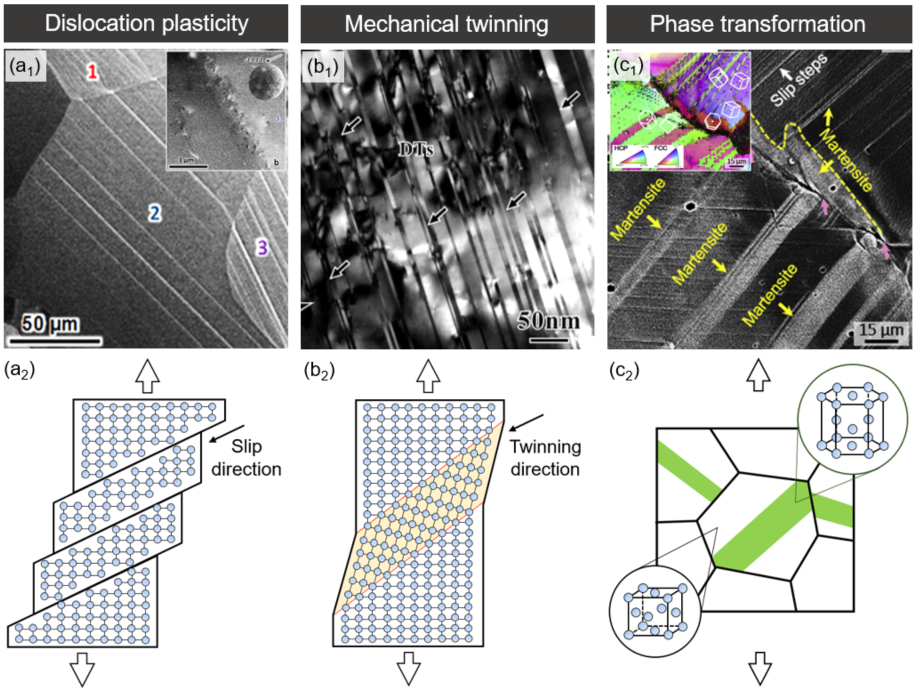

Figure 1-2: Three types of deformation mechanisms in metals. (a) Dislocation plasticity. (b) Mechanical twinning. (c) Mechanically-induced martensitic transformation. The micrographs in (a$_1$) and (c$_1$) are adapted with permission granted through a license between MIT and Elsevier (https://libraries.mit.edu/scholarly/publishing/using-published-figures/) from [28] and [29], respectively. The TEM image in (b$_1$) is adapted from [30] (open access).

In addition to the phase-specific properties, extrinsic factors such as phase morphology, fraction, distribution, or interface characteristics also play a critical role in macroscopic properties. A series of schematics in Fig. 1-3 illustrate this point, showing different types of microstructural hierarchies generated in multi-phase alloys as well as microstructural design parameters associated with each structure. Unlike a single-phase microstructure that has a limited number of controlling factors (Fig. 1-3(a)), the presence of different phases substantially extends the design space by introducing more microstructural variety such as phase strength, fraction, distribution, stability, etc. (Figs. 1-3(b-d)).

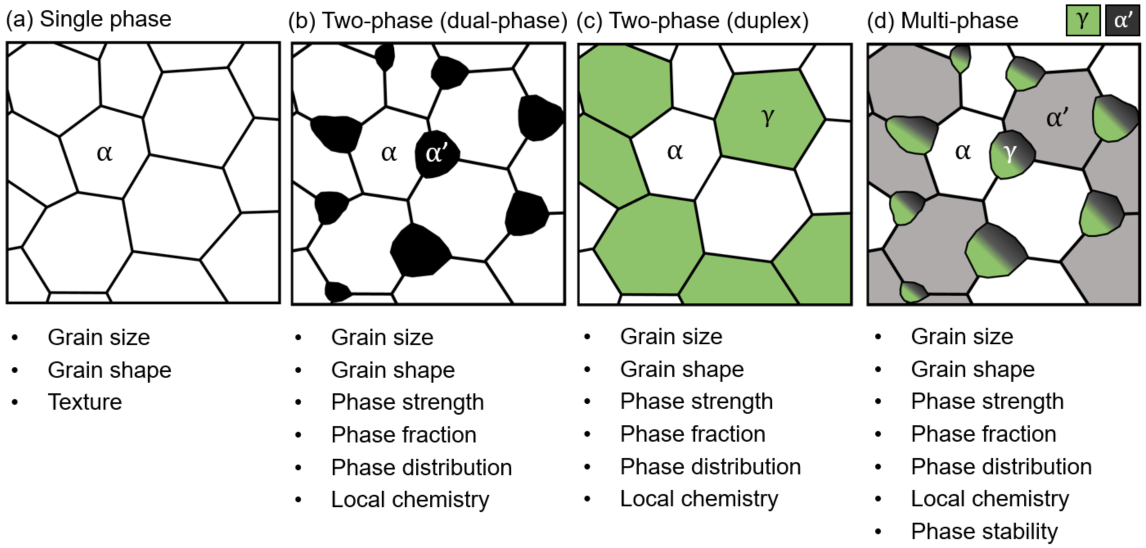

Figure 1-3: Various types of microstructural complexity. (a) Single phase microstructure. (b) Two-phase (dual-phase) microstructure. (c) Two-phase (duplex) microstructure. (d) Multi-phase microstructure with a metastable phase. Microstructural parameters that need to be considered for each type are listed underneath in respective schematics.

1.3 Microscopic strain localization and damage in multi-phase alloys

As a result of the interplay between these intrinsic and extrinsic variables, in multi-phase microstructures, upon mechanical loading, intense strain heterogeneity can develop, and strain tends to be highly localized in certain microstructural locations.

This microscopic strain localization can be differentiated from macroscopic strain localization by its length scale, as illustrated in Fig. 1-6. 1-6(a) shows strain distribution on the surface of a tensile sample, as typically observed in conventional mechanical tests. The specimen is under plastic instability at the point of image acquisition, thus showing a localized neck (macroscopic strain localization) as pointed out by an arrow. However, even before the onset of necking, from a microscopic perspective, the microstructure already undergoes a highly heterogeneous deformation (microscopic strain localization). For example, despite the homogeneous strain distribution in most of the gauge section, as highlighted by a box in Fig. 1-6(a), microscopically, severe strain heterogeneity develops between phases and even at a sub-grain level (Fig. 1-6(b)). The cumulative strain is intense in some local microstructural areas, and the amount of strain accumulated in each location depends on both intrinsic and extrinsic factors.

Furthermore, in multi-phase alloys, due to the incorporation of phases that exhibit high mechanical contrast, the risks of micro-cracking also increase. It has been commonly accepted that damage is prone to occur in the locations where severe strain incompatibility or stress intensification develops. Macroscopically, damage formation is considered as a result of high strain concentrations (Fig. 1-6(b)), but microscopically, damage nucleation correlates with deformation heterogeneity. More specifically, nucleation of damage incidents can be prohibited if the amount of local strain is sufficient to accommodate imposed geometry changes, but if the local microstructure cannot fully accommodate such shape deformation, the damage starts to nucleate [31]. Damage resistance of a multi-phase alloy is thus determined by the capacity of the microstructure to accommodate local shape deformation, and such a capacity obviously depends on both intrinsic and extrinsic microstructural parameters. With this attention, an increasing number of studies have been carried out in recent years to identify critical microstructural factors that govern strain localization mechanisms and damage evolution in different types of multi-phase microstructure.

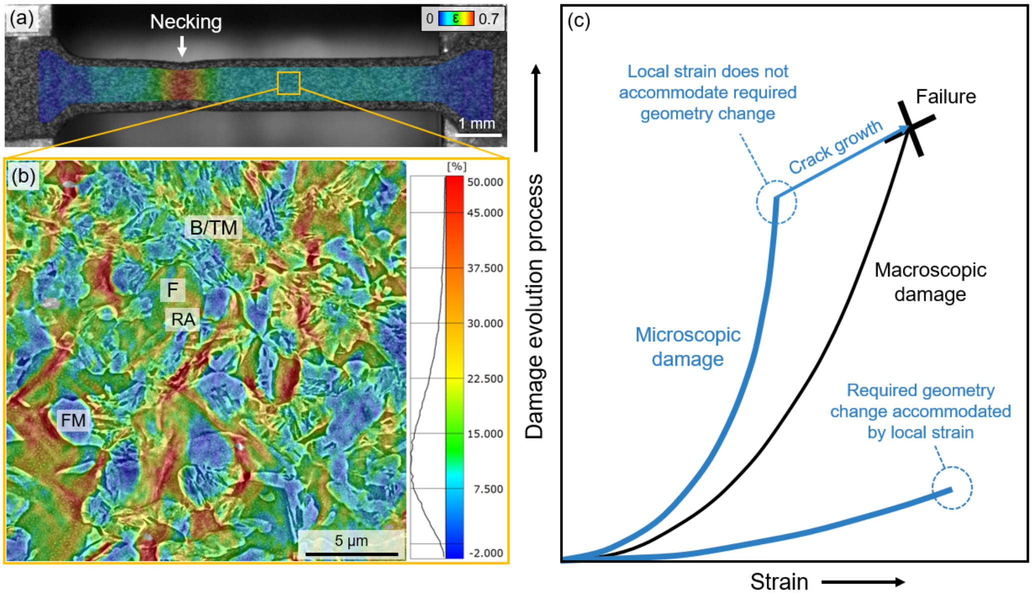

Figure 1-4: Strain localization and damage at macroscopic and microscopic scales. (a) Macroscopic strain localization observed in a tensile specimen under plastic instability. (b) Microscopic strain localization observed in a local area of the tensile specimen in (a). (c) Relationships between damage and applied strain from macroscopic and microscopic perspectives, adapted with permission granted through a license between MIT and Elsevier (https://libraries.mit.edu/scholarly/publishing/using-published-figures/) from [31].

One of the most extensively studied multi-phase alloys is dual-phase (DP) steel. DP steel has a composite-like microstructure consisting of soft ferrite (α) and hard martensite (α') phases. In this alloy, the considerable mechanical contrast between these two phase constituents is highlighted as a critical factor that determines the strain localization tendency. The effect of phase contrast on strain heterogeneity can be quantitatively evaluated by tracking the amount of local strain partitioned into each phase in the course of deformation. The latest experimental and modeling studies have demonstrated that the amount of strain partitioned into soft ferrite can be almost 10 times higher than that into hard martensite [32, 33] (Fig. 1-5(b)). The inset in Fig. 1-5(a) also shows highly localized strain inside ferrite grains. Due to the significant strain incompatibility between these two phases, micro-cracking is prone to occur at the phase interfaces [34]. Despite multiple damage micro-mechanisms that can possibly occur in this two-phase microstructure (Fig. 1-5(b)), the most dominant damage micro-mechanisms is identified as the decohesion of the ferrite-martensite interfaces [34]. However, the governing damage micro-mechanism also depends on extrinsic factors. For instance, martensite cracking can become more probable as the fraction of martensite increases [14].

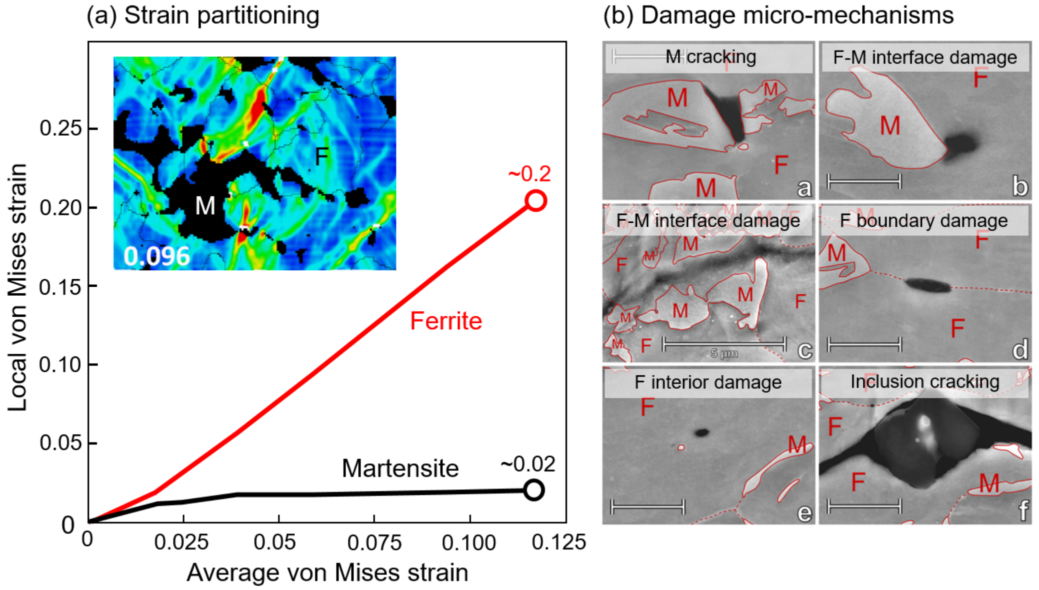
(a) Strain partitioning

(b) Damage micro-mechanisms

Figure 1-5: Strain localization and damage micro-mechanisms in DP steel. (a) Strain partitioning between ferrite (F) and martensite (M) (adapted from [35] (strain map) and [33] (plot)). (b) Various damage micro-mechanisms observed in DP steel: M cracking, F-M interface damage, F boundary damage, F interior damage, and cracking around an inclusion (adapted from [34]). The figures and plots in (a-b) are adapted with permission granted through a license between MIT and Elsevier and Springer Nature (https://libraries.mit.edu/scholarly/publishing/using-published-figures/).

1.4 Goal of this thesis

The aim of this thesis is to identify critical microstructural mechanisms that govern strain localization and damage in multi-phase alloys at a microscopic level and propose micromechanically-guided microstructure design solutions for better property optimization.

1.5 Thesis structure

By combining the *in situ* microstructure-based strain mapping technique and *in situ* synchrotron X-ray diffraction, we explore the following three effects on microscopic strain localization and damage in different multi-phase alloys: local texture (Chapter 3), mechanical twinning (Chapter 4), and phase transformation (Chapter 5).

In Chapter 2, we first introduce the experimental and analytical tools used in this thesis. Details of mechanical tests, *in situ* characterization techniques, and analysis methodologies are described.

In Chapter 3, we study the effects of local texture on strain localization and damage in a (α+β) titanium alloy. Two critical strain localization mechanisms are identified in this two-phase microstructure: (i) intragranular strain band formation in soft grains and (ii) intergranular strain localization along boundaries. Both mechanisms exhibit a strong dependence on the local crystallographic orientations of neighboring α grains. The α and β phases in general tend to co-deform, resulting in negligible difference in partitioned plastic strain between the two phases. Significant load partitioning between the two phases is observed as the deformation level increases, implicating that the phase interfaces can be a preferential site for micro-void nucleation.

In Chapter 4, we investigate the effects of mechanical twinning on strain localization and damage in a two-phase titanium alloy. Temporally and spatially varying strain localization mechanisms due to the activation and propagation of the $\{10\bar{1}2\}$ extension twins are resolved using the *in situ* microstructure-based strain mapping technique, and the potential of employing mechanical twinning to improve the damage resistance of the titanium alloy is proposed.

In Chapter 5, we explore the effects of phase transformation, especially mechanically induced martensitic transformation, on strain localization in a ferrite-containing quenching and partitioning (QP) steel. *In situ* observations show that neighborhood phases have a strong influence on both mechanical stability and post-transformation behavior of metastable retained austenite. The transformation in general mitigates strain heterogeneity between retained austenite and its surroundings, ferrite or martensitic matrix, although such co-deformability decreases in the case of retained austenite in a ferrite grain as the deformation level increases.

In Chapter 6, we summarize the main findings of this thesis and provide directions for future research.

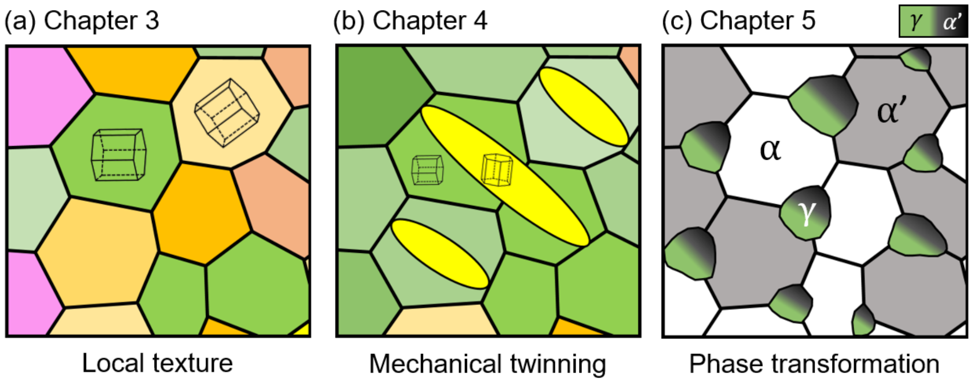

Figure 1-6: Three microstructural characteristics explored in this thesis. (a) Local texture (Chapter 3). (b) Mechanical twinning (Chapter 4). (c) Phase transformation (Chapter 5)

Chapter 2

Methodology

2.1 Mechanical testing

In Chapters 3 and 5, the room-temperature uniaxial tensile tests were performed under a quasi-static loading condition, i.e., at strain rates of 8.3×10^{-4} s^{-1} (Chapter 3) and $\sim10^{-3}$ s^{-1} (Chapter 5) in a Gatan MICROTEST2000 Uniaxial Testing Stage (Fig. 2-1(a)). The plate-type tensile specimens were machined from a bulk alloy sheet by electric discharge machining (EDM), with gauge dimensions of 1.21 mm × 1.51 mm × 8 mm (Chapter 3) and 1.21 mm × 0.68 mm × 6 mm (Chapter 5). The surfaces of the specimens were then subjected to mechanical grinding by a series of abrasive SiC papers until 800 grit. Note that for the QP steel in Chapter 5, the decarburized layers (~0.06 μm) were removed from both surfaces of the tensile sample. As shown in Fig. 2-1(b), the tensile stage was installed with an optical camera, which recorded the deformation images (~140 pixel/mm in resolution) during the tests at a fixed frame rate of 2 Hz for digital image correlation (DIC). The identical acquisition rate, i.e., a data point per 500 ms, was applied to the load measurements. The commer-

---

This chapter contains contents adapted from the following papers: 1. J. Kang et al., An *in situ* study of microstructural strain localization in an (α+β) Ti-Al-V-Fe-Si-O alloy, *Under revision*, 2022., and 2. J. Kang et al., Neighborhood effects on mechanically induced martensitic transformation: An *in situ* investigation in a ferrite-containing QP steel, *Submitted*, 2022.

cially available GOM Correlate software (https://www.gom.com/en/products/gom-suite/gom-correlate-pro) was employed to calculate the engineering strain and surface strain distribution from the deformation images with the spatial resolution of ∼0.2 mm (∼30 pixels) facet size and ∼0.1 mm (∼15 pixels) facet distance. The engineering strain was measured by the change in the distance between two points in the gauge during the deformation. Fig. 2-1(c) shows an example of an optical image of a tensile sample in the necking process, and the strain profile exported from the dashed line drawn on the specimen surface.

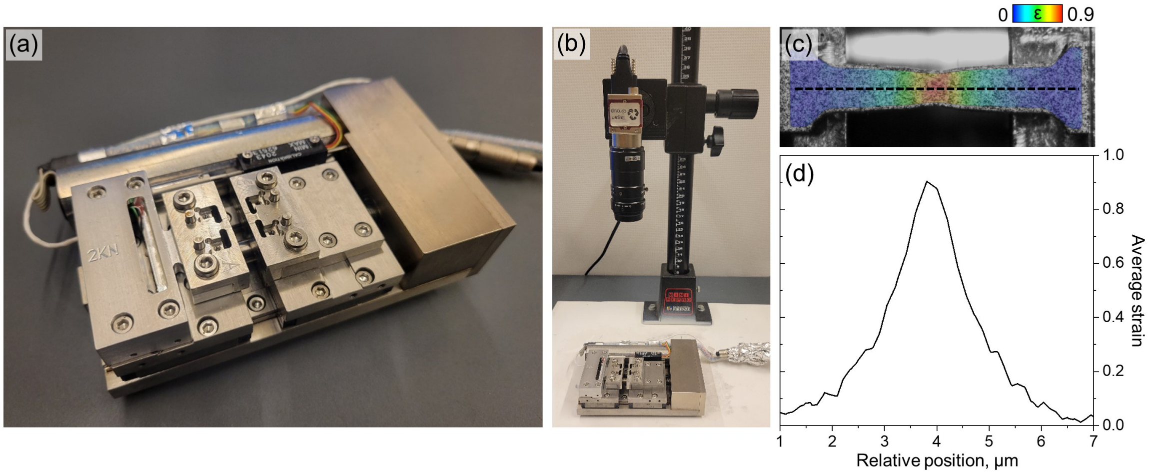

Figure 2-1: Deformation stage and exemplary strain profile across the gauge calculated by optical DIC. (a) Gatan MICROTEST2000 Uniaxial Testing Stage. (b) Tensile stage coupled with an optical camera (on the top) for DIC. (c) Tensile specimen under plastic instability. (d) Local strain profile exported from the horizontal dashed line highlighted on the sample surface in (c).

2.2 Microstructure characterization

Most of the microstructural characterization in this thesis was performed on a TESCAN MIRA3 scanning electron microscope (SEM) equipped with the EDAX/TSL system. Mirror-finish specimens were prepared by conventional metallographic sample preparation procedures of grinding and polishing up to the final polishing step using 40 nm SiO_2 colloidal sillica particle suspension (OPS). The polished samples were then subjected to ultrasonic cleaning in acetone or isopropanol bath. All electron backscatter diffraction (EBSD) measurements included in the thesis were performed using the following imaging parameters: 20 kV acceleration voltage, 20 beam intensity, and 60-80 nm step size. The acquired EBSD data were post-processed in Orientation Imaging Microscopy (OIM) software to extract microstructural information such as grain size, phase distribution and fraction, crystallographic orientation, *etc.*

In Chapter 5, Mn segregation in retained austenite was investigated using energy-dispersive X-ray spectroscopy (EDS) in Zeiss Merlin High-resolution SEM equipped with the Octane Elect Super EDS system (EDAX, AMETEK, Inc.), employing 15 kV acceleration voltage, 1 nA probe current, 8.5-9 mm working distance, and 0.96 µs amp time which provided more than 50000 counts per second (CPS). For point measurements, the acquisition time was 20 seconds, and for linescans, 512 data acquisition points (or pixels) were created across a 3 µm line whose width was 1 µm. 32 frames were acquired in each line with 25 ms dwell time, which resulted in the approximate scanning time of 6 minutes and 30 seconds per line.

2.3 *In situ* microstructure-based digital image correlation (µ-DIC)

Sample preparation

An *in situ* SEM-based microscopic-digital image correlation (µ-DIC) was employed to probe into the micromechanical origins of strain localization and damage in multi-phase microstructure. The experimental details of such microstructure-based strain mapping technique and its applications have been well-documented and can be found in the references [29, 34, 36–39]. In all of the *in situ* SEM experiments in the thesis, the following sample preparation methods were applied. Hourglass-shaped tensile specimens with a curved gauge geometry (shown in Fig. 2-2) were machined by EDM, followed by standard mechanical grinding and polishing procedures with a final polishing step with OPS. The specimens employed in Chapters 3 and 5 were lightly etched after the final polishing to facilitate phase boundary detection. The titanium specimen studied in Chapter 3, for instance, was etched with the Kroll's reagent (94.3 vol.% H_2O, 1.9 vol.% HF, and 3.8 vol.% HNO_3) for five seconds and then slightly re-polished with OPS for 10 seconds to improve the exposure of phase boundaries as well as to minimize topological contrast resulting from etching. The QP steel sample in Chapter 5 was etched with a 3% Nital etchant (3% vol.% HNO_3 acid in CH_3OH) for four seconds.

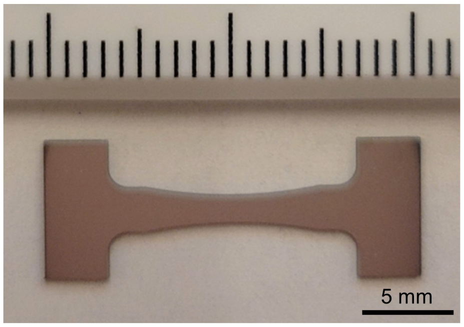

Figure 2-2: Geometry of the round-neck-shaped tensile specimen for the in situ SEM experiments in the thesis. The smallest graduation in the ruler is 1 mm.

A speckled pattern for µ-DIC was generated on the surface using non-crystalline SiO_2 nanoparticles with an average size of $\sim$40 nm. To homogeneously spread the particles, the following procedures were employed. First, the sample was polished for five seconds on the final polishing pad (Chemomet, Buehler, item No. 424010) where several droplets of diluted OPS solution (20 vol.% OPS solution in distilled water) were distributed. Next, the sample was washed with water for three seconds and isopropanol for three seconds using wash bottles with gentle pressure, and then dried in air. The exemplary speckle pattern generated by this methodology is provided in Fig. 2-3 in the two-phase titanium alloy studied in Chapter 3.

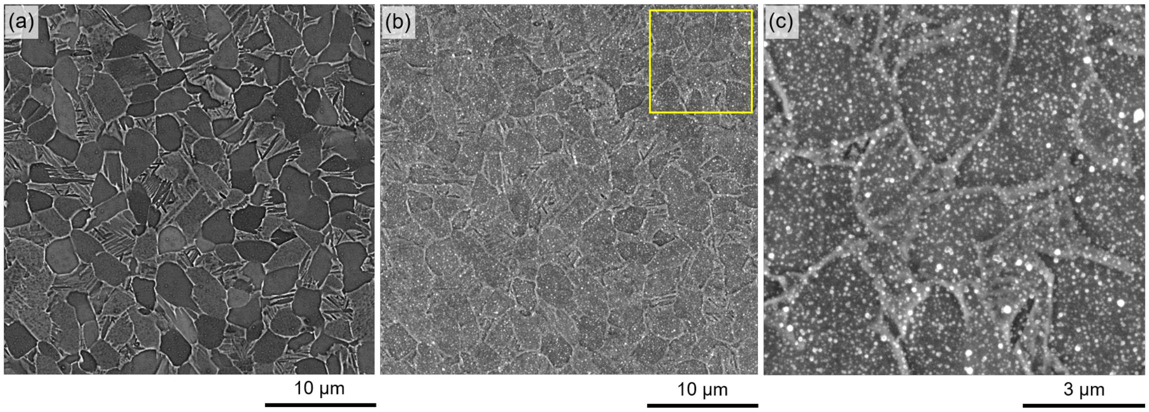

Figure 2-3: Stochastic speckle patterns of SiO_2 particles for microstructure-based digital image correlation (µ-DIC). (a) BSE micrograph of the as-received microstructure of the (α+β) titanium alloy (Chapter 3) where the *in situ* SEM characterization was carried out. (b) In-beam SE micrograph of the same area as (a). (c) Magnified in-beam SE image in the region inside the yellow box in (b) showing homogeneous SiO_2 particle distribution.

Imaging conditions

The *in situ* tensile test was carried out using a Gatan MICROTEST2000 Uniaxial Testing Stage installed inside the TESCAN MIRA3 scanning electron microscope (SEM), as shown in Fig. 2-4. A 30-minute plasma cleaning was carried out before imaging to remove hydrocarbon contamination. For SE/BSE imaging, the following beam conditions were adopted: 8-9 kV acceleration voltage, ∼13 beam intensity, and 9 mm working distance. The high-resolution SE, BSE, and in-beam SE images of 4096 × 4096 in pixel (50 × 50 μm^2) were recorded at different deformation steps. In Chapters 4 and 5 where metastability effects were investigated, the EBSD measurements were performed at every deformation step to keep track of the occurrence of mechanical twinning (Chapter 4) and phase transformation (Chapter 5). All EBSD measurements during the *in situ* experiments were carried out under the following imaging parameters: 20 kV acceleration voltage, 20 beam intensity, 18 mm working distance, and 60-80 nm step size. The local strain maps of each deformation step were calculated by correlating a series of in-beam SE images in GOM Correlate software (https://www.gom.com/en/products/gom-suite/gom-correlate-pro).

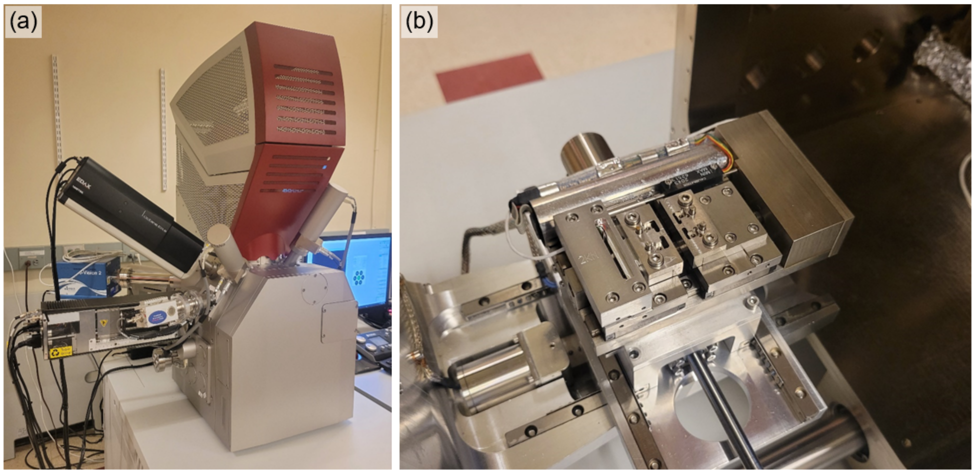

Figure 2-4: Tensile stage installation for *in situ* SEM/EBSD characterization. (a) TESCAN MIRA3 scanning electron microscope (SEM) equipped with an EBSD detector. (b) Gatan MICROTEST2000 Uniaxial Testing Stage installed inside the SEM chamber.

Strain definition

A substantial part of the strain analyses performed in the thesis correlates local strain partitioned across microstructural constituents to macroscopically applied strain. The terminologies of the strains employed in the analyses include engineering strain ($\varepsilon_{\mathrm{eng}}$), local strain ($\varepsilon_{\mathrm{local}}$), and average strain ($\varepsilon_{\mathrm{avg}}$). The engineering strain, is the global, macroscopically applied strain along a tensile direction, calculated by the two-point distance measurement in the optical DIC. The local strain is the micro-level strain calculated from the µ-DIC analysis. The average strain is the mean value of the local strain histogram at each step of deformation, representing the average deformation level of the microstructural patch monitored during the *in situ* SEM characterization. The quantitative strain analyses employed the two types of representative strains: (i) equivalent von Mises strain ($\varepsilon_{\mathrm{local,vM}}$ or $\varepsilon_{\mathrm{avg,vM}}$) and (ii) the strain component along the tensile axis ($\varepsilon_{\mathrm{local,xx}}$ or $\varepsilon_{\mathrm{avg,xx}}$).

2.4 *In situ* synchrotron X-ray diffraction (SXRD)

In Chapters 3 and 5, *in situ* synchrotron X-ray diffraction (SXRD) tensile testing was carried out to examine the mechanical responses of each phase to tensile loading. The tests were performed in a beamline 11-ID-C at the Argon National Laboratory, Chicago, USA. The beam at a wavelength of 0.1173 Å was irradiated on the surface of the tensile sample being deformed at a constant strain rate of 10^{-3} s^{-1}. The experimental configuration of this beamline is schematically shown in Fig. 2-5(a). The beam size was 0.5 mm × 0.5 mm, and the diffraction images were recorded at a constant time interval, by a Perkin Elmer XRD1621 amorphous silicon large-area detector with the image size of 2048 × 2048 in pixel and a pixel size of 200 µm × 200 µm. The detector was placed approximately 1600 mm from the specimen. At each step, 100 frames were collected with 0.1 second exposure time and summed to achieve high-quality diffraction pattern. The CeO_2 standard was employed as a calibrant of instrument parameters.

2.4.1 Lattice strain and phase stress calculation

For the lattice strain and phase stress calculation, the positions of the diffraction peaks need to be exported. To achieve the peak positions, the two-dimensional X-ray diffractograms were first segmented using the software program FIT2D [40]. The 1-D diffraction profiles were then obtained by integrating five degrees of the diffraction rings along the longitudinal (LD) and transverse (TD) directions (i.e., from 2.5 to +2.5 degrees around the each direction), as shown in Figs. 2-5(b-c). The positions of the diffraction peaks were extracted by Gaussian peak fitting of these 1-D diffraction profiles. The lattice strains were calculated by the peak positions, and the phase stresses were calculated from the lattice strains and corresponding elastic constants using the von Mises effective stress [41–44] under the isotropic elasticity assumption as described below.

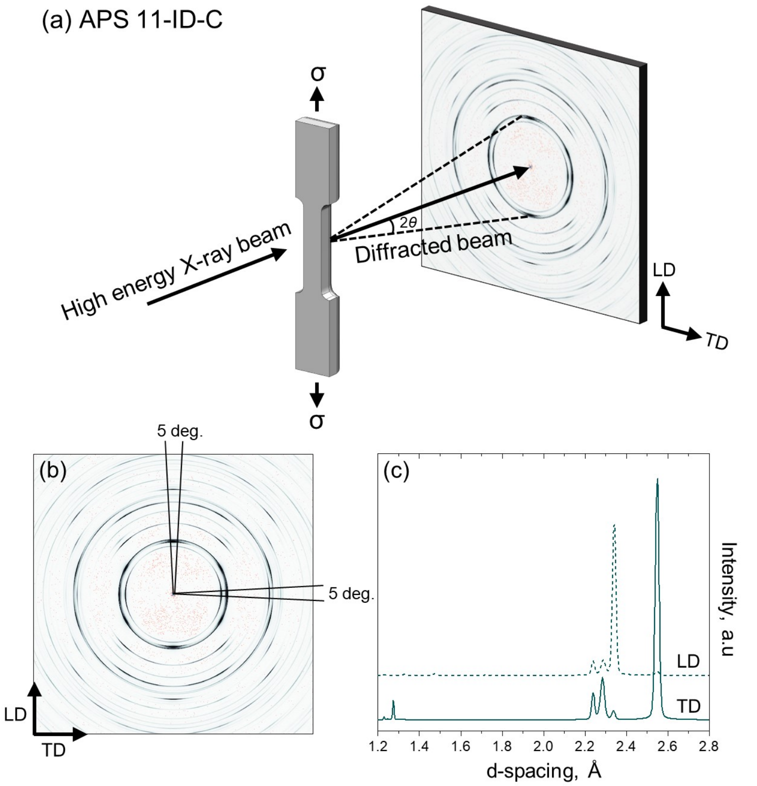

Figure 2-5: *In situ* synchrotron x-ray diffraction (SXRD) experimentation. (a) Configuration of the *in situ* testing in a beamline 11-ID-C at the Argon National Laboratory, Chicago, USA. (b) Two-dimensional diffractograms of the titanium alloy at an undeformed state (Chapter 3). (b) Diffraction profiles along longitudinal direction (LD) and transverse direction (TD) integrated from (b). The loading axis is parallel to LD.

The inter-planar spacing of an (hkl) lattice plane was achieved by diffraction peak fitting using the Gaussian function, and the lattice strain, $\varepsilon^{\mathrm{hkl}}$, was calculated by the following equation:

$$\varepsilon^{hkl} = \frac{d^{hkl} - d_0^{hkl}}{d_0^{hkl}} \tag{2.1}$$

where d_0^{hkl} is an inter-planar spacing measured at the unstrained state, and d^{hkl} is the one obtained at a deformed state. The principal strains and stresses of each plane were calculated from the lattice strains as follows [41]:

$$\varepsilon_1^{hkl} = \varepsilon_3^{hkl} = \varepsilon_{TD}^{hkl} \tag{2.2}$$

$$\varepsilon_2^{hkl} = \varepsilon_{LD}^{hkl} \tag{2.3}$$

$$\sigma_1^{hkl} = \sigma_3^{hkl} = \frac{E^{hkl}}{(1+\nu^{hkl})}\varepsilon_1^{hkl} + \frac{\nu^{hkl}E^{hkl}}{(1+\nu^{hkl})(1-2\nu^{hkl})}(\varepsilon_1^{hkl}+\varepsilon_2^{hkl}+\varepsilon_3^{hkl}) \tag{2.4}$$

$$\sigma_2^{hkl} = \frac{E^{hkl}}{(1+\nu^{hkl})}\varepsilon_2^{hkl} + \frac{\nu^{hkl}E^{hkl}}{(1+\nu^{hkl})(1-2\nu^{hkl})}(\varepsilon_1^{hkl}+\varepsilon_2^{hkl}+\varepsilon_3^{hkl}) \tag{2.5}$$

where σ_1^{hkl} and σ_3^{hkl} correspond to the principal stresses in the TD, and σ_2^{hkl} represents the principal stress in the LD. E^{hkl} and ν^{hkl} is the diffraction elastic constants calculated from each reflection by measuring the slope of the elastic region of engineering stress-lattice strain plots. The von Mises effective stress of {hkl} plane, σ_{eff}^{hkl}, can be calculated from the principal stresses as shown in Eq. 2.6.

$$\sigma_{eff}^{hkl} = \frac{1}{\sqrt{2}}\left[(\sigma_1^{hkl}-\sigma_2^{hkl})^2 + (\sigma_2^{hkl}-\sigma_3^{hkl})^2 + (\sigma_3^{hkl}-\sigma_1^{hkl})^2\right]^{\frac{1}{2}} \tag{2.6}$$

2.4.2 Phase fraction calculation

For Chapter 5, the evolution of the volume fraction of metastable retained austenite as a function of applied stress and strain was calculated by Rietvald refinement using Material Analysis Using Diffraction (MAUD) software [45,46]. The two-dimensional diffractograms were segmented by five degrees and then converted into 72 one-dimensional profiles. These individual 72 profiles were imported to MAUD through ImageJ plugin [47] and were simultaneously fitted with a pseudo-Voigt function in the software. The analysis assumes that the c/a ratio of the body-centered tetragonal (BCT) martensite is close to unity, and therefore ferrite, tempered martensite, and fresh martensite share the same lattice parameter ($a_{\alpha/\alpha'}$). Four body-centered cubic (BCC) peaks, e.g., α(110), α(200), α(211), and, α(220), and five face-centered cubic (FCC) peaks, e.g., γ(111), γ(200), γ(220), γ(311), and γ(222), were subjected to the refinement. Radial diffraction in the diamond anvil cell (rDAC) [48] was employed to fit the sinusoidal oscillations in the diffraction peak positions arising from the anisotropic elastic strain imposed during the deformation. The Delft model [49,50] and isotropic crystallite size and microstrain was applied as the line broadening model, and E-WIMV (Extended WIMV) algorithms [51] were adopted for the texture model. An example of the fitting results is provided in Fig. 2-6.

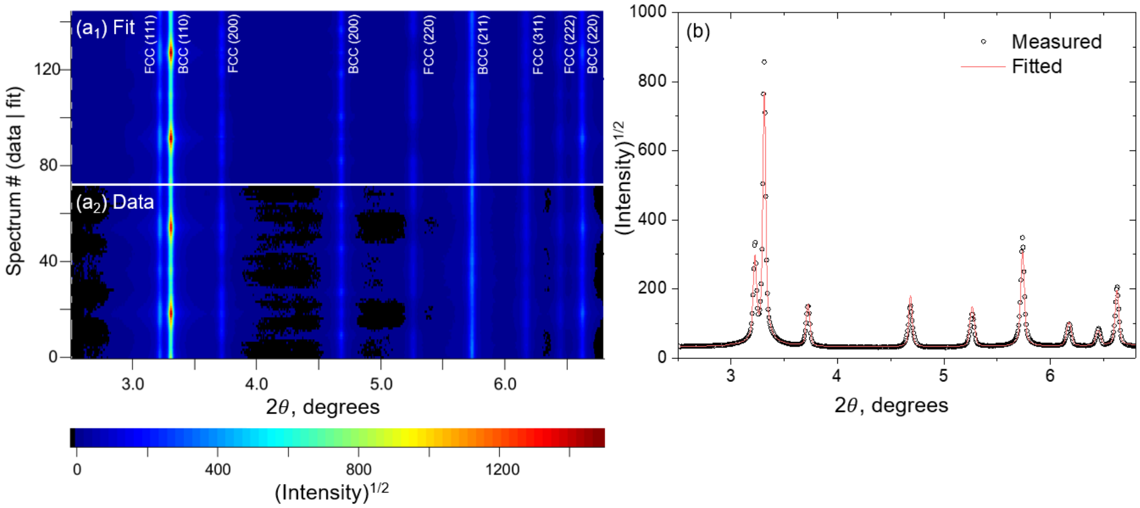

Figure 2-6: Rietvald refinement result of the QP steel at a load-free state (Chapter 5). (a_1) fitted and (a_2) measured data. (b) Integrated diffraction profile.

2.5 Nanoindentation

In Chapters 3 and 5, nanoindentation was performed to investigate how the mechanical contrast between phases influences strain localization. The indentation measurements were carried out on the as-polished surface of initial microstructure using the accelerated property mapping (XPM) mode in a Hysitron TI950 TriboIndenter (Bruker company) with a diamond Berkovich tip (1140 GPa modulus, 0.07 Poisson's ratio). The sample surface was prepared to be mirror-like to minimize surface roughness effects, by final polishing with the 40 nm SiO_2 particle suspension. With 150 µN maximum load, a trapezoid load cycle (loading for 0.1 s, holding for 0.1 s at a peak load, and unloading for 0.1 s) was employed for the indentation. Three to four grids of 22 × 22 indents were produced, and the spacing of the indents in each grid was set to 400 nm, which is roughly 10 times higher than the estimated maximum indentation depth, to minimize the overlap of the plastic zones created by each indentation event. Nanohardness values were calculated from each load-displacement curve by employing the Oliver-Pharr method [52] implemented in the Hysitron software package. The tip area function was calibrated on fused quartz (72 GPa modulus, 0.17 Poisson's ratio) before the indentation using the following equation:

$$A = C_0 {h_c}^2 + C_1 h_c + C_2 {h_c}^{1/2} + C_3 {h_c}^{1/4} + C_4 {h_c}^{1/8} + C_5 {h_c}^{1/16} \tag{2.7}$$

Where A is the contact area, h_c is the contact depth, and $C_{i(i=0,...,5)}$ are the calibration parameters of the area function.

After indentation, the areas where the indentation was carried out were characterized by BSE and EBSD to correlate the measured nanohardness values with grain or phase information, as shown in Fig. 2-7. The indents located inside grains were considered for the statistics to avoid the boundary effects on the nanohardness values. For example, the QP steel studied in Chapter 5, after excluding the indents at the boundaries, the number of indents included in the nanohardness statistics corresponds to 389 for ferrite, 252 for tempered martensite, 51 for fresh martensite, and 28 for retained austenite, respectively. No transformation of retained austenite was observed after the indentation within the resolution of EBSD.

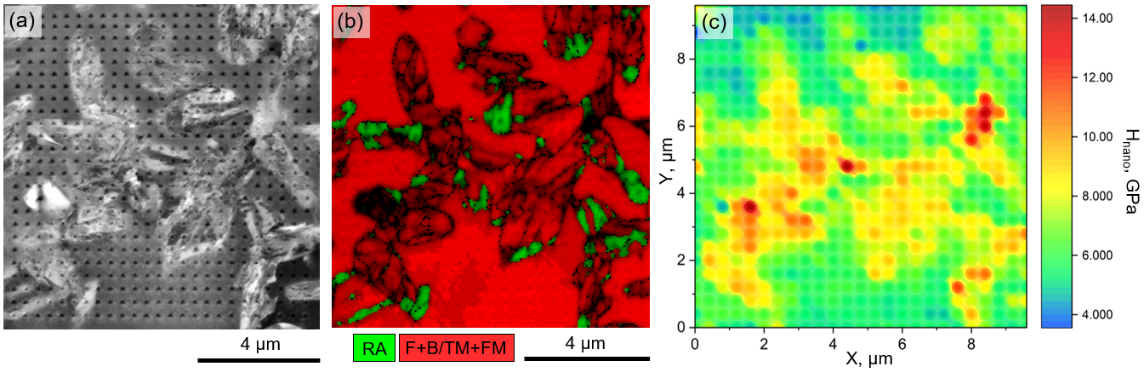

Figure 2-7: Correlation of phase information and nanohardness. (a) BSE micrograph showing a grid of indents produced in as-recieved microstructure of QP steel (Chapter 5). (b) EBSD and (c) hardness maps corresponding to the area (a).

2.6 Damage quantification

In Chapters 3 and 4, the evolution of damage as a function of applied strain was quantitatively evaluated. In this analysis, the cross-section of a fractured tensile specimen where the average strain levels across its gauge were well-defined by optical DIC performed beforehand was polished and subjected to SEM characterization, as shown in Figs. 2-8(a-b). Cross-sectional micrographs were recorded at different strain levels (Fig. 2-8(c_1-c_3)), and the damage incidents were identified by ImageJ based on contrast difference (Fig. 2-8(d)). The number density and the area fraction were calculated at each strain level, and then by dividing the area fraction by the number density, the average size of the bulk damage incidents was achieved (Fig. 2-8(e)).

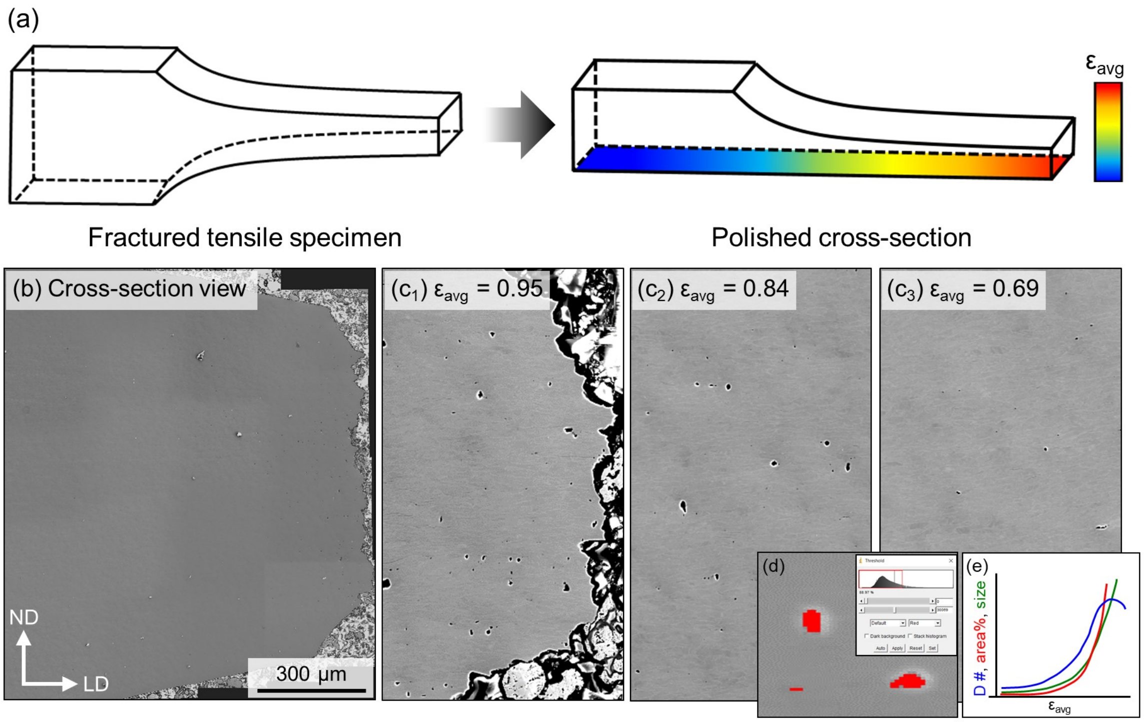

Figure 2-8: Damage detection procedures using ImageJ. (a) Fractured tensile specimen having well-defined average strain (ε_{avg}) across the gauge. The cross-section of the fractured tensile bar is polished for SE imaging. (b) Large field-of-view SE image of the cross-section of the fractured tensile specimen of a two-phase titanium alloy (Chapter 3). The loading direction (LD) is horizontal, and the normal direction (ND) is perpendicular to the direction of the sample surface. (c_1-c_3) SE images of the cross-section of the specimen at different strain levels. (d) Contrast-based damage detection performed in ImageJ. (e) Schematic plot of calculated damage number density (i.e., D#), damage area fraction (i.e., area%), and average damage size (i.e., size).

Chapter 3

Local texture effects

In low-symmetry crystal systems, such as in hexagonal-close packed (HCP) structured metals, local crystallographic orientation plays an important role in determining which deformation modules to be activated, and thus governs plastic strain localization. In this study, the critical microstructural factors responsible for microscopic strain localization are systematically analyzed for an (α+β) alloy by *in situ* microstructure-based digital image correlation (μ-DIC), *in situ* synchrotron X-ray diffraction (SXRD), and statistical analyses of strain localization incidents. The uniaxial tension tests reveal strain localization (i) across favorably oriented adjacent α grains (multi-grain strain localization) and (ii) along grain/phase boundaries (boundary strain localization), both of which suggest the strong influence of local texture on strain heterogeneity. The boundaries shared by soft and hard α grains are observed to be highly susceptible to strain localization, although ductile damage mechanisms are mostly delayed until the late stages of necking. While the majority of the (α+β) microstructure can co-deform to high strain levels without significant ductile damage evolution, nucleation, growth, and coalescence of micro-voids eventually occur at the α/β phase interfaces. The insights provided in this study highlight the importance of local texture on strain localization and damage in (α+β) Ti alloys.

This chapter contains contents adapted from J. Kang et al., An *in situ* study of microstructural strain localization in an (α+β) Ti-Al-V-Fe-Si-O alloy, *Under revision*, 2022.

3.1 Introduction

(α+β) titanium (Ti) alloys can exhibit a wide range of microstructures and mechanical property combinations, enabling a broad spectrum of engineering applications [5, 21, 53–58]. Microstructure dependence of (α+β) Ti alloy behavior has been commonly investigated in the literature, looking into the effects of phase constitution [59, 60], operating plasticity modes (e.g., dislocation plasticity, twinning, etc.) [22,61–68], and grain/phase boundary characteristics [69–78], especially to better understand failure mechanisms. Extensive experimental and computational studies have recognized that damage nucleation occurs in the microstructural regions where substantial deformation heterogeneity develops at the polycrystal [31, 79–83] or single grain [84–86] levels. An improved understanding of both inter- and intragranular strain localization processes is thus of fundamental significance in guiding alloy processing and development. In this context, α anisotropy, α local texture, and β plasticity effects require a brief re-visit, as they play a critical role in the alloy studied here.

A major phase constituent in Ti alloys, the hexagonal close-packed (HCP) structured α phase, intrinsically possesses a highly anisotropic mechanical response due to considerable variation in critical resolved shear stress (CRSS) among different slip systems [87,88]. Basal ⟨a⟩ and prism ⟨a⟩ slip systems are documented as the two easiest slip systems having low CRSS magnitudes among all HCP slip systems including pyramidal ⟨a⟩ or ⟨c+a⟩ slip [22, 89, 90]. Due to such anisotropy of HCP lattices, the misorientation between the basal plane normal, i.e., c-axis, and a loading direction is considered decisive for the incipience of plastic deformation modules in HCP crystals relative to neighboring grains. A grain having high misorientation exhibits more pronounced activity of basal and prismatic slip and is referred to as a 'soft' grain, whereas a grain having low misorientation is referred to as a 'hard' grain. Deformation twinning is also often reported in hard grains [91, 92].

For the α phase, local texture effects are discussed in the context of local slip activation [28, 93–95], plasticity transfer [74–78], and stress redistribution [96, 97].

Specifically, the local crystallographic orientation of neighboring grains plays a decisive role in controlling slip transferability of grain boundaries [98]. In case of limited slip transmission, a substantial pile-up of dislocations occurs, causing highly localized stress fields and eventually promoting micro-void nucleation at grain boundaries [69, 70, 99, 100]. It has been demonstrated by a microstructure-based strain mapping (microscopic digital image correlation or μ-DIC) technique that slip transmission across grains with preferred orientations, i.e., similarly oriented grain clusters forming micro-textured zones (MTZs), gives rise to long-range plastic strain localization [101–103]. The strong grain neighborhood influence on the redistribution of grain-resolved stresses has been also verified in commercially pure titanium (CP-Ti) through three-dimensional X-ray diffraction (3D-XRD) as well as crystal plasticity finite element (CPFE) simulations [96]. Significant stress redistribution has been also observed in Ti-6242 alloy, from soft to hard grains, which promotes basal stresses in hard grains resulting in basal facet nucleation upon fatigue loading [97]. One way to evaluate the local texture effects on strain heterogeneity is to calculate a local Taylor factor based on local kinematics [84, 85]. It represents the relative kinematic hardness of crystals, often adopted to interpret pore creation, since sharp contrast of local Taylor factors across a grain boundary can be a potential manifestation of strain incompatibility causing local stress intensification. For instance, it has been reported that the existence of adjoining hard- and soft-colony orientations can facilitate cavity creation, presumably owing to strong deformation incompatibility that develops through the mechanical constraint imposed by hard colonies and anisotropic straining by the prismatic and basal slip in soft colonies [104, 105].

The body-centered cubic (BCC) structured β phase, a minor constituent in (α+β) titanium alloys, on the other hand, exhibits moderate mechanical anisotropy, and the activation of $\{110\}\langle\bar{1}11\rangle$, $\{211\}\langle\bar{1}11\rangle$, and $\{321\}\langle\bar{1}11\rangle$ slip systems has been understood as the popular plasticity mode [106, 107]. The involvement of β phase in strain incompatibility has been evaluated mostly in the context of slip transfer across α/β phase interfaces [74–78], rather than the mechanical behavior of the β phase itself. Slip trace analyses of Ti-5Al-2.5Sn (in wt%), an equiaxed near-α titanium alloy, for instance, have shown that slip transfer across the α/β interfaces can be facilitated if the adjoining β grain has a high Schmid factor (favorable to slip) [78]. It has also been reported through micro-pillar tests and CP simulations that the β laths may not act as a critical barrier to slip transfer if its thickness is small [74, 75]. Mechanical effects of β phase on stress distribution have been studied through CPFE simulations, which reveal, for example, that the presence of β phase reduces load shedding from a soft grain to a hard grain, leading to enhanced dwell fatigue resistance [108]. The high sensitivity of β phase morphology in local yielding was also studied by micropillar tests [59].

The study aims to connect these microstructural interactions to microscopic strain localization and damage micro-mechanisms in an (α+β) Ti alloy, applying the *in situ* µ-DIC technique to a Ti-Al-V-Fe-Si-O alloy. Though such grain-to-grain level surface strain mapping has been well-documented as an effective characterization methodology to inspect heterogeneous strain evolution and subsequent damage incipience process, its intrinsic limitations should also be noted: (i) limited field-of-view, (ii) facet-size dependence on local strain calculation, and (iii) in-plane boundary condition. This study tries to overcome these shortcomings by integrating the microstructural insights acquired from *in situ* surface strain mapping, *in situ* synchrotron X-ray diffraction, and statistical analyses of strain localization and damage incidents.

3.2 Initial microstructure and mechanical property

The Ti-0.85Al-3.90V-0.25Fe-0.25Si-0.15O alloy exhibits a two-phase microstructure of hexagonal closed-packed (HCP) structured α phase and body-centered cubic (BCC) structured β phase. A backscatter electron (BSE) micrograph in Fig. 3-1(a) shows an as-received microstructure of the alloy with β phase in a brighter contrast (white). The thin β phase is preferentially located either between the boundaries of α grains or within the lamellar structures, as highlighted in the inset of Fig. 3-1(a). The thickness of β phase is 0.128 ± 0.056 µm between the granular α grains and 0.043 ± 0.014 within the lamellar structures (averaged from 40 features each). The average grain size of the α phase is 2.71 µm calculated from the statistical distribution of the area fraction.

Fig. 3-1(c) shows a one-dimensional SXRD profile fully integrated from the two-dimensional diffraction ring at a strain-free state. The lattice parameters of the phases calculated from the diffraction peaks are a_α=2.9443 Å, c_α=4.6798 Å and a_β=3.2365 Å. The c-to-a ratio (c/a) of the HCP α phase can be calculated as 1.5894 which is slightly higher than that of pure Ti (c/a=1.587) possibly due to the dissolution of alloying elements [109]. The phase fractions of this alloy correspond to ~87% of α phase and ~13% of β phase which were calculated by the contrast-based BSE image analysis of an as-polished microstructure and confirmed by the Rietveld refinement of the SXRD profile. Fig. 3-1(d) shows the $\{0001\}$, $\{10\bar{1}0\}$ and $\{10\bar{1}1\}$ pole figures of the α grains in Fig. 3-1(b).

An engineering stress-strain curve along the TD at room temperature in Fig. 3-1(e) shows that the alloy yields at 842.5 MPa, reaches an ultimate tensile strength of 853.5 MPa at $\varepsilon_{eng}\sim 0.081$, and fractures at $\varepsilon_{eng}\sim 0.17$, all of which are comparable to the previously reported values [110]. It should be noted that a subtle stress drop is observed in the stress-strain curve after yielding, approximately by 5.9 MPa, potentially due to the mechanical twinning-induced lattice reorientation [111,112]. Furthermore, the strain distribution across the gauge shown in the inset of Fig. 3-1(e) (obtained by the optical DIC) suggests that the alloy exhibits remarkable strain development during necking with the peak strain value of 0.90 before fracture.

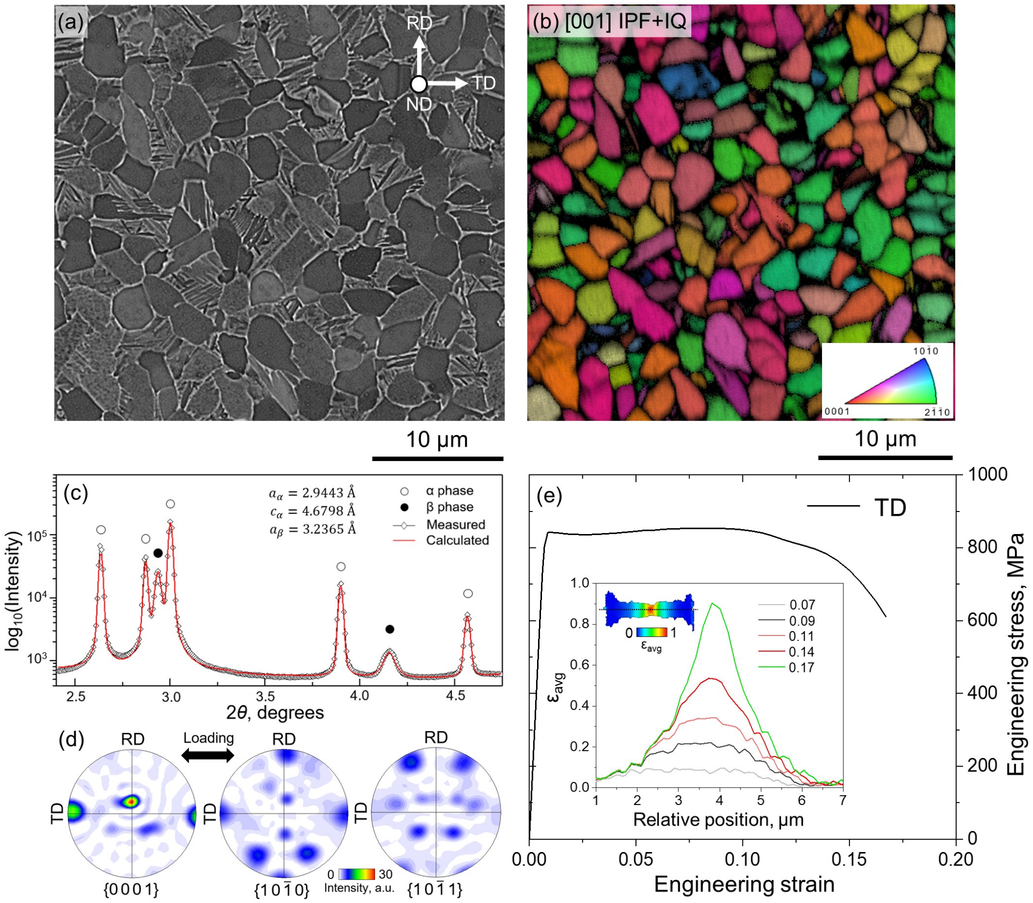

Figure 3-1: As-received microstructure and room-temperature mechanical response of the alloy. (a) BSE image of the microstructure at an undeformed state. (b) [001] IPF+IQ map of the α phase in (a) region. (c) Synchrotron X-ray diffraction (SXRD) profile. (d) {0001}, {10$\bar{1}$0}, and {10$\bar{1}$1} pole figures of the α phase in (b). (e) Engineering stress-strain curve with the inset showing average strain (ε_{avg}) profiles with the increasing engineering (global) strain levels (ε_{eng}). Note that the average strain represents the mean strain in the local area of interest along the gauge of the tensile specimen calculated by the optical DIC.

3.3 *In situ* synchrotron X-ray diffraction

In situ SXRD tensile results enable the quantitative determination of lattice strains corresponding to different crystallographic planes as well as load partitioning trends. The diffraction Elastic moduli ($E_{(hk(i)l)}$) and Poisson's ratios ($\upsilon_{(hk(i)l)}$) adapted for the effective stress calculation are listed in Table 3.1, which are in a range comparable to the reported values [113]. Figs. 3-2(a-b) show the lattice strain evolution of the {10$\bar{1}$1}, {0002}, and {10$\bar{1}$0} planes of the α phase and the {110} plane of the β phase with the applied engineering stress and the engineering strain. The plots demonstrate that the lattice strains of both phases exhibit a linear increase at a comparable rate in the elastic regime until the onset of yielding (~842.5 MPa), which is marked as a horizontal line in Fig. 3-2(a). After yielding, in the early plasticity regime, the slopes of the lattice strains of all α and β planes decrease almost at the same strain level of $\varepsilon_{\mathrm{eng}} = 0.004$. In this regime, from $\varepsilon_{\mathrm{eng}} = 0.004$ up to $\varepsilon_{\mathrm{eng}} = 0.012$ (between the two vertical dashed lines in Figs. 3-2(b-d)), the difference in the lattice strain values observed between the studied planes, for example, between the $\beta\{110\}$ planes and the $\alpha\{10\bar{1}0\}$ planes remains below 0.5%. These observations indicate that the two phases yield almost at the same strain level, around $\varepsilon_{\mathrm{eng}} = 0.004$. The effective stresses calculated from Eqns. 3-4 (Fig. 3-2(c)) also exhibit similar trends as the lattice strains, showing no obvious difference in load-partitioning capability between the phases up to the strain level of $\varepsilon_{\mathrm{eng}} = 0.012$.

However, in the plastic regime where the engineering strain is higher than $\varepsilon_{\mathrm{eng}} = 0.012$, clear distinctions in both lattice strain and partitioned load between the two phases were observed. The lattice strains corresponding to the α planes only slightly increase, whereas the strain corresponding to the $\beta\{110\}$ planes continues to increase, beyond those of the α planes. Specifically, at the very last data point at $\varepsilon_{\mathrm{eng}} = 0.075$, the $\beta\{110\}$ lattice strain is about 1.5 times higher than that of $\alpha\{10\bar{1}0\}$, the highest among all of the α planes (Fig. 3-2(b)). The effective stress evolution also demonstrates a substantial difference in this regime; the partitioned load in the $\beta\{110\}$ planes is higher than those in the α planes (almost two times higher stress at $\varepsilon_{\mathrm{eng}} \sim 0.075$).

It should be also noted that the $\beta\{110\}$ planes also exhibit more significant peak broadening once the applied strain is beyond $\varepsilon_{\mathrm{eng}} = 0.012$, which can be seen in the rapid increase in the full width at half-maximum values (FWHM), as shown in Fig. 3-2(d). The change in FWHM becomes substantial in $\varepsilon_{\mathrm{eng}} > 0.012$ (the strain level highlighted as the vertical dashed line), leading to a greater peak broadening of more than twice as much at $\varepsilon_{\mathrm{eng}} = 0.075$ as the $\alpha\{10\bar{1}0\}$ plane (the highest among all the α planes).

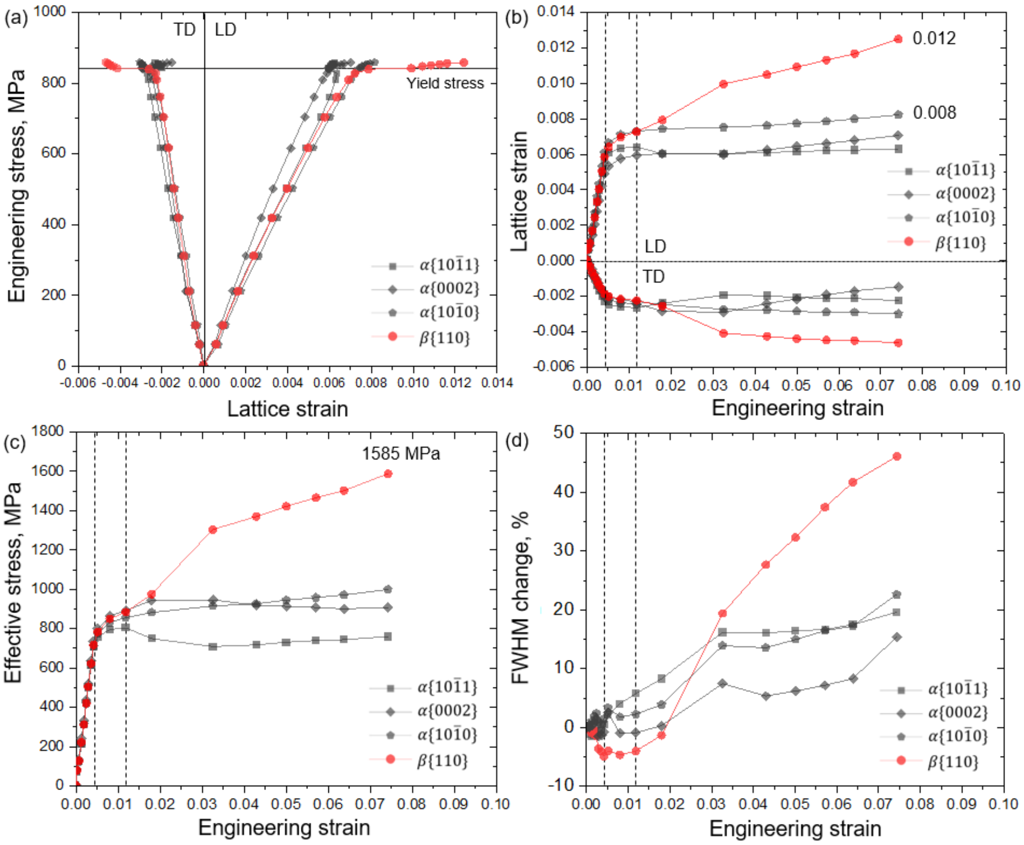

Figure 3-2: ***In situ*** **synchrotron X-ray diffraction tensile testing results.** (a-b) Lattice strain evolution in the longitudinal (positive) and transverse (negative) directions during the tensile deformation. (c) Effective stress evolution. (d) Full width at half maximum (FWHM) change of each peak over the deformation.

Table 3.1: Elastic moduli and Poisson's ratios of crystallographic planes calculated from the SXRD profiles

Plane	$\alpha\{10\bar{1}1\}$	$\alpha\{0002\}$	$\alpha\{10\bar{1}0\}$	$\beta\{110\}$
$E^{hk(i)l}$, GPa	122	144	116	119
$\nu^{hk(i)l}$	0.38	0.36	0.31	0.29

3.4 *In situ* SEM characterization

Substantial parts of this study involve quantitative assessments of local strain including the calculation of plastic strain partitioned among individual grains or phases. The strain-partitioning analyses were carried out by acquiring mean values as well as standard deviation from local strain subsets. It should be noted that local strain values calculated from DIC analysis can experience the facet size dependence, which demands the careful validation of whether the applied facet size can provide sufficient resolution for sub-grain microstructural features that give rise to heterogeneous strain distribution. In this work, the local strain maps and profiles determined by two different sets of facet size (FS) and inter-facet distance (FD), e.g., 60/20 in pixel (732/244 in nm) and 30/15 in pixel (366/183 in nm). To ensure the accuracy of local strain analyses, especially at the locations where acute strain gradients develop, the substantial parts of the local strain assessment in the present work (e.g., local strain profiles, grain/phase strain partitioning, local strain subset analyses, *etc.*) were performed adopting the reduced facet size (i.e., FS/FD: 366/183 in nm)

Indentification of strain localization incidents

In situ SEM tensile testing coupled with µ-DIC analysis was carried out on the area of interest introduced in Figs. 3-1(a-b). Figs. 3-3(a-b) are the BSE micrographs overlaid with the two-dimensional strain maps showing local strain distributions at different average strain levels, e.g., ε_{avg}=0.16 in Fig. 3-3(a) and ε_{avg}=0.28 in Fig. 3-3(b). The *in situ* microstructure strain maps in Figs. 3-3(a-b) show highly heterogeneous plastic strain patterns in terms of intensity, location, and morphology, even inside a single grain. For the strain localization analysis, the strain localization incidents were defined in the top 4% most strained subset of the strain map. 4% provides optimal representation of the strain bands since going to lower percentages reveal only the strain peaks while higher percentages render it difficult to identify individual strain bands. The analysis was carried out on the strain map obtained at ε_{avg}=0.16 (Fig. 3-3(a)), and this criterion corresponds to the strain subset with $\varepsilon_{local} \geqq 0.28$ at this deformation step. The identified 42 incidents are illustrated in Fig. 3-3(c) on top of the BSE image, showing that a major portion of the strain localization incidents possess elongated ('band-like') morphology.

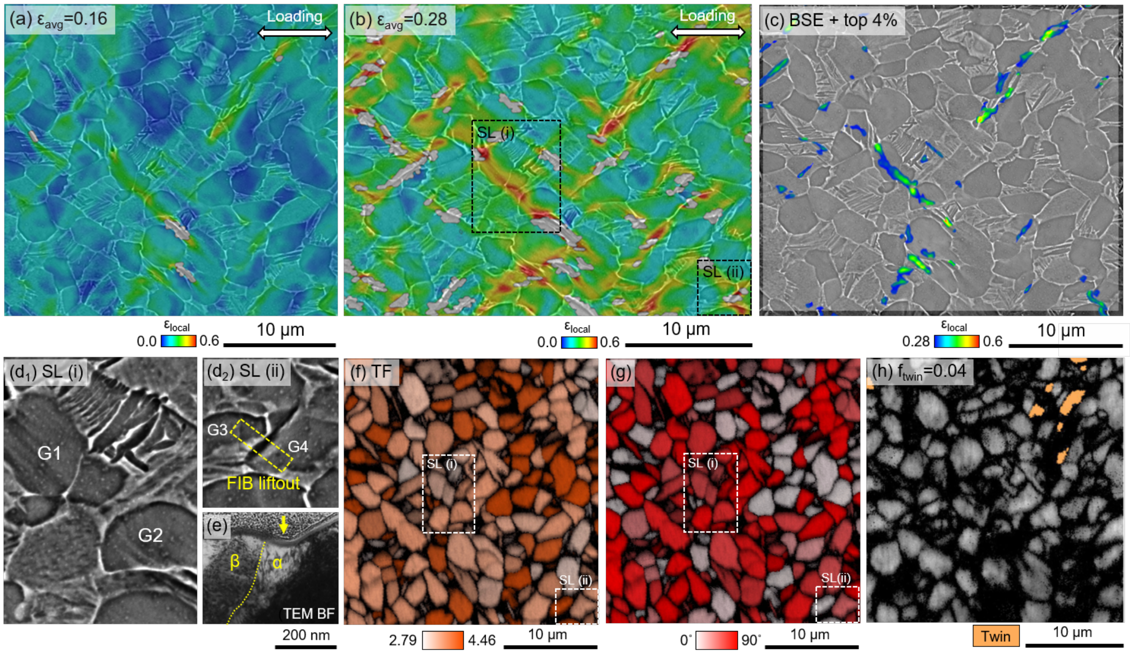

Figure 3-3: ***In situ* strain/EBSD maps and BSE micrographs.** *In situ* strain maps at (a) $\varepsilon_{avg} = 0.16$ and (b) $\varepsilon_{avg} = 0.28$ (FS/FD: 732/244 in nm). Two characteristic strain localization incidents are highlighted by the dashed boxes: strain localization across the multiple α grains (SL (i)) and along a boundary (SL (ii)). (c) SL incidents (FS/FD: 366/183 in nm) overlaid on the BSE micrograph acquired at $\varepsilon_{avg} = 0.28$. The SL incidents are defined as the strain subset having the local strain values greater than the 96th percentile (i.e., top 4% most strained subset). (d) BSE images of the deformed microstructures of SL (i) and SL (ii). Note that the small white dots in the BSE images are the contrast arising from the silica particles employed for μ-DIC. (e) TEM bright-field (BF) image of the cross-section of SL (ii). The yellow arrow indicates the boundary that creates the out-of-plane surface feature observed from the top surface. (f) Taylor factor map at an undeformed state. (g) Crystal orientation map showing the angles between the c-axes of HCP crystals (i.e., basal plane normal) and the loading direction. (h) Post-deformation IQ map with the mechanical twins highlighted.

These strain localization incidents possess distinct characteristics. In Fig. 3-3(b), two of them are labeled as SL (i) and SL (ii). SL (i) shows a strain band formed across multiple grains, while SL (ii) is an example of strain concentrated at the phase boundaries leading to loss of image correlation. The detailed features of these two incidents are also shown in the magnified BSE images (Figs. 3-3(d_1-d_2) with the associated grains labeled as G_i (i=1, 2, 3, 4). It should be noted that SL (ii) entails local surface features, shown in Fig. 3-3(d_2), which at first glance resemble a surface cracking incident. Further investigations by lifting a FIB lamella and cross-section TEM characterization suggest the presence of surface relief (rather than a crack) near the β ligament (Fig. 3-3(e)).

It should be also noted that as loaded along the TD, as expected, the alloy exhibits mechanically-induced surface features due to twinning, as highlighted in Fig. 3-3(h). The point-to-origin misorientation profiles in Fig. 3-4 demonstrate that these mechanical twins are $\{10\bar{1}\bar{2}\}$ extension twins, which have been commonly reported in HCP metals [114–116]. The fraction of the mechanical twins (f_{twin}) is low, as aimed, in the selected area of investigation, e.g., $f_{twin} = 0.04$ at $\varepsilon_{avg} = 0.28$. This is based on the EBSD measurement with a step size of 60 nm.

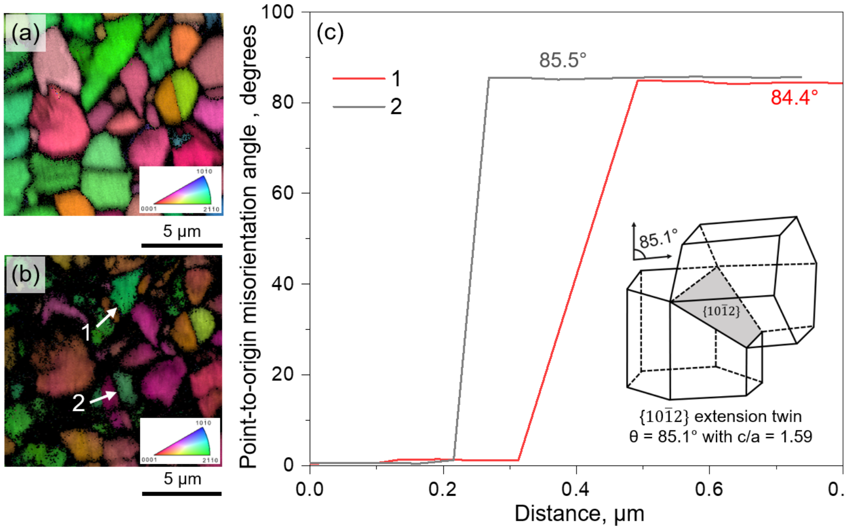

Figure 3-4: Occurrence of mechanical twinning in the microstructure. [001] IPF+IQ maps of a local area (a) before and (b) after deformation. (c) Point-to-origin misorientation angle profiles exported from the white lines (from left to right), 1 and 2, labeled in (b). This local area of the microstructure exhibits mechanical twinning upon straining, and the misorientation angle profiles demonstrate that the twins formed in (b) correspond to the $\{10\bar{1}\bar{2}\}$ extension twins. Note that the angular resolution of the EBSD measurements is 1.

Classification of strain localization incidents

The distinct characteristics of the strain localization incidents as shown in the exemplary cases of SL (i) and SL (ii) implies that the microstructure experiences multiple strain localization mechanisms concurring upon straining, and thus reliable identification and classification of the strain localization incidents as well as evaluation of their statistical importance should be preceded to reveal the underlying microstructural interactions responsible for strain heterogeneity. Acknowledging this necessity, here we focus on (i) introducing the microstructural criteria employed in the study to identify the strain localization incidents and (ii) correlating such incidents with the characteristics of the local microstructural environment.

First of all, local microstructure characteristics were evaluated based on relative strength of α grains by employing local Taylor factor and crystal orientation analyses. A Taylor factor map of the as-received microstructure (Fig. 3-3(f)), for example, can be considered as an initial probe of the relative kinematic hardness of the HCP crystals in the microstructure. The input CRSS ratio is basal <a> : prismatic <a> : pyramidal I <a> : pyramidal II <c+a> = 1.15 : 1 : 1.79 : 2. The CRSS values were calculated using EVPSC simulations and the fitting results are shown in Fig. 3-5. To ensure the accuracy of the fitting, the true stress-strain curves measured from the tensile tests performed along the three loading directions, i.e., rolling direction (RD), transverse direction (TD), and 45 degrees to RD and TD, were employed in the fitting. The modeled stresses along the three directions show a good agreement with the measured stress-strain curves. The back-extrapolated CRSS values are also in accord with the ones documenented in similar (α+β) titanium alloys [22,90]. The contributions of the β phase and mechanical twinning were excluded from the model to reduce numerical complexity [117,118]. The accuracy of the model thus can be improved considering the influence of the β phase as shown in the literature [113,119,120].

Fig. 3-3(g) is a crystal orientation map displaying the misorientation of the HCP crystals, i.e., the angle between the c-axes and the loading direction. The relationship between the local Taylor factor and misorientation of a HCP crystal is shown in Fig. 3-6. If misorientation of an HCP crystal is relatively small, for instance, the activation of the easy slip systems such as prismatic and basal slip modes having low CRSS values are greatly suppressed, and thus the crystal exhibits high resistance to plastic deformation and possesses a high Taylor factor. On the other hand, in the case of high misorientation, the prismatic and basal slip modes are readily allowed, and such reduced barrier to yielding is represented as a low Taylor factor of the crystal.

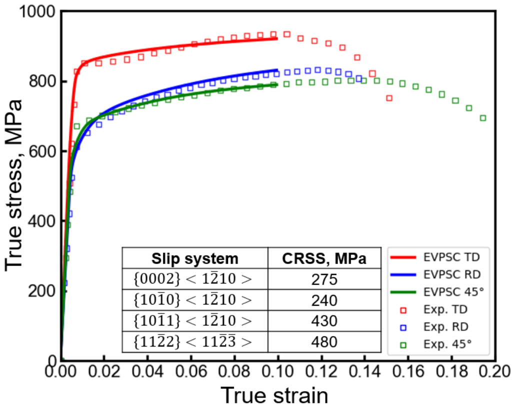

Figure 3-5: Calculation of critical resolved shear stress (CRSS) of α phase. True stress-strain curves of the alloy measured experimentally and the corresponding stress-strain curves fitted by the elastic-viscoplastic self-consistent (EVPSC) simulations. The table includes critical resolved shear stress (CRSS) magnitudes of basal, prismatic, pyramidal I <a>, and pyramidal II <c+a> slip systems calculated from the micromechanical model. Note that this EVPSC simulation was performed by Dr. Gaoming Zhu.

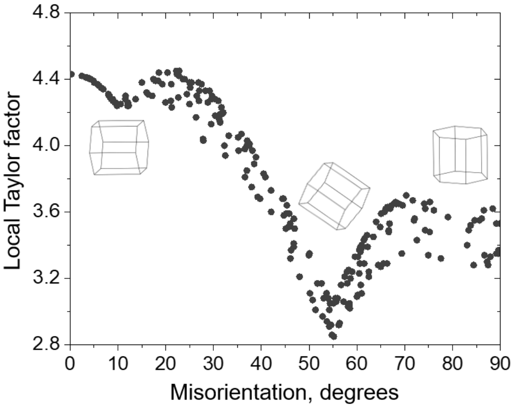

Figure 3-6: Correlation between local Taylor factors and misorientation. The local Taylor factors and misorientation of the α grains in Fig. 3-1(b) were exported using the OIM software. The misorientation represents the angle between the c-axis (i.e., basal plane normal) of an HCP crystal and the loading axis.

Next, the local microstructures (or α grains) surrounding the incidents were labeled as either 'soft (S)' or 'hard (H)' grains based on the relative kinematic hardness of the HCP crystals. By employing the bimodal distribution of Taylor factors in the microstructure shown in Fig. 3-7, a soft grain is defined as a grain of a Taylor factor smaller than 3.9 and a hard grain of a Taylor factor equal to or larger than 3.9. Based on this criterion, SL (i) occurs across the soft grains (G1 and G2), while SL (ii) is observed at the boundary between a hard grain (G3) and a soft grain (G4), as highlighted by the dashed boxes in Figs. 3-3(f-g). It should be worthwhile noting that considering the correlation between local Taylor factors and misorientation as presented in Fig. 3-6, this criterion is nearly equivalent to the following: a soft grain is defined as a grain having misorientation higher than 40, and a hard grain is defined as a grain having misorientation equal to or smaller than 40. Although one may choose 3.8 or 4.0 instead of 3.9, the statistical outcome is not altered due to the statistical scarcity of the grains having local Taylor factors between 3.7 and 4.2. To be specific, only one incident among 42 is affected if one chooses 3.8 other than 3.9, and none of the incidents are changed if one chooses 4.0.

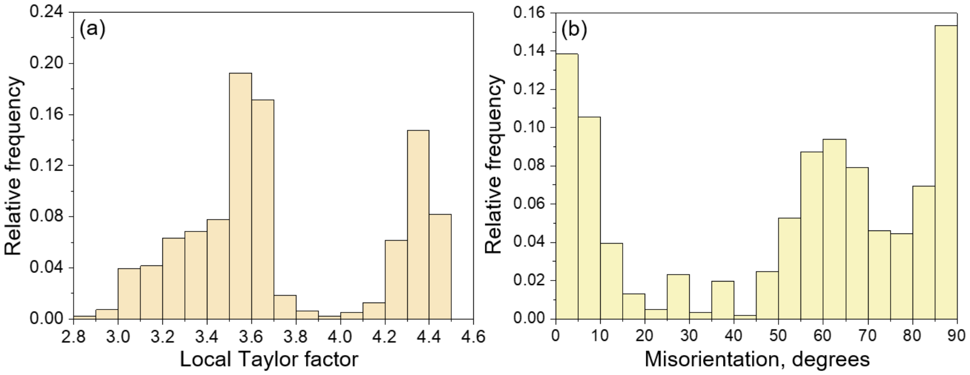

Figure 3-7: Local Taylor factor and misorientation distributions of the as-received microstructure. Distributions of (a) local Taylor factors and (b) misorientation.

Finally, the strain localization incidents were systematically classified based on the locations and Taylor factors of the neighboring α grains (Fig. 3-8). The contribution of the incidents in each type was weighted based on their number fraction (in %) among 42 incidents. The incidents were first classified into intragranular (strain localization within a grain or across multiple grains) and intergranular (strain localization at or along boundaries) types. Then, the boundary strain localization incidents were grouped into soft-soft (S-S), soft-hard (S-H), and hard-hard (H-H) types based on the Taylor factors of the surrounding grains, further classified into 'center' and 'side' depending on the position of the incidents relative to the midpoint of boundaries. That is, if the distance (d) between the midpoint of a strain localization incident and β phase is equal to or smaller than a quarter of the thickness (t) of the β phase, i.e., $d \leq 0.25t$, the incident is classified as 'center'. In the other case, i.e., $d > 0.25t$, the incident belongs to 'side' category.

The classification results in Fig. 3-8 shows about 17% (in number fraction) of the strain localization occur within grains, mostly inside a soft grain or across multiple soft grains as similarly observed in SL (i) in Fig. 3-3(b). No such intragranular-type strain localization incidents were observed within hard grains. The boundary strain localization incidents account for 83% of all localizations, with the majority of them located near the boundaries surrounded by soft and hard grains (50%). One example is SL (ii) in Fig. 3-3(b). An interesting observation made on the position of the boundary strain localization incidents is that boundary strain localization tends to occur in a position skewed towards one of the adjacent grains ('side') rather than located in the middle of the boundaries ('center'). This tendency is commonly observed in most boundary strain localization incidents, especially in the S-S and S-H types. For the S-H type, the localization incidents tend to be inclined towards a soft grain instead of a hard grain.

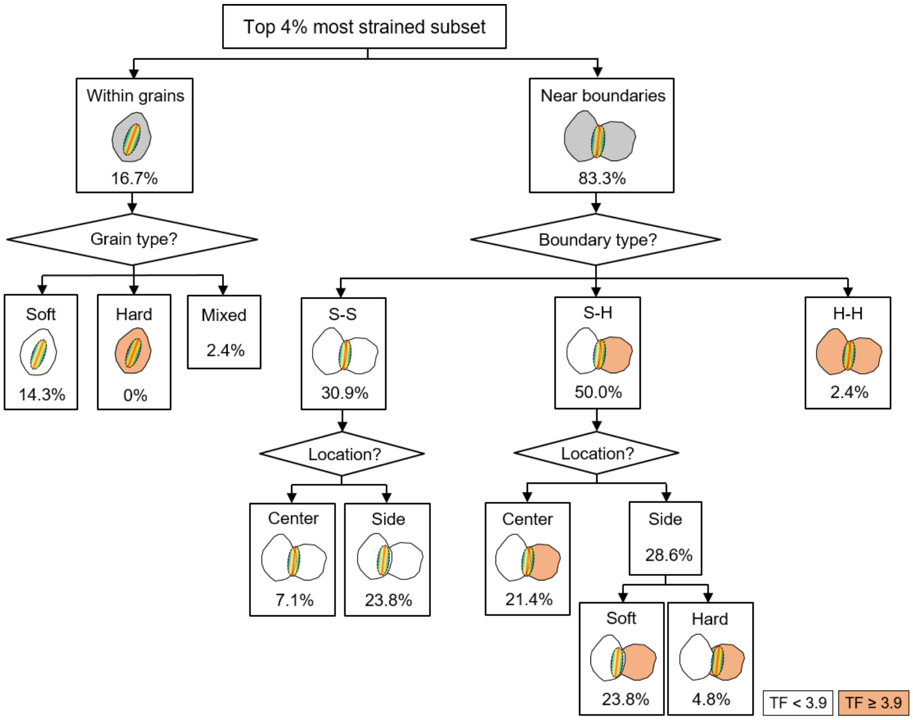

Figure 3-8: Classification of the strain localization (SL) incidents. The classification of the SL incidents has been made based on their locations and the relative kinematic hardness of surrounding grains. The values in % indicates the number fraction of the SL incidents corresponding to each category (among 42 incidents).

Local strain at boundary strain localization incidents

The local strain profiles exported from the boundary strain localization incidents also demonstrate intense strain accumulation in the soft grain side of the boundaries rather than near the hard grain. The strain profiles exported across the three boundary types, e.g., S-S (Fig. 3-9(a)), S-H (Fig. 3-9(b)), and H-H (Fig. 3-9(c)), show a considerable level of strain heterogeneity that develops at a grain scale, especially inside the soft grains. Specifically, the strain profiles across the S-S and S-H boundaries (Figs. 3-9(a_2) and 3-9(b_2)) demonstrate a noticeable escalation of local strain near the boundaries of the soft grains. For the S-H boundaries (Fig. 3-9(b)), the local strain reaches the peaks at the position slightly leaning towards the soft grains (as pointed by '▼'). The magnitudes of the local strain at the exact middle points of the S-S and S-H boundaries (labeled as '○') tend to be lower than the peak values observed in the soft grains. Relatively mild development of local strain is observed across a series of hard grains (Fig. 3-9(c_2)).

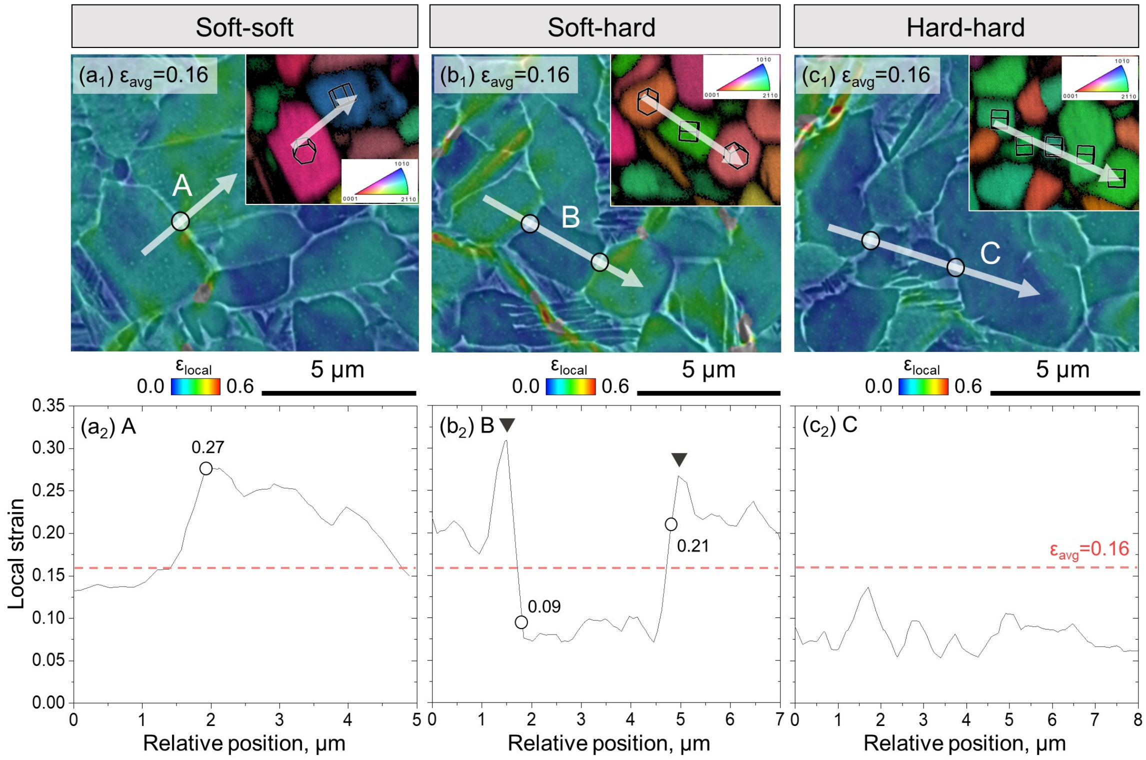

Figure 3-9: Local strain profiles across different types of boundaries. An *in situ* strain map (FS/FD: 366/183 in nm), a Taylor factor map (pre-deformation), and local strain profiles obtained at ε_{avg}=0.16 are shown for the three types of boundaries: the boundaries surrounded by (a) soft grains, (b) soft and hard grains, and (c) hard grains. The strain profiles were exported from the white arrows shown in the *in situ* strain and Taylor factor maps. The middle points of the boundaries are indicated by the white circles ('○') in the strain maps, and the local strain values at these points ('○') are shown in the strain profiles. Note that no twinning was observed in any of the hard grains in (c) where the strain profiles were exported.

To evaluate the severity of the boundary strain localization incidents and to demonstrate the microstructural origin, the local strain and geometry of 34 boundary incidents were systematically examined. Mean and maximum local strain values of 13 S-S and 21 S-H boundary incidents as well as the angles of the boundaries where the incidents formed were exported. The angle between a boundary and the tensile direction was measured from the BSE image captured before the deformation. The result shows that the strain localization incidents which form at S-H boundaries tend to exhibit higher mean and maximum local strain values, compared to the ones at S-S boundaries (Fig. 3-10). Despite small differences in mean local strain , the maximum local strain is roughly 13% higher in the S-H boundary incidents than in the S-S incidents. This higher local strain in the S-H incidents implies that the most critical incidents can form along S-H boundaries, which is consistent with the sharp local strain development observed at the S-H boundaries shown in Fig. 3-9(b_2). Note that compatible observations were made in hot deformation where cavity nucleation is facilitated at the boundaries comprised of soft- and hard- α colonies [104,105]. Furthermore, these boundary strain localization incidents are commonly found along the grain or phase boundaries about 40-60 degrees inclined to the loading axis. Among 31 incidents, for instance, about half of the incidents form along the boundaries 40-60 degrees tilted to the loading axis. The corresponding raw data of boundary type, location, mean and maximum local strain, and boundary angle is provided in Table 3.2 in Appendix.

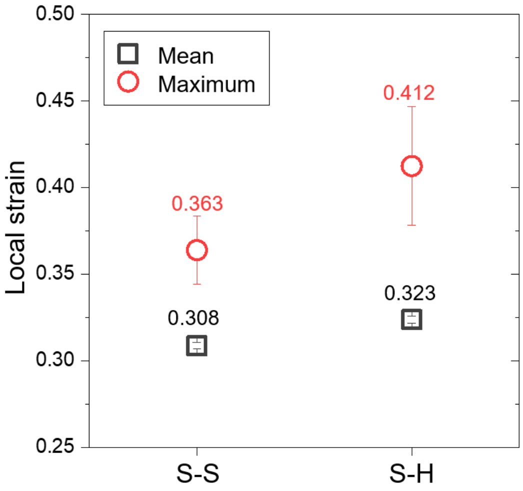

Figure 3-10: Local strain statistics of boundary strain localization incidents. Mean and maximum local strain at soft-soft (S-S) and soft-hard (S-H) boundary strain localization incidents (FS/FD: 366/183 in nm). The error bars are the standard error of the mean for the mean strains and standard deviation for the maximum strains, respectively.

Subsurface effects on strain mapping

It should be also recognized that surface strain mapping is intrinsically blinded to potential influences originating from the grains right below the surface. To assess these sub-surface grain effects, an extensive inspection was performed after FIB surface milling on whether there is a distinct microstructure, either a new grain or phase, immediately underneath the strain localization incidents. Owing to the destructive nature of FIB, this verification process was carried out on a newly generated *in situ* dataset. The milling depth, 0.5∼1 µm, was chosen to be smaller than the average grain size (∼2.7 µm) but higher than the width of the strain bands (∼0.55 µm). The result of this assessment shown in Fig. 3-11 demonstrates that 90% of 60 strain localization incidents (mostly boundary strain localization incidents) do not exhibit new grains or phases right below the surface, which indicates negligible correlation with sub-surface microstructure and surface strain localization.

Summary

The systematic classification of the strain localization events indicates the intragranular strain localization in soft grains (e.g., SL (i)-type, referred to from here onwards as multi-grain strain localization) and intergranular strain localization at soft-hard boundaries (e.g., SL (ii)-type, referred from here onwards as boundary strain localization) are the two most pronounced types that constitute the majority of the strain localization incidents. The band-shaped boundary strain localization incidents tend to be inclined towards soft grains while mild strain development was observed in hard grains. The most critical incidents that exhibit high local strain can form along S-H boundaries having an angle of 40 and 60 degrees to the loading axis. These observations in shape, local strain, and location of the boundary strain localization incidents suggest that dislocation plasticity in soft grains or the relative alignment of active slip systems in soft grains with grain or phase boundaries may play a role in promoting strain localization along the boundaries in this microstructure. The microstructural discussions regarding these two characteristic incidents are provided in Section 3.6.

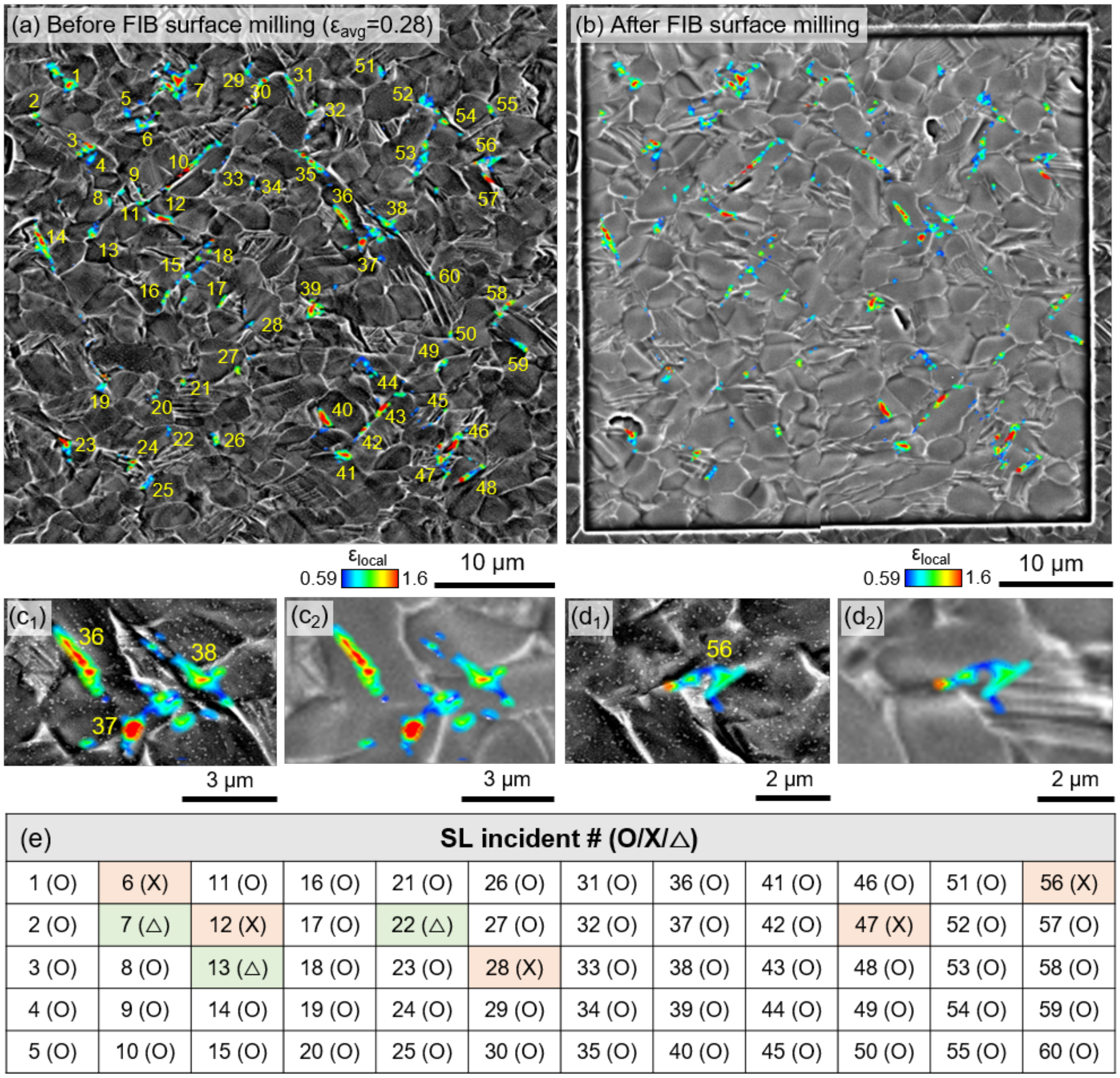

(e)	SL incident # (O/X/△)										
1 (O)	6 (X)	11 (O)	16 (O)	21 (O)	26 (O)	31 (O)	36 (O)	41 (O)	46 (O)	51 (O)	56 (X)
2 (O)	7 (△)	12 (X)	17 (O)	22 (△)	27 (O)	32 (O)	37 (O)	42 (O)	47 (X)	52 (O)	57 (O)
3 (O)	8 (O)	13 (△)	18 (O)	23 (O)	28 (X)	33 (O)	38 (O)	43 (O)	48 (O)	53 (O)	58 (O)
4 (O)	9 (O)	14 (O)	19 (O)	24 (O)	29 (O)	34 (O)	39 (O)	44 (O)	49 (O)	54 (O)	59 (O)
5 (O)	10 (O)	15 (O)	20 (O)	25 (O)	30 (O)	35 (O)	40 (O)	45 (O)	50 (O)	55 (O)	60 (O)

Figure 3-11: Subsurface microstructure verification after FIB-assisted surface milling. (a) BSE micrograph overlaid with 60 strain localization incidents. (b) BSE micrograph of the same area as (a) after FIB-surface milling. The incidents were classified into the following three categories: (i) 'O': no significant change found in subsurface microstructure (e.g., no new phase or grain right underneath the incidents), (ii) 'X': significant change found in subsurface microstructure (e.g., new α/β grain or lamellar structure found immediately below the incidents), and (iii) 'Δ': uncertain from the BSE image. (c) Strain localization incidents (36, 37, 38) labeled as 'O'. (d) Strain localization incident (56) labeled as 'X'. (e) Classification results. The result demonstrates that the majority of the incidents (90%) belong to the 'O' category, implying that the strain–microstructure correlation studied on the surface can be valid in this microstructure.

3.5 Damage and fracture analyses

It has been demonstrated that microscopic strain localization sites are likely microstructural features where damage nucleation takes place, leading to void growth, and eventually coalescence [32,121]. To investigate the damage and fracture behavior of the alloy, comprehensive damage analyses were performed by carrying out image analysis of the cross-sectional micrographs of the center of the fractured tensile specimen (Figs. 3-12(a-b)). Three 70 × 210 μm^2 SE images obtained at the same strain level were subjected to the image analysis (Figs. 3-12(c-d)). The analysis shows that this alloy in general exhibits co-deformation of the α and β phases with no damage nucleation until high strain levels. Extensive damage growth (i.e., increase in the average damage size) starts only near the end of the diffuse neck (2.99 mm away from the fracture surface), 0.39 mm distant from the fracture surface, and continues up to the end of the localized neck (0.17 mm away from fracture) as shown in the inset of Fig. 3-12(a).

Figs. 3-12(b_1-b_4) illustrate the morphological characteristics of voids at different stages of the nucleation-growth-coalescence process in detail. As expected from the strain localization trends, sub-micron voids first nucleate at the phase interfaces (small voids highlighted by the triangular marks (‘▼’) in Fig. 3-12(b_1)), expand along the boundaries (Fig. 3-12(b_1)), and coalesce into a micron-scale crack (Fig. 3-12(b_2)). Multiple micron-scale cracks develop in this manner, which ends up growing further and/or coalescing with other similar cracks (Figs. 3-12(b_3-b_4)). An interesting observation is that the critical crack development occurs through a series of coalescence steps; sub-micron voids growing along boundaries first coalesce into a micron-scale crack (Fig. 3-12(b_2)), and the micron-scale crack evolves into a critical size crack once it meets and coalesces with another damage (Fig. 3-12(b_3-b_4)).

A more quantitative analysis of these microstructural damage mechanisms was carried out by focusing on the damage evolution curves. The curves in Fig. 3-12(c) show how the number density, the area fraction, and the average size of the cross-sectional damage incidents increase with the average strain (ε_{avg}) measured across the gauge by optical DIC. The average strain at the last deformation step in the *in situ* test (Fig. 3-3(b)) is highlighted as the dashed arrow ($\varepsilon_{avg} = 0.28$). The damage evolution curves also indicate that the alloy exhibits a notably long nucleation period up to $\varepsilon_{avg}\sim0.6$ with a limited number of damage incidents observed up to $\varepsilon_{avg}\sim0.6$ (i.e., well beyond the uniform elongation of $\varepsilon_{eng}\sim0.08$). The number density and the area fraction of damage incidents exhibit a mild increase from $\varepsilon_{avg}\sim0.6$ to $\varepsilon_{avg}\sim0.75$ and start to rise drastically only from $\varepsilon_{avg}\sim0.75$ onwards. The average size of the damage incidents shows a similar trend.

It should be noted that the damage incidents in the localized neck ($\varepsilon_{avg} > 0.85$) exhibit a large size variation as seen by the error bars in Fig. 3-12(c) at $\varepsilon_{avg} > 0.85$, as well as in the histogram in Fig. 3-12(d). The histogram shows that ~90% of the damage incidents generated in the localized neck are smaller than 1 μm^2, while a limited number of the damage incidents end up growing significantly. The table in Fig. 3-12(d) shows the sizes of the five largest damage incidents, where it can be seen that the largest one reaches over 29 μm^2. This stochastic observation indicates that the actual fracture in the alloy develops from the most critical coalescence event leading to the largest crack in the localized neck region. Figs. 3-12(b_1-b_2) show that the initial micro-void coalescence can result in the horizontal damage incidents. Subsequent coalescence processes, however, can lead to the larger cracks vertical to the loading axis, and these cracks are the most critical ones causing final failure. It should be also noted that these observations were made from the fractured specimen where the large damage sites stopped growing when the most fatal crack coalescence decreases the local stress. Cracking at inclusions was also observed but the number density of inclusions is $(2.31 \pm 0.45)\times10^{-3}$ μm^{-2}, which corresponds to about two inclusions per 1000 μm^2. The average size of the inclusions is 0.064 ± 0.007 μm^2.

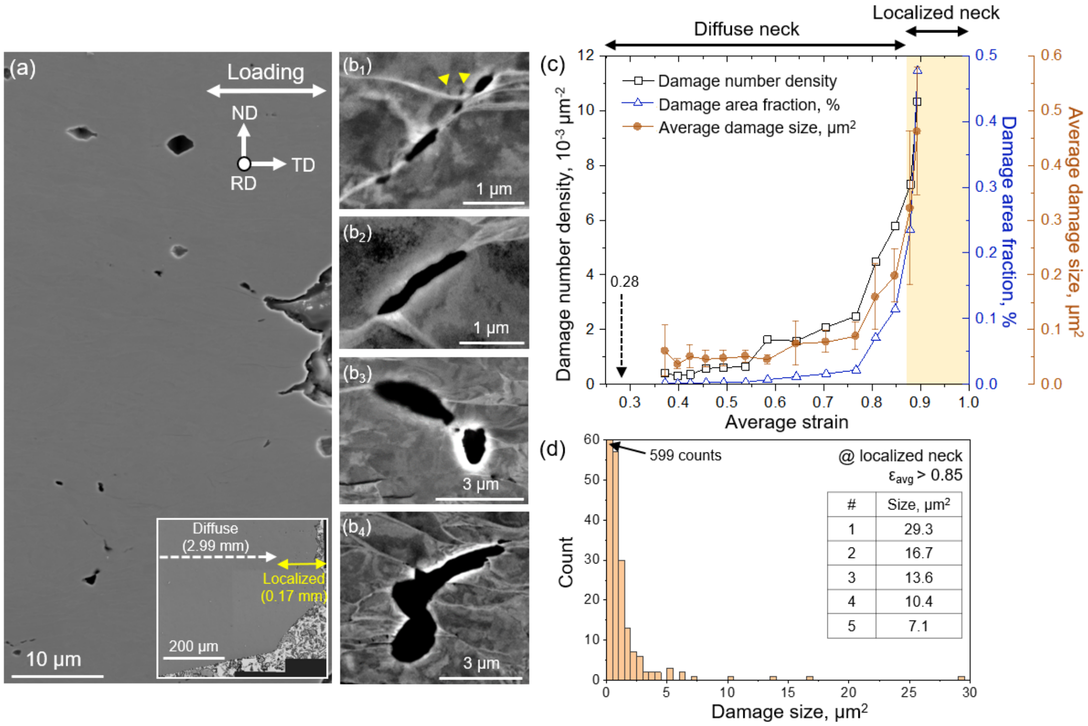

Figure 3-12: Damage micrographs and damage evolution at different strain levels. (a) large field-of-view SE image of the cross-section of the fractured tensile specimen. BSE images of (b_1) damage nucleation and sub-micron damage growth, (b_2) damage growth along the boundaries, and (b_3-b_4) micron-scale damage coalescence processes. (c) Evolution of the number density, area fraction, and average size of damages with increasing average strain (ε_{avg}) across the gauge. (d) histogram of the size of the damages at the localized neck (where $\varepsilon_{avg} > 0.85$). The count of the first bin is 599, and the table shows the sizes of the five largest damages.

Fig. 3-13 shows a fracture surface of the cone part of the fractured tensile sample. The fracture surface exhibits a large number of dimples, characteristic of the classical ductile mode of fracture. The average dimple size corresponds to 3.48 ± 1.637 μm, which is slightly larger than the average grain size of the α phase, i.e., 2.71 μm. In addition to the dimples, some areas of the fracture surface (e.g., the region in the yellow box in Fig. 3-13(a)) exhibit ledge-like topological features as highlighted by the arrows in Fig. 3-13(c). The approximate distance between the ledges is 29.6 ± 3.53 μm, which is far higher than the average sizes of the dimples as well as α grains.

In summary, the detailed damage characterization and the fractography analysis reveal that in the Ti-0.85Al-3.90V-0.25Fe-0.25Si-0.15O alloy, ductile damage growth and coalescence processes are delayed despite the multi-phase nature of the alloy with characteristically different α and β phases. For the major part of the deformation processes, the average damage size remains below 0.1 µm^2. Only in the final stages of the localization process, significant damage growth and coalescence are observed, leading the macroscopic cracking. The delay in the activation of damage mechanisms until the late stages of deformation can be discussed in the context of co-deforming characteristics of the present two phases.

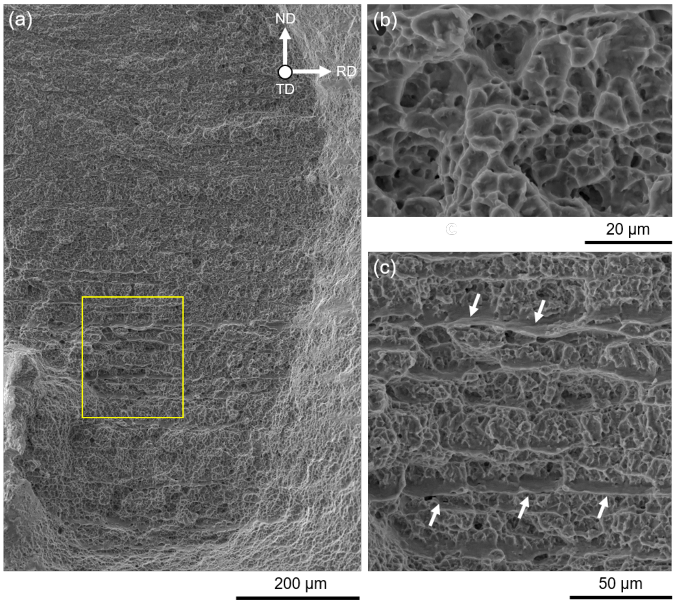

Figure 3-13: Fracture surface. (a) Low magnification SE image of the fracture surface. (b) Dimples. (c) SE image of the region in the yellow box in (a). The white arrows identify the ledges formed on the fracture surface.

3.6 Strain localization mechanisms

3.6.1 Multi-grain strain localization

The quantitative analysis of strain localization incidents presented in Fig. 3-8 presents that about 17 percent of strain localization (among 42 incidents) occurs either in soft grains or across multiple soft grains. One evident example of such incident, SL (i) in Fig. 3-3, is subjected to further investigation in this section. One potential microstructural mechanism ascribed to the formation of such relatively long-range, intragranular strain localization incidents is the activation of slip systems co-aligned among neighboring α grains. It has been studied that the long-range localizations can become prominent in micro-textured titanium alloys where clusters of α grains share preferred orientation, as studied in an equiaxed (α+β) Ti-6Al-4V alloy [101, 102].

The methodology exploited to evaluate the role of local texture in governing local slip activation is a surface trace analysis based on in-house developed MatLab and python codes [112]. Although salient success has been achieved by the trace analysis methodology in studying plastic deformation of both single [122–124] and multi-phase alloys [74, 125], its limitations can be also documented as follows: (i) the interference from surface imperfections, such as mechanical scratches or contamination; and (ii) the geometric misalignment between SE images and EBSD measurements; and (iii) the deformation-induced misalignment. For (i), it was validated through surface observation that the surface was free of such artifacts before deformation. For (ii), the image quality (IQ) map of the corresponding EBSD measurement was utilized to mitigate the systematic misalignment. Potential errors arising from (iii) may be significant at large levels of deformation, for example, ε_{avg}=0.28 in the study (Fig. 3-3(b)) where a considerable amount of lattice rotation and surface roughness were introduced in the microstructure. To alleviate the influence of this type of misalignment, the EBSD image recorded before deformation and the BSE micrograph taken at ε_{avg}=0.16 (clearly showing SL (i)) were employed for the crystallographic analysis.

First, relative slip activity of the microstructure environment surrounding the incident SL (i) was evaluated. Three local microstructure areas, A, B1, and B2 in Fig. 3-14(a), were selected for comparison. Area A includes the intragranular strain band, SL (i), while the other two areas, B1 and B2, exhibit relatively homogenous strain distribution. The local EBSD maps of the selected microstructures employed for the calculation are shown in Figs. 3-14(b_1-b_3), and the corresponding EBSD datasets have almost the same number of measurement points. Grain area cumulative distribution functions (CDFs) of Schmid factor (SF) were calculated taking into account four slip systems: basal, prismatic, pyramidal I <a>, and pyramidal II <c+a>. The graphs in Figs. 3-14(c_1-c_4) demonstrate that the local area A exhibits relatively high activity of pyramidal I <a> slip compared to other areas. For area A, for instance, the area fraction of the grains having SF $\geqq$ 0.45 for the pyramidal I <a> slip is ~0.78, which means that the grains in area A are geometrically oriented in a way that favors the activation of the pyramidal I <a> slip. On the other hand, for areas B1 and B2, the corresponding values are ~0.39 and ~0.02, respectively, indicating a much less probability of the activation of the pyramidal I <a> slip. It should be also noted that the activity of prismatic slip can be also high, considering its low resistance to slip, which is represented as its lowest CRSS among all other slip systems. The analysis implies that from a purely geometrical perspective, i.e., slip plane alignment to the loading axis, the formation of the intragranular strain band in area A can involve the activity of the pyramidal I <a> or prismatic slip.

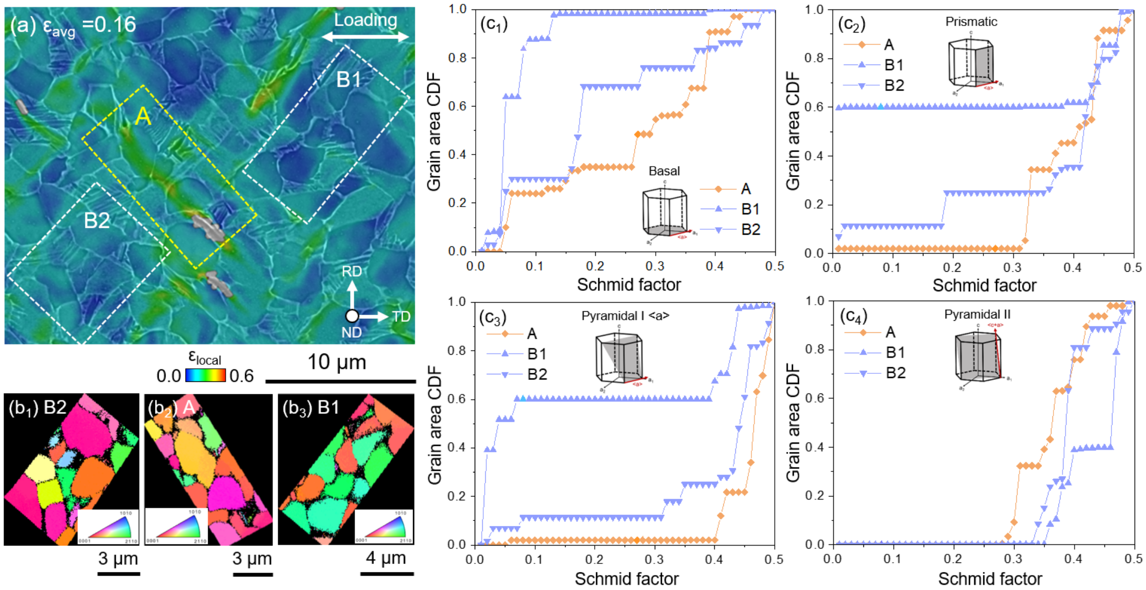

Figure 3-14: Crystallographic assessment of slip activity of three local regions. (a) *in situ* strain map showing three local areas of investigation (FS/FD: 732/244 in nm), e.g., A: the area including the transgranular strain localization incident, and B1 and B2: the two selected areas showing relatively homogeneous deformation. (b) [001] IPF maps of the three areas (A, B1, and B2). Grain size cumulative distribution functions of Schmid factors of (c_1) basal, (c_2) prism, (c_3) pyramidal I <a>, and (c4) pyramidal II <c+a> slip systems.

Second, to further validate the participation of pyramidal I <a> or prismatic slip to the formation of the strain band, SL (i), the slip traces of the associated grains, G1 and G2, and corresponding SFs were calculated. The stress state was assumed to follow the global boundary condition, i.e., uniaxial tension, and the EBSD image recorded from the initial microstructure was employed for the calculation. A set of Euler angles was exported from the in-grain position of each grain as highlighted in

Fig. 3-15(b). The calculation results in Figs. 3-15(c_1-c_2) illustrate the slip traces of each member of the four slip system families, basal (red), prismatic (blue), and pyramidal I (green) slip systems, and corresponding SFs. Note that the highest SF among the three independent slip systems is shown for the basal slip trace, and the SFs of the pyramidal I slip traces correspond to pyramidal I <a>. Correlating the dotted line in black indicating the direction of the strain band to the calculated slip traces demonstrates that the formation of SL (i) is likely attributable to the activation of pyramidal I <a> slip in G1 and prismatic slip in G2, both of which exhibit high SFs (0.47 for $(1\bar{1}01)[\bar{1}\bar{1}20]$ at G1 and 0.44 for $(\bar{1}101)[\bar{1}\bar{1}20]$ at G2) compared to all other slip systems. This analysis suggests that the two closely aligned high SF slip systems in the vicinal grains lead to the long-range strain band formation across G1 and G2. The detailed calculation results are provided in Table 3.3 in Appendix.

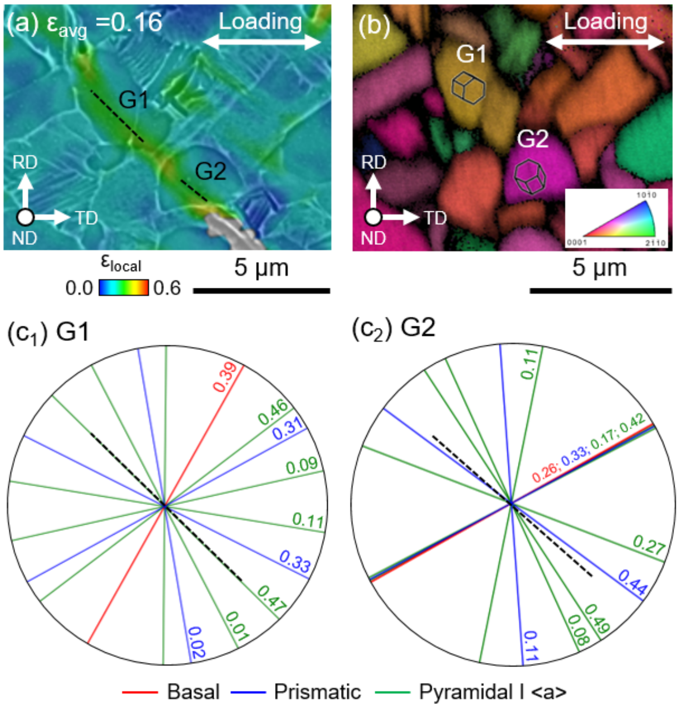

Figure 3-15: Crystallographic assessment of the strain localization event across multiple grains. (a-b) *In situ* strain (FS/FD: 732/244 in nm) and [001] IPF+IQ map of the local area where a transgranular strain band was observed. Euler angles exported from the points, G1 and G2, were used for slip trace calculation. (c) Slip traces and corresponding Schmid factors of basal, prismatic, and pyramidal I <a> slip planes. Only the maximum Schmid factor is shown for the basal slip traces.

3.6.2 Boundary strain localization

The most common type of strain localization in the alloy is boundary strain localization which accounts for 83% among 42 incidents (Fig. 3-8). The majority of the boundary incidents extend along the soft-hard boundaries (50%) and typically at the soft side (47.6%). One exemplary incident of this type is SL (ii) in Fig. 3-3. A microstructural process that can lead to such boundary incidents is the operation of high SF slip systems aligned nearly parallel to the boundaries. As predicted from high SFs of prismatic slip in 21 soft grains associated with the boundary strain localization (Fig. 3-16), the activation of prismatic slip in soft grains was observed in the investigated microstructural patch. An example is the slip trace highlighted by the yellow arrow in Fig. 3-17(b). Crystallographic assessments (see Table 3.4 in Appendix) demonstrate that this slip trace corresponds to the prismatic slip system having the highest SF (0.46), and that both prismatic slip plane and direction are near-parallel to the boundary (see the unit cell in Fig. 3-17(b)). Note also that DIC is lost at the soft side suggesting higher local strain value that develops in this soft grain. These observations suggest that the alignment of the slip system in a path that is absent of barriers for mobile dislocations, for example, along a boundary (as opposed to towards a phase boundary), leads to strain localization, and to more extensive out-of-plane surface relief (see cross-sectional TEM image shown in Fig. 3-3(e), and [126]). It should be emphasized, however, that this type of strain localization occurs most often when the soft-hard orientation coupling is present, which is not a feature repeating throughout this microstructure.

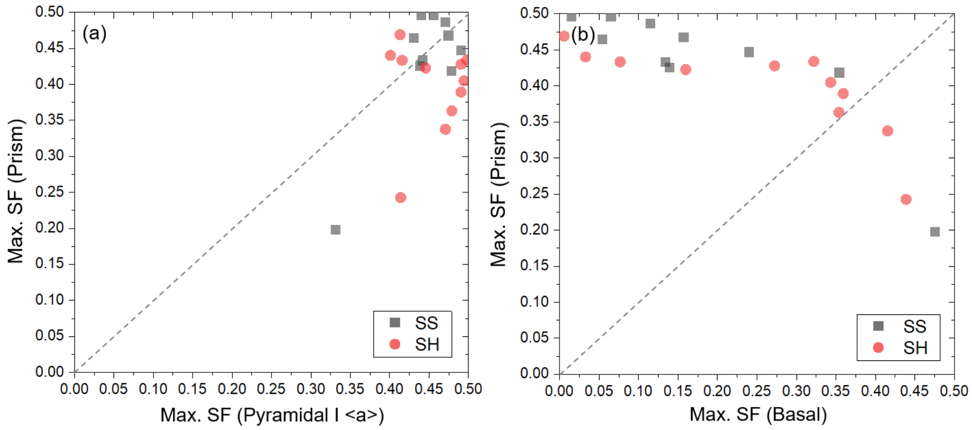

Figure 3-16: Slip activity evaluation of basal, prismatic, and pyramidal I <a> slip systems in soft grains. Maximum Schmid factors of (a) prismatic and pyramidal I <a> slip systems and (b) prismatic and basal slip systems. Note that the calculations were carried out on the soft grains involved in boundary strain localization incidents skewed towards soft grains. The dotted lines are the equipartition lines.

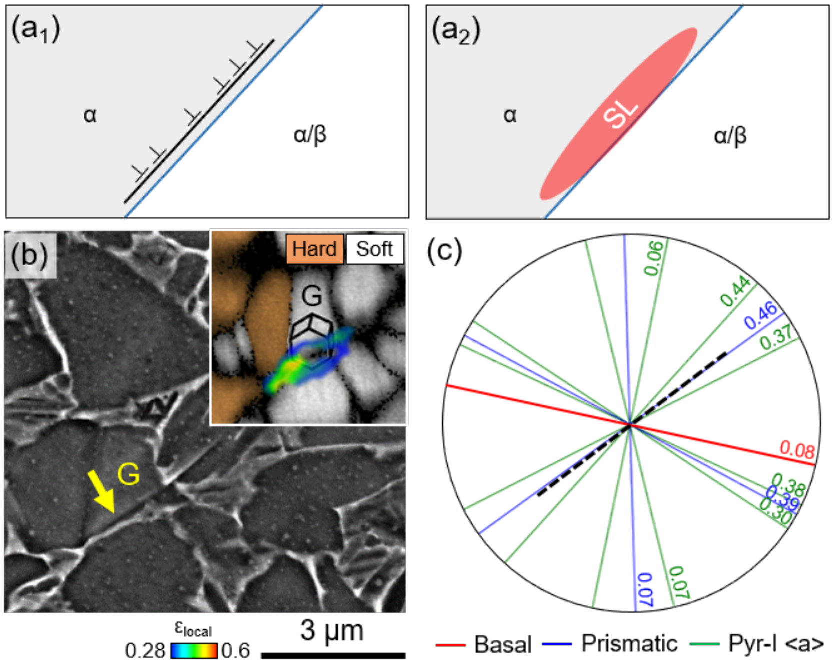

Figure 3-17: Slip trace assessment of a boundary strain localization event. Schematics of (a$_1$) mobile dislocations whose slip direction is nearly parallel to a boundary and (a$_2$) strain localization associated with (a$_1$). (b) BSE image showing a slip trace (pointed by a yellow arrow) in the soft grain labeled as 'G' and the discrete Taylor factor map of the same area showing soft (TF < 3.9) and hard grains (TF $\geqq 3.9$). The strain localization incident associated with this slip trace is overlaid on the Taylor factor map. (c) Potential slip traces and corresponding Schmid factors of grain G. The dotted line indicates the slip trace shown in (b).

3.7 Beta phase effects

In typical multi-phase alloys, intrinsic mechanical contrast between existing phases is considered a prominent factor that creates heterogeneous plastic strain distribution and promotes strain incompatibility at phase interfaces. This effect has been extensively studied in ferrous systems, especially in dual-phase steels, where the prominent strength contrast between the martensite and ferrite phases restricts the co-deforming capability of the microstructure and eventually leads to interface decohesion [33, 34, 36]. This microstructural influence is often captured by evaluating a tendency of plastic strain partitioning between the phases, and recent *in situ* microstructure studies have shown that ferrite (soft phase) can accommodate about 10 times higher plastic strain than martensite (hard phase) [32, 33]. However, it is intriguing to see here in this (α+β) Ti alloy that the strain localization processes can be explained through α characteristics only. This is especially surprising when, α grains may not effectively deform without comparable stretching of the β phase in between, due to the highly interconnected microstructure. Yet, our data suggests limited influence of the β phase on the strain localization tendency at the microscale. To discuss the origins of this, we focus next on two points: (i) slip transfer, and (ii) phase strength contrast. We also later note the effect of β-phase work-hardening.

Regarding (i), it is generally documented that limited deformation transfer across phase interfaces can be a major precursor of strain incompatibility and micro-void nucleation [72–78, 99, 100]. On the other hand, the β phase may not act as a significant barrier to dislocation motion if it exhibits high Schmid factors (easy slip) [78] and small thickness [74]. In this alloy, grain area cumulative distribution functions (CDFs) of Schmid factors (SF) for three popular BCC slip systems, i.e., $\{110\}\langle\bar{1}11\rangle$, $\{211\}\langle\bar{1}11\rangle$, and $\{321\}\langle\bar{1}11\rangle$, shown in Fig. 3-18, indicate that the β phase possesses relatively high SFs (oriented favorably to slip), implying favor in slip. In addition, the average width of the β ligament is small, i.e., ∼130 nm between the equiaxed αgrains, and ∼40 nm within the lamellar structures, which further decreases the possibility of slip impediment, especially at the early stages of plastic deformation [74].

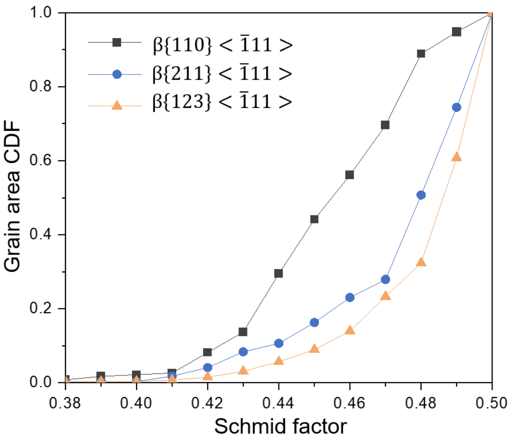

Figure 3-18: Slip activity assessment of β phase. Grain area cumulative distribution functions (CDFs) of Schmid factors of $\{110\}\langle\bar{1}11\rangle$, $\{211\}\langle\bar{1}11\rangle$, and $\{321\}\langle\bar{1}11\rangle$slip systems of β phase. This plot demonstrates that the β phase in the alloy exhibits relatively high SFs and thus prefers slip operation. For instance, the area fraction of the β grains whose SFs are higher than 0.45 is ∼0.56 for $\{110\}\langle\bar{1}11\rangle$, ∼0.84 for $\{211\}\langle\bar{1}11\rangle$, and ∼0.91 for $\{321\}\langle\bar{1}11\rangle$, respectively.

Next, we focus on (ii). In contrast to what has been observed in classical dual-phase steels, the dual-phase titanium alloy in the study exhibits an insignificant difference in the partitioned phase plastic strain (Fig. 3-19). The strain-partitioning plot in Fig. 3-19(a) demonstrates that, on average, the magnitudes of the plastic strain partitioned into each phase are comparable during the deformation. The mean values of the partitioned phase strain approximately correspond to the average strain imposed on the area of interest (ε_{avg}), as indicated by the equipartition line (dotted). The calculations performed with reduced facet size (Fig. 3-19(b)) also fail to capture the meaningful difference in the plastic strains partitioned into each phase. The partitioned strain in the β phase tends to be smaller as the facet size reduces (probably due to the improved spatial resolution since strain localization incidents are inclined towards the α phase) but the difference is statistically negligible and not enough to create substantial strain incompatibility.

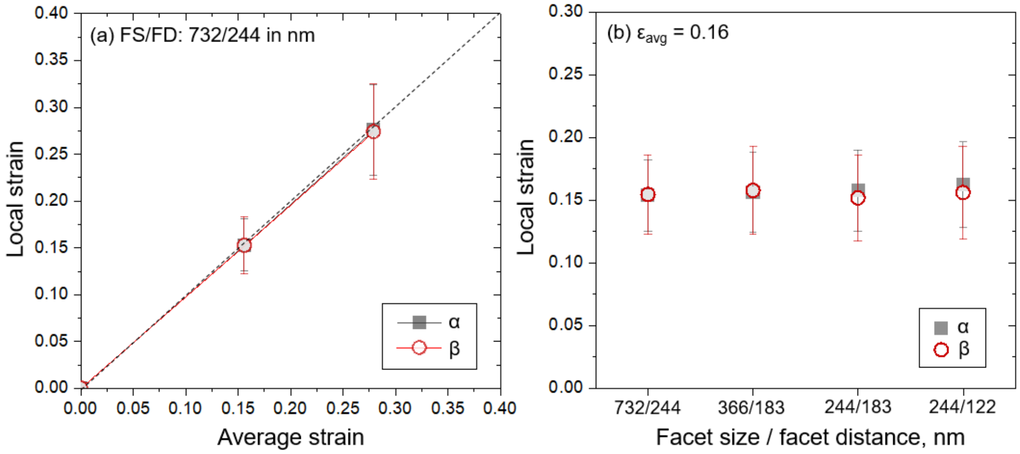

Figure 3-19: Plastic strain partitioning. (a) Phase strain partitioned in the α and β phases (FS/FD: 732/244 in nm). (b) Facet size dependency on partitioned phase strain at $\varepsilon_{avg} = 0.16$. Regarding (a), the facet size effects need also to be mentioned. No obvious plastic strain partitioning was captured here for various facet sizes (244-732 nm) and facet distances (122-244 nm). Reducing the facet size to lower values (Fig. 3-19(b)) can provide a slightly decreased plastic strain in the β phase, while this difference is not statistically significant.

Furthermore, nanoindentation measurements of the two phases performed in the as-received sample also do not show a statistically relevant difference in the nanohardness values (Fig. 3-20). One of the microstructural areas where the indentation was performed and its corresponding nanohardness contour map are shown in Figs. 3-20(a-b). The indents at the β phase are highlighted by the square boxes whose nanohardness values are similar to the ones measured from the surrounding α grains. The nanohardness value of the β phase averaged from 28 data points is 3.19 GPa (± 0.11), which is in the range of nanohardness variation of the α phase resulting from its orientation (Fig. 3-20(c)). It should be also noted that the size of the plastic zone that influences the nanohardness is 5-10 times the indentation depth [127]. The indentation depth of the two phases is about 35 nm, which leads to the plasticity zone in the range of 175∼350 nm. Such a relatively large plasticity zone compared to the width of the β ligament can create statistical difficulty in accurate measurement in the β phase nanohardness, but one can safely say that the nanohardness of the β phase is the range that the α phase can exhibit (2.92∼4.11 GPa). The same yield point of the two phases (measured through *in situ* SXRD testing in Fig. 3-2), the negligible difference in partitioned plastic strains (from *in situ* μ-DIC in Fig. 3-19) and nanohardness (Fig. 3-20) between the phases all suggest that the α and β phases, in general, tend to co-deform upon straining.

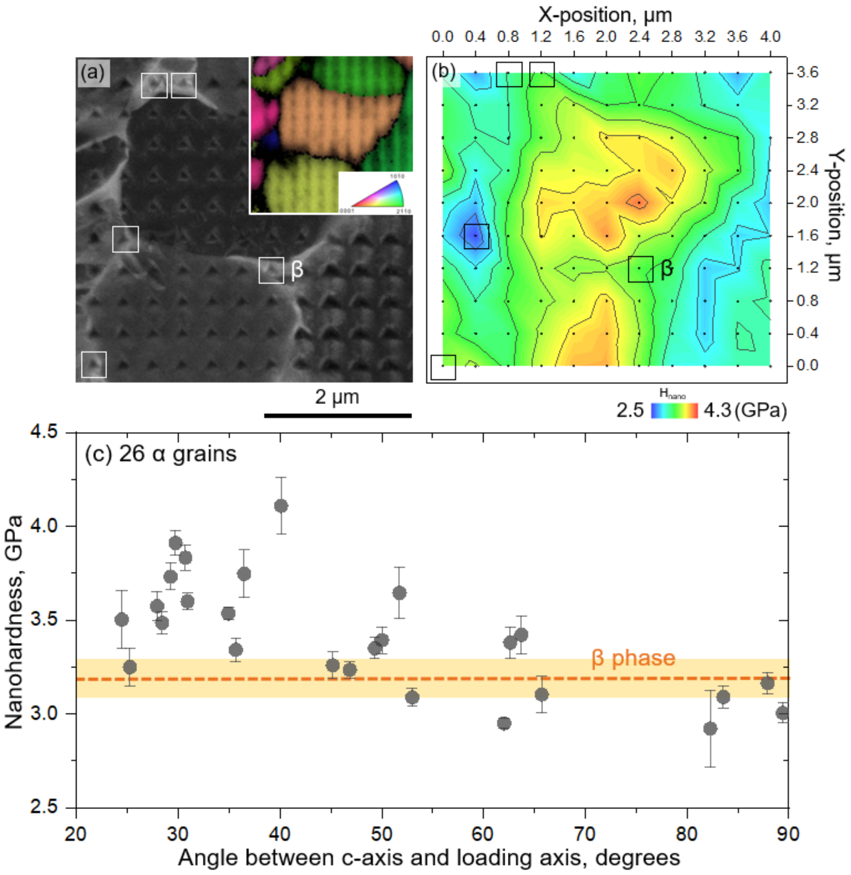

Figure 3-20: Nanohardness measurement on α and β phases. (a) BSE and IPF maps of one of the local microstructural areas where the indentation was performed. (b) Nanohardness contour map of the area in (a). The indents at the β phase are highlighted by the square boxes in (a) and (b). (c) Nanohardness values of α and β phases. The orientation dependency of the nanohardness values of the α phases is presented by the angle between the c-axis of an HCP crystal and the loading axis.

Despite the two-phase co-deformability, it should be also noted that the β phase exhibits work-hardening during the deformation, which leads to substantial load-partitioning between the phases and thus to the micro-void formation at the α/β interfaces. The considerable broadening of the diffraction peaks of the β{110} planes (i.e., higher FWHM change) indicates the crystal lattice of the β phase is substantially distorted by lattice defects, primarily by dislocations [128, 129]. Sharp plastic strain gradients due to high density of geometrically necessary dislocations near the α/β phase interfaces can also contribute to this observation, as predicted by a strain-gradient CP model [108]. Such β phase hardening can accelerate strain localization in the α grains, in addition to the primary slip near-parallel to the boundary in Fig. 3-17, since the α grains next to the β phase need to compensate for the strain incompatibility that develops during the deformation. The statistical outcome demonstrating the prevalent occurrence of the boundary strain localization in the soft α grains (Fig. 3-8) also supports these mechanisms. Slight change in the strain partitioning at small facet sizes may also be an indication of this strain hardening effect (Fig. 3-19(b)).

3.8 Conclusion

In this work, by incorporating the microstructural insights accomplished through *in situ* SEM/SXRD experimentations, the microstructural origin of heterogeneous deformation as well as its micromechanical consequences in relation to damage creation are examined in the two-phase Ti alloy. It is observed that both phases can deform comparably to high strain levels without significant ductile damage evolution. A schematic sketch in Fig. 3-21 summarizes a series of strain localization, damage, and failure processes of the two-phase Ti alloy in the study. The starting microstructure consisting of soft and hard α phase and β phase is shown in Fig. 3-21(a_1), and upon straining, the two characteristic strain localization types can be observed: multi-grain strain localization in soft grains (Fig. 3-21(a_2)) resulting from the activation of co-aligning slip systems and boundary strain localization (Fig. 3-21(a_3)) arising from the active slip systems aligned parallel to boundaries. Further straining up to the later deformation stage leads to nucleation of submicron-scale voids at the boundaries and their growth (Fig. 3-21(b_1)) and coalescence into the micron-scale cracks. (Fig. 3-21(b_2)). At a localized neck, such micron-scale cracks coalesce into a crack of critical size.

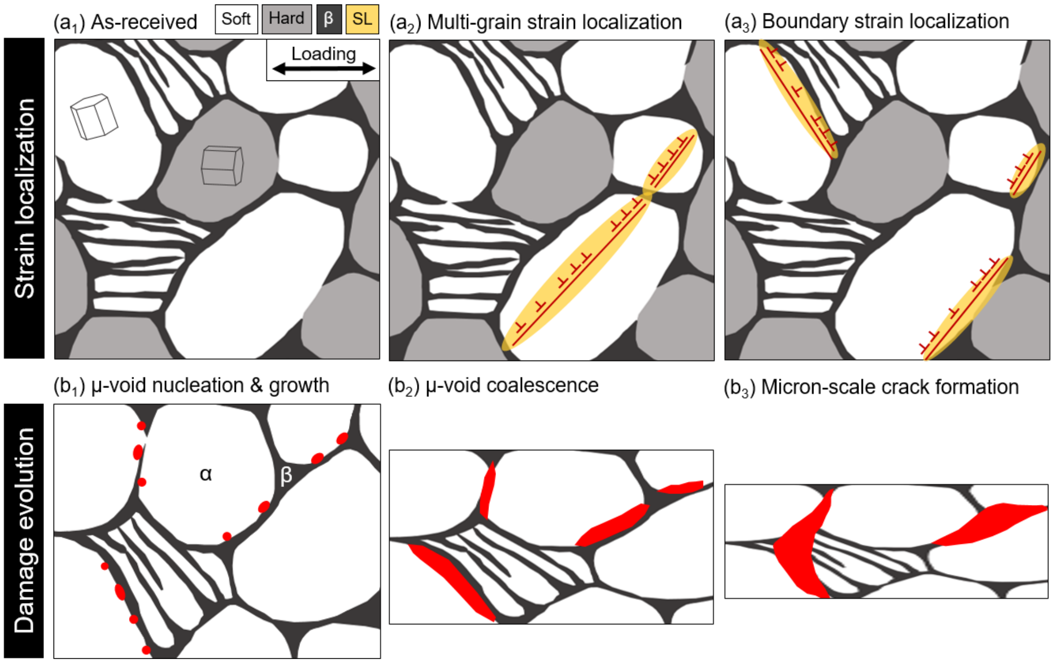

Figure 3-21: Strain localization (top view) and damage/failure mechanisms (cross-section view). (a$_1$) Exemplery as-received microstructure of a two-phase titanium alloy consisting of α phase (soft and hard) and β phase. (a$_2$) Multi-grain (intragranular) strain localization. (a$_2$) Boundary (intergranular) strain localization. (b$_1$) Micro-void (μ-void) nucleation and growth along phase boundaries. (b$_1$) Micro-void void coalescence into micron-scale cracks. (b$_3$) Coalescence of the micron-scale cracks into the cracks of critical size.

The main findings of the study are summarized as follows.

(1) Two critical strain localization mechanisms are identified through the *in situ* μ-DIC: (i) intragranular strain band formation in soft grains (multi-grain strain localization) and (ii) intergranular strain localization (boundary strain localization) at soft-hard boundaries. Crystallographic calculations demonstrate a strong dependence of these mechanisms on the local crystallographic orientations of neighboring α grains. An intragranular strain band results from co-aligning high Schmid factor slip systems between neighboring α grains, whereas a prismatic slip direction aligned near-parallel to a boundary can lead to intergranular (boundary) strain localization. In the latter case, such configuration can facilitate the plastic strain localization in the soft α grain along a boundary due to the lack of barriers for mobile dislocations.

(2) The role of the β phase on the strain localization tendencies is also investigated. The same yield point (measured through *in situ* SXRD testing), the negligible difference in partitioned plastic strain (from *in situ* μ-DIC), and comparable nanohardness

between the phases, indicate the co-deformability of the α and β phases in this alloy; clarifying why local α characteristics govern strain localization tendencies. Nevertheless, the strain hardening of the β phase due to the increase in the dislocation density during the deformation, is a factor that can influence the α strain localization near the α/β interfaces.

(3) Damage evolution curves reveal that the alloy exhibits this long nucleation regime up to the strain level far higher than the onset of plastic instability. The phase boundaries constitute the typical void growth paths. A portion of damage incidents evolves into critical size through a series of coalescence mechanisms: first coalescence of sub-micron voids (propagating along the boundaries) into a micron-scale crack, followed by the coalescence of such micron-size cracks into larger cracks of critical size.

3.9 Appendix

Table 3.2: Statistics of boundary strain localization incidents at soft-soft (S-S) and soft-hard (S-H) boundaries. The strain statistics, e.g., mean and maximum local strain at each incident, were exported from the strain map at $\varepsilon_{\text{avg}} = 0.16$. The boundary angle corresponds to the angle between a boundary where strain localization was observed and the tensile direction measured from the image captured before the deformation.

Incident #	Type	Location	Mean strain	Stdev	Max. strain	Angle (deg)
1	S-S	Center	0.312	0.022	0.363	54.6
2			0.318	0.031	0.418	-
3			0.312	0.022	0.362	54.3
4		Side	0.318	0.025	0.38	40.9
5			0.306	0.019	0.365	46.2
6			0.305	0.016	0.343	10.1
7			0.347	0.043	0.446	51.6
8			0.305	0.022	0.384	47
9			0.294	0.008	0.328	53.3
10			0.308	0.017	0.351	62.2
11			0.288	0.003	0.292	29.6
12			0.298	0.011	0.318	10.8
13			0.3	0.019	0.38	45.5
14	S-H	Center	0.363	0.066	0.552	54.6
15			0.323	0.033	0.435	67.2
16			0.329	0.032	0.404	13.2
17			0.317	0.025	0.373	52.9
18			0.309	0.016	0.342	73.1
19			0.342	0.048	0.461	63.1
20			0.344	0.061	0.522	34.4
21			0.317	0.031	0.404	56.1
22			0.314	0.022	0.354	52.6
23		Side	0.307	0.021	0.37	42
24			0.297	0.012	0.331	11.1
25			0.339	0.047	0.46	-
26			0.36	0.056	0.49	55.6
27			0.307	0.017	0.348	72.2
28			0.326	0.029	0.408	24.1
29			0.302	0.013	0.333	79.1
30			0.315	0.027	0.379	38.9
31			0.354	0.062	0.539	-
32			0.311	0.02	0.387	62.3
33			0.319	0.03	0.446	41
34			0.299	0.012	0.324	17.9

Table 3.3: Schmid factors of basal, prismatic, pyramidal I <a>, and pyramidal I <c+a> slip systems at G1 and G2.

Slip systems		G1	G2
		(330.7°, 144.2°, 26.8°)	(119.4°, 142.5°, 240.8°)
Basal	$(0001)[2\bar{1}\bar{1}0]$	0.39	0.23
	$(0001)[\bar{1}2\bar{1}0]$	0.01	0.26
	$(0001)[\bar{1}\bar{1}20]$	0.37	0.03
Prism	$(01\bar{1}0)[2\bar{1}\bar{1}0]$	0.31	0.44
	$(10\bar{1}0)[\bar{1}2\bar{1}0]$	0.02	0.33
	$(\bar{1}100)[\bar{1}\bar{1}20]$	0.33	0.11
Pyramidal I <a>	$(01\bar{1}1)[2\bar{1}\bar{1}0]$	0.46	0.49
	$(10\bar{1}1)[\bar{1}2\bar{1}0]$	0.02	0.17
	$(\bar{1}101)[\bar{1}\bar{1}20]$	0.11	0.19
	$(0\bar{1}11)[2\bar{1}\bar{1}0]$	0.09	0.27
	$(\bar{1}011)[\bar{1}2\bar{1}0]$	0.01	0.42
	$(1\bar{1}01)[\bar{1}\bar{1}20]$	0.47	0.08
Pyramidal I <c+a>	$(10\bar{1}1)[2\bar{1}\bar{1}\bar{3}]$	0.03	0.12
	$(10\bar{1}1)[11\bar{2}\bar{3}]$	0.04	0.04
	$(01\bar{1}1)[11\bar{2}\bar{3}]$	0.02	0.12
	$(01\bar{1}1)[\bar{1}2\bar{1}\bar{3}]$	0.27	0.14
	$(\bar{1}101)[\bar{1}2\bar{1}\bar{3}]$	0.07	0.21
	$(\bar{1}101)[\bar{2}11\bar{3}]$	0.13	0.15
	$(\bar{1}011)[\bar{2}11\bar{3}]$	0.43	0.07
	$(\bar{1}011)[\bar{1}\bar{1}2\bar{3}]$	0.42	0.15
	$(0\bar{1}11)[\bar{1}\bar{1}2\bar{3}]$	0.10	0.11
	$(0\bar{1}11)[1\bar{2}1\bar{3}]$	0.05	0.26
	$(1\bar{1}01)[1\bar{2}1\bar{3}]$	0.27	0.50
	$(1\bar{1}01)[2\bar{1}\bar{1}\bar{3}]$	0.02	0.46

Table 3.4: Schmid factors of basal, prismatic, pyramidal I <a>, and pyramidal I <c+a> slip systems of grain G.

Slip systems		G
		(77.5°, 24.8°, 285.6°)
Basal	$(0001)[2\bar{1}\bar{1}0]$	0.00
	$(0001)[\bar{1}2\bar{1}0]$	0.07
	$(0001)[\bar{1}\bar{1}20]$	0.08
Prism	$(01\bar{1}0)[2\bar{1}\bar{1}0]$	0.07
	$(10\bar{1}0)[\bar{1}2\bar{1}0]$	0.46
	$(\bar{1}100)[\bar{1}\bar{1}20]$	0.39
Pyramidal I <a>	$(01\bar{1}1)[2\bar{1}\bar{1}0]$	0.06
	$(10\bar{1}1)[\bar{1}2\bar{1}0]$	0.37
	$(\bar{1}101)[\bar{1}\bar{1}20]$	0.30
	$(0\bar{1}11)[2\bar{1}\bar{1}0]$	0.07
	$(\bar{1}011)[\bar{1}2\bar{1}0]$	0.44
	$(1\bar{1}01)[\bar{1}\bar{1}20]$	0.38
Pyramidal I <c+a>	$(10\bar{1}1)[2\bar{1}\bar{1}\bar{3}]$	0.05
	$(10\bar{1}1)[11\bar{2}\bar{3}]$	0.25
	$(01\bar{1}1)[11\bar{2}\bar{3}]$	0.46
	$(01\bar{1}1)[\bar{1}2\bar{1}\bar{3}]$	0.43
	$(\bar{1}101)[\bar{1}2\bar{1}\bar{3}]$	0.17
	$(\bar{1}101)[\bar{2}11\bar{3}]$	0.01
	$(\bar{1}011)[\bar{2}11\bar{3}]$	0.02
	$(\bar{1}011)[\bar{1}\bar{1}2\bar{3}]$	0.21
	$(0\bar{1}11)[\bar{1}\bar{1}2\bar{3}]$	0.37
	$(0\bar{1}11)[1\bar{2}1\bar{3}]$	0.33
	$(1\bar{1}01)[1\bar{2}1\bar{3}]$	0.15
	$(1\bar{1}01)[2\bar{1}\bar{1}\bar{3}]$	0.05

Chapter 4

Mechanical twinning effects

Due to temporally dynamic and spatially discrete lattice reorientation arising from mechanical twinning, identifying the critical micro-mechanisms responsible for heterogeneous deformation is challenging. In this work, employing high-resolution *in situ* microstructure-based digital image correlation (µ-DIC), we investigate the strain localization mechanisms modulated by the activation of $\{10\bar{1}2\}$ extension twinning in a titanium alloy. Our *in situ* observations demonstrate that sharp strain bands formed in an early plasticity regime ($\varepsilon \sim 0.01$) by pyramidal I <c+a> activation can be mitigated by subsequent nucleation and propagation of $\{10\bar{1}2\}$ twins. A significant amount of strain is partitioned into the twin domains due to the massive activation of prismatic <a> system. Although substantial strain heterogeneity develops inside the twin domains, a high capacity to accommodate local shape deformation due to the activated prismatic <a> slip is proposed as a mechanism to delay surface cracking and final failure.

4.1 Introduction

Mechanical twinning is an essential plastic deformation mode in hexagonal closed-packed (HCP) structured metals such as magnesium (Mg), titanium (Ti), zirconium (Zr), and their alloys [130–132]. In such low-symmetry crystal systems, due to the limited number of slip systems for dislocation glide, mechanical twinning is preferred. The temporal evolution and spatial distribution accompanied by twinning have significant impacts on the deformation behaviors of materials, especially on ductility [133–135], formability [91,136,137], fatigue [138–140], and final failure [141,142]. Understanding the heterogeneous deformation arising from the development of the twinning microstructure at the microscopic level is thus of fundamental importance in designing and optimizing the microstructures of HCP metals for enhanced structural properties.

In contrast to the gradual lattice rotation driven by slip [143–145], mechanical twinning causes substantial lattice reorientation in a short period of time. As a result of this abrupt shear deformation, heterogeneous lamellar-shaped domains, or twin domains, of the reoriented lattice form inside the parent HCP grains. Propagation, growth, or thickening of these new domains also gives rise to significant modification of the local or macroscopic texture during deformation [116, 146, 147]. The amount of reorientation of the lattice, often characterized by a misorientation angle between a twin domain and a parent grain, depends on the types of twinning. For example, activation of the $\{10\bar{1}2\}$ extension twin, one of the popular twin types in HCP metals, leads to a considerable reorientation of the lattice, around $\sim 86^\circ$ for Ti alloys with a finite amount of shear strain of ~ 0.17 [130].

Although considerable efforts have been made to understand how the activation and evolution of mechanical twinning can modulate strain hardening behaviors [111, 148, 149], due to the temporally dynamic and spatially discrete nature of mechanical twinning, understanding the development of heterogeneous deformation in the twinning microstructure is challenging. On a microscopic scale, such a texture modification can lead to strain partitioning between parent grains and the twin domains [150–152] as well as local variations of active plasticity mechanisms [153, 154]. This is because mechanical twinning often competes with slip systems having the <c> component, such as pyramidal <c+a> slip systems, and furthermore, twinned domains can experience different slip activity in reoriented grains. Therefore, after twinning, distinct plasticity mechanisms can operate heterogeneously and simultaneously in both the parent grains and the twin domains. Considering the path dependence of plastic deformation, relying on post-mortem characterization of final microstructure cannot provide a complete landscape of the microscopic role of mechanical twinning in controlling strain heterogeneity across the microstructure. All of these challenges also create another knowledge gap on whether mechanical twinning can be beneficial to accommodate local shape deformation, and thus to delay damage processes.

In this work, we study the effects of mechanical twinning on strain heterogeneity, by employing high-resolution *in situ* microstructure-based digital image correlation (µ-DIC). The evolution of the pre- and post-twinning microstructure is characterized in a heavily textured microstructural area of a two-phase titanium alloy. Due to the low content of aluminum and the majority of α crystals preferentially oriented in a hard direction, the selected area is expected to exhibit mechanical twinning. The heterogeneous deformation arising from the activation of the $\{10\bar{1}2\}$ extension twin is resolved temporally and spatially and quantified with respect to the macroscopically applied strain. More specifically, the following questions will be addressed: (i) How does mechanical twinning modulate strain localization mechanisms over deformation? (ii) What is the quantitative contribution of mechanical twinning to the microscopically partitioned strain? (iii) Can the involvement of mechanical twining enhance the damage resistance of titanium alloys?

4.2 Twinning-mediated strain localization process

The initial condition of the microstructure selected for the *in situ* μ-DIC is presented in Figs. 4-1(a_1), (b) and (c). The {0001} pole figure included as an inset of Fig. 4-1(a_1) proves that most of the HCP α crystals are oriented in a direction in which easy slip systems, such as prismatic and basal slip systems, are not favorable. This alloy also contains the β phase, as shown as bright features populated at the boundaries of α grains in Fig. 4-1(b), this β phase is hardly detected on the phase map (Fig. 4-1(c)) due to the limited spatial resolution of EBSD.

A serious of *in situ* strain and [100] IPF maps captured during tensile deformation (Figs. 4-1(a) and (d)) demonstrate that this alloy deforms by mechanical twinning upon tensile loading, although its activation is not observed in the early plasticity regime at $\varepsilon_{avg,xx} = 0.012$ (Fig. 4-1(a_2)). At low strain level, sharp and relatively long strain bands appear across multiple grains, as shown in Fig. 4-1(d_1). After mechanical twinning is activated, thick strain bands corresponding to the twinned domains form and propagate throughout the microstructure (Figs. 4-1(d_2-d_4)). The overall strain level is higher in the twinned domains than in the parent grains. Local strain histograms in Figs. 4-1(e_1-e_4) also reflects this heterogeneous distribution between the parent grains and the twinned domains. The histogram initially shows a single peak as presented in Fig. 4-1(e_1) at at $\varepsilon_{avg,xx} = 0.012$ but it starts to split into two peaks (as highlighted by '●' in Fig. 4-1(e_2) at $\varepsilon_{avg,xx} = 0.057$ and Fig. 4-1(e_3) $= 0.090$) where mechanical twins account for a reasonable portion of the microstructure. In the later stage of deformation, at $\varepsilon_{avg,xx} = 0.160$, as the twins propagate and thicken and thus the fraction of mechanical twins is greater than 40%, the local strain histogram converges to a single peak, as shown in Fig. 4-1(e_4).

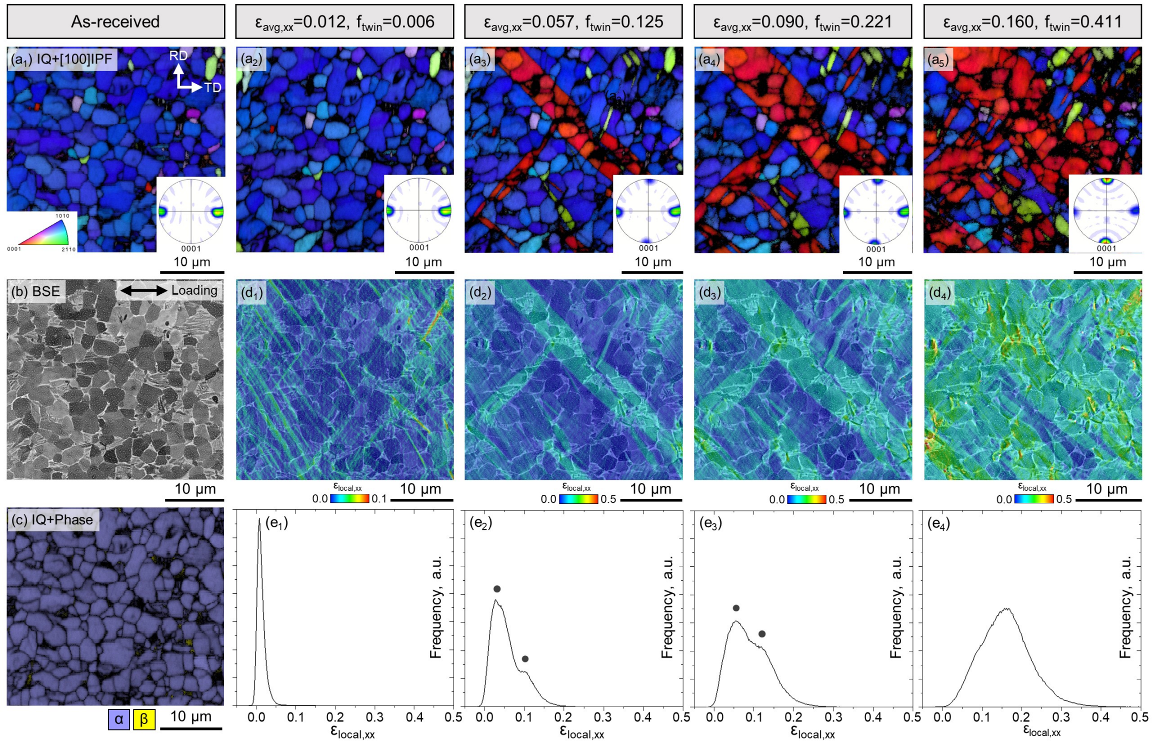

Figure 4-1: *In situ* SEM/EBSD characterization. (a_1) IQ + [100] IPF map, (b_1) BSE micrograph, and (c) phase map of as-received microstructure. (a_2-a_5) IQ + [100] IPF maps, (d_1-d_4) *In situ* local strain ($\varepsilon_{\text{local,xx}}$) maps, and ($e_1$-$e_4$) local strain histograms at the average strain ($\varepsilon_{\text{avg,xx}}$) of 0.012, 0.057, 0.090, and 0.160, respectively. {0001} pole figures are included in each EBSD map, and twin fractions (f_{twin}) at each average strain are shown on the top.

Local strain profiles exported from some of the parent grains and a propagating twin domain in Fig. 4-1 provide detailed features on strain localization in this twinning microstructure. For example, before the twinning is activated, at $\varepsilon_{\text{avg,xx}} = 0.012$, acute strain development is observed along sharp strain bands, as indicated by '∇' in Figs. 4-2(a_1) and (b). The mechanical twinning starts to operate from $\varepsilon_{\text{avg,xx}} \sim 0.03$ and thickens with deformation, leading to a broadening strain band until $\varepsilon_{\text{avg,xx}} \sim 0.10$ as shown in Fig. 4-2(c). However, with increasing deformation levels, substantial local strain concentration appears in the twin domain as shown in the strain maps in Figs. 4-2(a_3-a_5) as well as the local strain profiles in Fig. 4-2(c). Such a salient strain localization mostly develops at the α/β interfaces as shown in Fig. 4-2(a_5). The maximum local strain value is approximately 1.2 at $\varepsilon_{\text{avg,xx}} = 0.301$. No surface cracks are observed until this strain level.

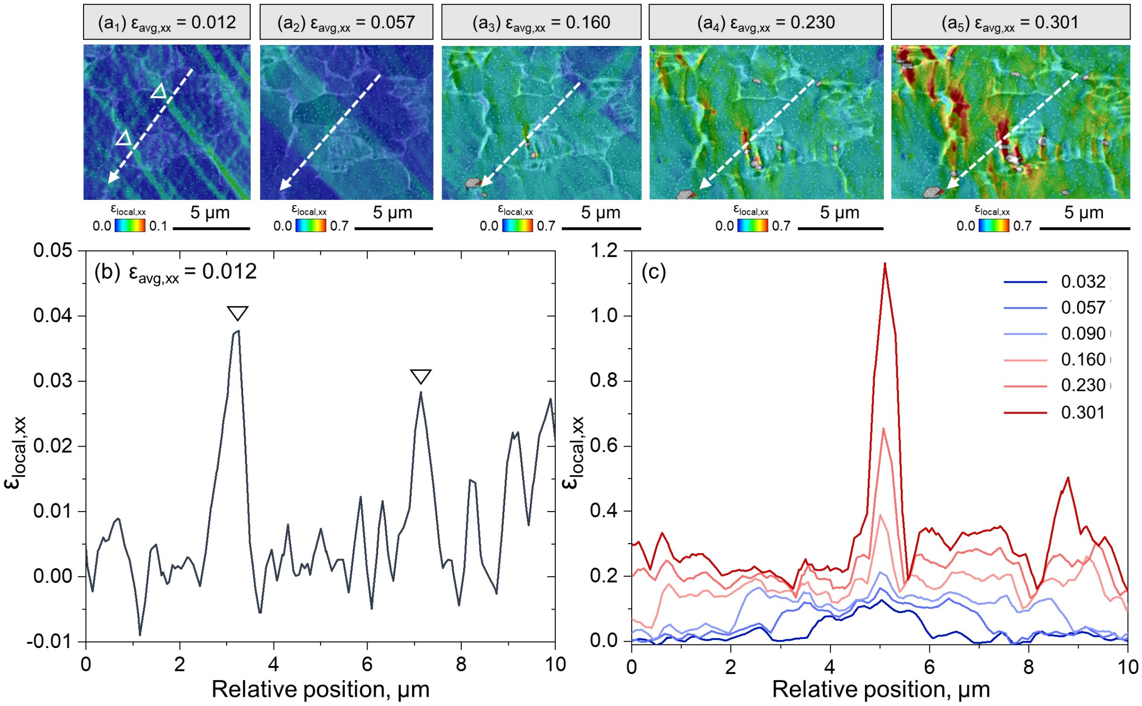

Figure 4-2: Local strain profiles across parent grains and twin domains. *In situ* strain maps at different average strain levels: (a$_1$) $\varepsilon_{avg,xx} = 0.012$, (a$_2$) $\varepsilon_{avg,xx} = 0.057$, (a$_3$) $\varepsilon_{avg,xx} = 0.160$, (a$_4$) $\varepsilon_{avg,xx} = 0.230$, and (a$_5$) $\varepsilon_{avg,xx} = 0.301$. (b) A local strain profile along the arrow in (a$_1$). (c) Local strain profiles exported from the arrows in (a$_2$-a$_5$)

To identify the critical deformation mode that governs the strain localization processes in this microstructure (Figs. 4-1(d$_1$-d$_4$)), detailed crystallographic calculations were performed on the local area shown in Fig. 4-3(a). The potential slip and twin traces, as well as corresponding Schmid factors (SFs), were calculated based on a set of Euler angles exported from the positions (P1, P2, and P3) marked in Figs. 4-3(b$_1$)-(b$_3$). The simulated traces were compared with the slip and twin traces observed experimentally. The results shown in Figs. 4-3(c$_1$)-(c$_3$) show that the sharp strain bands observed in the early plastic regime (Fig. 4-3(a$_1$)) arise from the activation of pyramidal I <c+a> slip systems (Fig. 4-3(c$_1$)). The twin trace shown in Fig. 4-3(a$_2$) indicates that the formation of thick strain band (Fig. 4-3(a$_2$)) is attributed to the activation of a $\{10\bar{1}2\}$ extension twin, more specifically $(\bar{1}102)[1\bar{1}01]$ variant. The characteristic amount of reoriented lattice due to $\{10\bar{1}2\}$ twin activation is $\sim 85°$ and as a result, the prismatic slip can be favored in the twinned domains. Therefore, in the later stage of deformation, the strain localization process is mostly controlled by heterogeneous deformation caused by prismatic slip activation (Fig. 4-3(c_3)). Significant strain concentration is observed at the locations where the prismatic slip traces intersect phase boundaries, but no surface cracking is found until $\varepsilon_{avg,xx} = 0.293$.

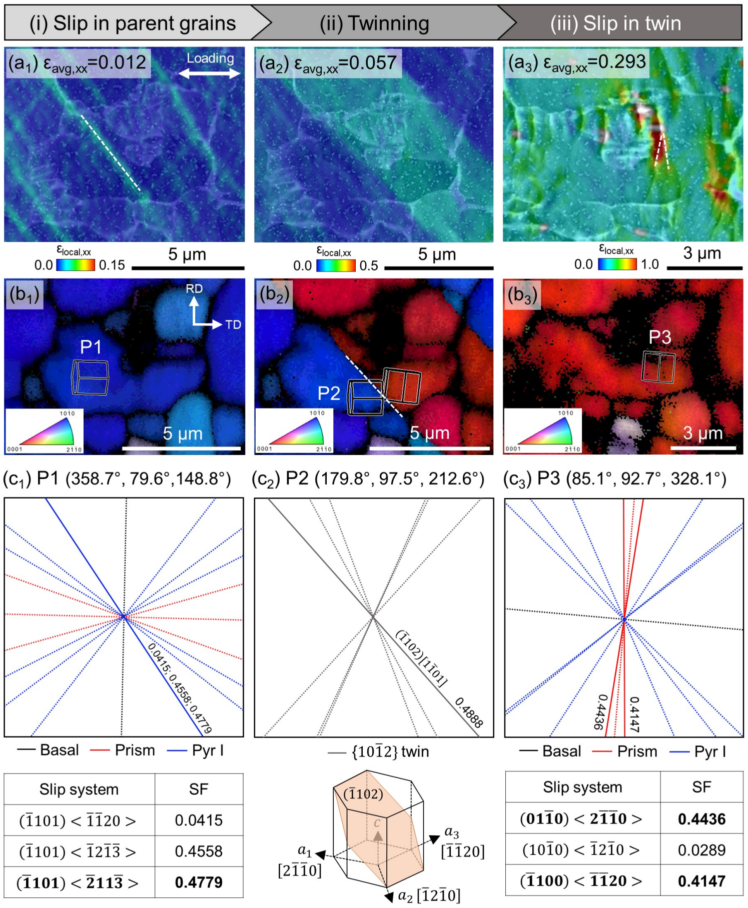

Slip system	SF
$(\bar{1}101) < \bar{1}\bar{1}20 >$	0.0415
$(\bar{1}101) < \bar{1}2\bar{1}\bar{3} >$	0.4558
$(\bar{1}101) < \bar{2}11\bar{3} >$	**0.4779**

Slip system	SF
$(01\bar{1}0) < 2\bar{1}\bar{1}0 >$	**0.4436**
$(10\bar{1}0) < \bar{1}2\bar{1}0 >$	0.0289
$(\bar{1}100) < \bar{1}\bar{1}20 >$	**0.4147**

Figure 4-3: Twin-mediated modulation of strain localization mechanisms. (a) *In situ* local strain ($\varepsilon_{local,xx}$) and (b) EBSD [100] IPF maps at $\varepsilon_{avg,xx}$ of (a_1-b_1) 0.012, (a_2-b_2) 0.057, and (a_3-b_3) 0.293. Euler angles exported at three different points, P1 in (b_1), P2 in (b_2), and P3 in (b_3), and calculated slip or $\{10\bar{1}2\}$ twin traces are shown in (c_1-c_3), respectively.

4.3 Quantitative evaluation of local strain contributors

The crystallographic analyses shown in Fig. 4-3 demonstrate that the strain patterning of this microstructure experiences considerable changes with increasing strain levels as different plasticity modules, such as pyramidal I <c+a> slip, $\{10\bar{1}2\}$ twin, and prismatic <a> slip, are activated consecutively during the course of deformation. As a result of these sequential activations, the local strain of the microstructure is the summation of the local strain accumulated by these three mechanisms. To quantitatively assess the contribution of each deformation mechanism to the local strain measured in a sample frame, the twinning shear should be converted to the sample frame by a series of coordinate transformations as described below (Fig. 4-4).

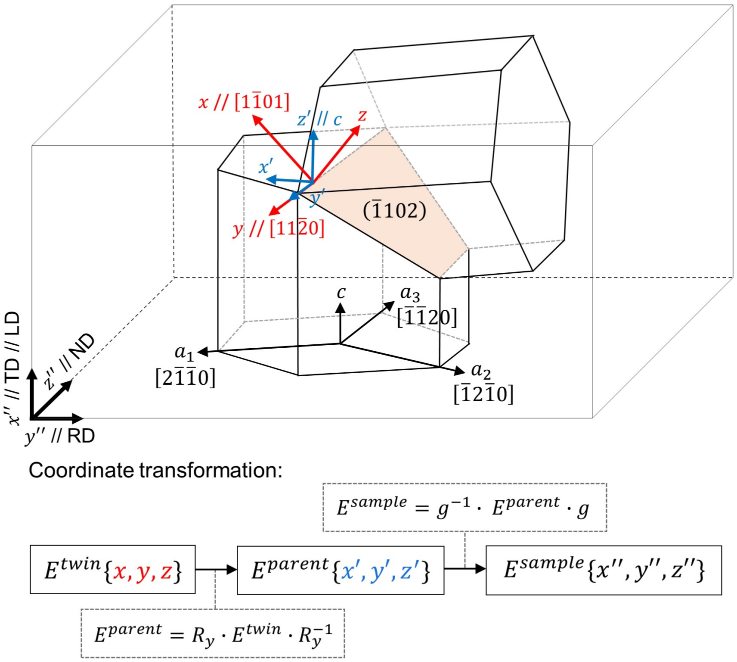

Figure 4-4: Coordinate transformation of $\{10\bar{1}2\}$ twinning shear from the twin reference frame, $\mathbf{E}^{\mathbf{twin}}\{x, y, z\}$ to the sample reference frame $\mathbf{E}^{\mathbf{sample}}\{x'', y'', z''\}$.

First, the twinning shear of the $(\bar{1}102)[1\bar{1}01]$ variant is defined in a twin reference frame, i.e., $\mathrm{E}^{\mathrm{twin}}\{x, y, z\}$, which is colored red in Fig. 4-4. The definition of a shear displacement gradient tensor is presented in Eqn. 4.1.

$$\mathbf{E} = e_{ij} = \begin{bmatrix} e_{xx} & e_{xy} & e_{xz} \\ e_{yx} & e_{yy} & e_{yz} \\ e_{zx} & e_{zy} & e_{zz} \end{bmatrix} \tag{4.1}$$

For the $(\bar{1}102)[1\bar{1}01]$ extension twin variant, the **x**-axis is the shear direction (i.e., $[1\bar{1}01]$), the **y**-axis is perpendicular to the shear direction and the habit plane normal, and the **z**-axis is the habit plane normal. Therefore, the displacement gradient tensor for the twinning shear can be expressed in a twin reference frame as follows.

$$\mathbf{E}^{twin} = \begin{bmatrix} 0 & 0 & s \\ 0 & 0 & 0 \\ 0 & 0 & 0 \end{bmatrix} \tag{4.2}$$

where s is the twining shear, commonly calculated by $s = \cot\theta$ with a misorientation angle, θ.

Next, the displacement gradient tensor expressed in the twinning reference frame is converted into the reference frame of the parent grain by applying a rotation operation. In the reference frame of the parent grains (i.e., $\mathrm{E}^{\mathrm{parent}}\{x', y', z'\}$), the $\mathbf{x}'$-axis is the prism plane normal, the $\mathbf{y}'$-axis is parallel to the **y**-axis, and the $\mathbf{z}'$-axis is the c-axis of an HCP crystal (i.e., [0001]). Based on a right-handed coordinate system with counterclockwise rotation, the rotation matrix, $\mathbf{R_y}$, which rotates the direction of twinning shear (i.e., $[1\bar{1}01]$) into the corresponding prismatic plane normal direction (i.e., $[1\bar{1}00]$) around the shared **y**-axis (or equivalently, $\mathbf{y}'$-axis) can be expressed as follows.

$$\mathbf{R_y} = \begin{bmatrix} \cos(\theta/2) & 0 & \sin(\theta/2) \\ 0 & 1 & 0 \\ -\sin(\theta/2) & 0 & \cos(\theta/2) \end{bmatrix} \tag{4.3}$$

Thus, the displacement gradient tensor for twinning shear in the parent grain reference frame is the following:

$$\mathbf{E^{parent}} = \mathbf{R_y} \cdot \mathbf{E^{twin}} \cdot \mathbf{R_y^{-1}} \tag{4.4}$$

Finally, by applying a coordinate transformation matrix ($\mathbf{g}\{\boldsymbol{\varphi_1}, \phi, \boldsymbol{\varphi_2}\}$) in Eqn. 4.5, which follows Bunge's convention [155], the gradient tensor can be transformed from the parent grain reference frame ($\mathrm{E}^{\mathrm{parent}}\{x', y', z'\}$) to the sample reference frame ($\mathrm{E}^{\mathrm{sample}}\{x'', y'', z''\}$). As a result, in the final coordinate frame, the $\mathbf{x}''$-, $\mathbf{y}''$-, and $\mathbf{z}''$-axes are parallel to the transverse direction (TD), the rolling direction (RD), and the normal direction (ND), respectively, as shown in Fig. 4-4. Note that the tensile deformation is performed in the transverse direction.

$$\mathrm{g}\{\varphi_1,\phi,\varphi_2\} = \begin{bmatrix} \cos\varphi_1\cos\varphi_2 - \sin\varphi_1\sin\varphi_2\cos\phi & \sin\varphi_1\cos\varphi_2 + \cos\varphi_1\sin\varphi_2\cos\phi & \sin\varphi_2\sin\phi \\ -\cos\varphi_1\sin\varphi_2 - \sin\varphi_1\cos\varphi_2\cos\phi & -\sin\varphi_1\sin\varphi_2 + \cos\varphi_1\cos\varphi_2\cos\phi & \cos\varphi_2\sin\phi \\ \sin\varphi_1\sin\phi & -\cos\varphi_1\sin\phi & \cos\phi \end{bmatrix} \tag{4.5}$$

In summary, the displacement gradient tensor in the sample reference frame is calculated as follows.

$$\mathbf{E_{sample}} = \mathbf{g^{-1}} \cdot \mathbf{E_{parent}} \cdot \mathbf{g} \tag{4.6}$$

or, equivalently,

$$\mathbf{E_{sample}} = \mathbf{g^{-1}} \cdot \mathbf{R} \cdot \mathbf{E_{twin}} \cdot \mathbf{R^{-1}} \cdot \mathbf{g} \tag{4.7}$$

In this analysis for the $\{10\bar{1}2\}$ twin, s in Eqn. 4.2 corresponds to 0.172, based on $\theta = 85.1^\circ$ and $(\varphi_1, \phi, \varphi_2) = (358.7^\circ, 79.6^\circ, 148.8^\circ)$, both of which were measured by EBSD. The final strain tensor of the $(\bar{1}102)[1\bar{1}01]$ twinning shear in the sample reference frame calculated by Eqn. 4.7 is shown in Eqn. 4.8, indicating that the strain component corresponding to the $\mathbf{x}''$-axis (along the loading direction) is 0.0624 (∼6%).

$$\mathbf{E_{sample}} = \begin{bmatrix} 0.0624 & 0.0681 & -0.0502 \\ -0.0761 & -0.0831 & 0.0613 \\ -0.0258 & -0.0281 & 0.0207 \end{bmatrix} \tag{4.8}$$

Based on this calculated value, the amount of local strain originating from the activation of the $(\bar{1}102)[1\bar{1}01]$ twin variant can be separated from the total local strain. Three local positions, A, B, and C, highlighted in the inset of Fig. 4-5 were subjected to calculation. Note that this area is identical to the one in which crystallographic evaluations were performed (Fig. 4-3). Location A shows the activation of the $(\bar{1}102)[1\bar{1}01]$ twin at $\varepsilon_{\mathrm{avg,xx}} = 0.011$, and this twin thickens in the direction marked as an arrow as the deformation proceeds. Area B becomes a twinned domain at $\varepsilon_{\mathrm{avg,xx}} = 0.087$, while area C never shows mechanical twinning and thus remains as a parent grain. The representative strain values of areas A, B, and C were calculated by averaging the five local strain values obtained from the point measurements at each location. As shown in Fig. 4-5(a), area A exhibits a sharp increase in local strain after mechanical twinning, while the local strain of area B exhibits a mild increase after twinning. The curve C in Fig. 4-5(a) indicates that the local microstructural area C can continue to deform without mechanical twinning, but the amount of local strain increase is much smaller than the other two regions, e.g., A and B.

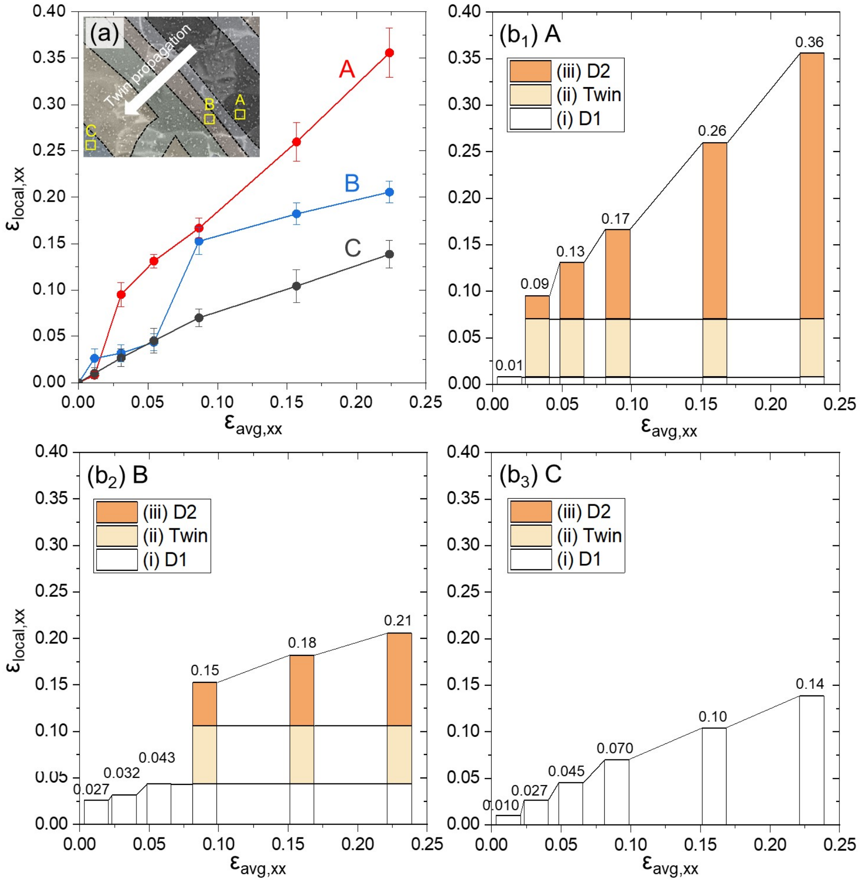

Figure 4-5: Quantitative evaluation of the contributions of different plasticity mechanisms to local strain. (a) Local strain evolution of three locations (A, B, and C) marked in the inset BSE micrograph. Local strain evolution plots decomposed into the following three plasticity components: (i) dislocation plasticity before mechanical twinning (D1), (ii) $(\bar{1}102)[1\bar{1}01]$ mechanical twinning (Twin), and (iii) dislocation plasticity after mechanical twinning (D2) at (b$_1$) A, (b$_2$) B, and (b$_1$) C.

The total local strain value can be decomposed into the following three plasticity components: (i) dislocation plasticity before mechanical twinning, primarily pyramidal I <c+a> slip (D1), (ii) $(\bar{1}102)[1\bar{1}01]$ mechanical twinning (Twin), and (iii) dislocation plasticity after mechanical twinning, mostly prismatic <a> slip (D2). Figs. 4-5(b$_1$-b$_3$) show how much each mechanism contributes to the local strain component along the loading direction measured by µ-DIC. For area A, the contribution of the twinning is approximately 17%, while the twinning accounts for about 29% in the case of area B. Area B has a higher fraction of D1 compared to A, almost four times greater, indicating that area B continues to deform with the aid of dislocation plasticity before becoming a twinned domain. Furthermore, the local strain of area A exhibits a sharp increase after twinning and, as a result, most of the local strain is accommodated by the prismatic slip (D2) after the twinning. Note that this accelerated local strain evolution occurs concurrently with the thickening of the twin. Without mechanical twinning, the overall strain is limited, as shown in Fig.4-5(c).

4.4 Roles of mechanical twinning in enhancing damage resistance

The results in Fig. 4-2 demonstrate substantial accumulation of strain in a local area of the twinned domain. As seen from the strain profile in Fig. 4-2(c), for instance, the local deformation level can reach almost 1.2 at $\varepsilon_{\mathrm{avg,xx}}$ ~0.301 without the sign of surface cracking. This may suggest that the occurrence of mechanical twinning can potentially improve the ability of the microstructure to accommodate local shape deformation, and thus lead to enhanced damage resistance. The $\{10\bar{1}2\}$ twin can be a good example to evaluate this hypothesis, since it reorients the lattice almost by 90°, and thus, comparing the evolution of the average damage size of the samples loaded along the transverse (favoring twinning) and rolling (unfavoring twinning) directions can provide some indication of whether mechanical twinning can bring such a benevolent effect.

Fig. 4-6(a) shows the optical images of the tensile samples strained along the rolling direction (RD in Fig. 4-6(a_1)) and the transverse direction (TD in Fig. 4-6(a_2)). These images were captured right before the fracture at a frame rate of 5 Hz. The TD sample clearly shows localized necking as marked by an arrow in Fig. 4-6(a_2) while a relatively diffuse neck is observed in the RD sample. The strain profiles

($\varepsilon_{avg,xx}$) along the neck region also exhibit a higher value of the maximum strain in the TD sample. The evolution of the average damage size as a function of the average strain along the gauge measured by the optical DIC shows that the onset of substantial damage evolution is delayed to the average strain greater than 0.8 in the presence of twinning. On the other hand, without mechanical twinning, the damage nucleates and grows in a much earlier strain, about 0.3 of the average strain for the RD sample.

Note that whether mechanical twinning is benevolent or not also depends on many other factors, such as the types and strain hardening capacity of twins and favored slip systems in a twin domain. Characteristics of grain or phase boundaries are also considered important in determining the transmission of twinning [112]. However, our results suggest that in the case where twinning can modulate the texture of the microstructure in a way that it has a texture component that has a higher capacity to accommodate local shape deformation, the resistance of the microstructure to damage nucleation can be effectively improved. These are the first investigations demonstrating such an effect, and thus further analyses are needed to confirm the influence of other effects.

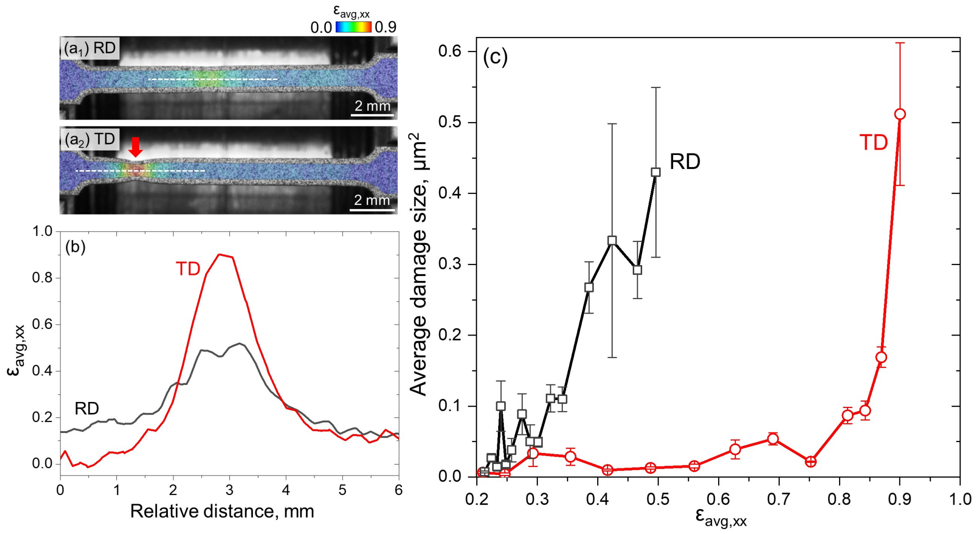

Figure 4-6: Dependency of initial texture on damage evolution of the alloy. Optical images of the tensile samples loaded along (a_1) rolling direction (RD) and (a_2) transverse direction (TD). These images were taken right before fracture at a rate of five frames per second (FPS). (b) Profiles of average strain in a loading axis ($\varepsilon_{avg,xx}$) exported along the white dotted lines in the gauge of the two samples in (a). (c) Evolution of average damage size in μm^2.

4.5 Conclusion

In this study, we identify the temporally and spatially modulated strain localization mechanisms due to the activation of the $\{10\bar{1}2\}$ mechanical twinning by high-resolution *in situ* microscopic strain mapping. In the early plasticity regime ($\varepsilon_{\mathrm{avg,xx}} \sim 0.01$), the activation of pyramidal I <c+a> slips leads to the formation of sharp strain bands along its slip traces. The occurrence of the $\{10\bar{1}2\}$ twins results in thick strain localization bands that propagate to other microstructural areas at higher length scales. Strain partitioning is also observed between parent grains and twin domains. Due to the significant reorientation of the lattice accompanied by the $\{10\bar{1}2\}$ extension twinning, prismatic <a> slip is preferred in twin domains. Vertical strain bands can form as a consequence of prismatic slip activation, but the local strain is concentrated mostly at phase interfaces in a point-wise manner. The quantitative contribution of the $(\bar{1}102)[1\bar{1}01]$ twinning shear is approximately 6% of the local strain along the loading direction. Although substantial strain localization is captured at the phase interfaces as a result of prismatic slip activation, in general, the high capability of accommodating local shape deformation of this slip system can have a potential to improve the damage resistance of this microstructure.

Chapter 5

Phase transformation effects

In most transformation-induced plasticity (TRIP)-assisted steels, identifying critical factors that govern mechanically induced martensitic transformation (MIMT) is challenging, due to the presence of multiple phase constituents and difficulties in spatially and temporally resolving transformation of sub-micron scale retained austenite. In this chapter, by combining microstructural information analyzed from *in situ* SEM/EBSD and *in situ* synchrotron XRD tensile experiments and phase-specific nanoindentation measurements, we explore neighborhood effects on pre- and post- mechanically induced martensitic transformation in a ferrite-containing QP steel that consists of ferrite (F), bainite (B), tempered martensite (TM), fresh martensite (FM), and retained austenite (RA). Local strains of RA and mechanically induced martensite (MM) at different locations are resolved at different strain levels. Our results demonstrate that RA in F is more stable than RA in B/TM matrices, where the mechanical strengths of RA and B/TM are comparable. The strain distribution inside F is highly heterogeneous, which leads to the distinct stability of RA in F. Strain localization and damage micro-mechanisms of this alloy were also explored, indicating a detrimental role for FM in promoting strain heterogeneity between the F and FM interfaces, and thus cracking.

This chapter contains contents adapted from J. Kang et al., Neighborhood effects on mechanically induced martensitic transformation: An *in situ* investigation in a ferrite-containing QP steel, *Submitted*, 2022.

5.1 Introduction

Transformation-induced plasticity (TRIP)-assisted multiphase microstructure design has been used as a key strategy in the development of advanced high-strength steels (AHSSs) [17, 156–159]. Third-generation AHSSs are generally TRIP-assisted steels consisting of different volumes of ferrite, martensite, bainite, and retained austenite [160–163]. The fraction of retained austenite is normally in the range of 10-20 vol.% [164–166], and the so-called TRIP effects in these steels arise from the diffusionless shear transformation of retained austenite to martensite during the course of deformation. This mechanically induced martensitic transformation (MIMT), which is either stress-driven [167–170] or strain-induced [171–173], provides additional strain hardening capability, enabling design of high-strength and high-formability steels [174–176]. Controlling the mechanical stability of retained austenite has become a central issue in this context because both early consumption and excessive stabilization of retained austenite lead to unoptimized strain hardening capacity and eventually to early plastic instability. [177–180]. Considerable research has been conducted to evaluate the microstructural factors that controls mechanical stability of retained austenite and revealed substantial effects of (i) elemental partitioning, (ii) size and morphology, (iii) orientation, and more recently, (iv) micromechanical influence of surrounding microstructure.

The elemental effects on the stability of retained austenite have been extensively studied in relation to optimization of martensite start (M_s) temperature [181–184]. In most low-alloyed TRIP steels, partitioning of carbon (C) into austenite is encouraged, due to its substantial influence on decreasing M_s temperature [185–188]. The role of manganese (Mn) has also been explored in depth [189–192], although Mn is generally believed to be immobile at low temperatures (350-450 °C) [193, 194]. Other substitutional elements such as silicon (Si) and aluminum (Al) are added to inhibit the precipitation of carbides and thus increase the stability of retained austenite [17, 195–197]. Also, (ii) size and morphology dependencies are in part correlated with the C partitioning effects. Two types of retained austenite have been highlighted due to their distinct characteristics: interlath retained austenitic films (20-200 nm in width) and blocky retained austenite ($\geq$ 200 nm in size). The high surface-to-volume ratio and C transfer from surrounding martensite rich in C have been considered the main causes of the high stability of the interlath retained austenite [198–200]. (iii) The crystallographic orientation of retained austenite is also perceived as a critical factor in deciding its stability, and, for example, high mechanical stability can be achieved for the retained austenite grains whose $\{111\}$ plane normal is closely aligned with the loading direction. [42, 201–203]

The latest advancement of *in situ* SEM/EBSD-based tensile deformation and microscopic strain mapping techniques [33, 36, 39, 204] has increased attention to the effects of the non-uniform strain distribution. The microstructure of most TRIP-assisted steels is a mixture of a mechanically soft phase (allotriomorphic ferrite) and hard phases (martensite or bainite) [205–207], and as a result of different mechanical properties between these phases, the amount of plastic strain partitioned into phases varies significantly [208–210]. Increasing numbers of studies have inspected such micromechanical roles in determining the mechanical stability of retained austenite [211–215], revealing that the local strain partitioned into martensitic matrices decides whether the surrounding retained austenite transforms or not [193, 194, 216]. However, these *in situ* investigations also report highly conflicting results regarding the strain evolution of retained austenite. Salehiyan et al. [217] and Tan et al. [193, 194], for example, observed limited strain partitioned into retained austenite, while Wang et al. observed a substantial amount of strain carried by retained austenite in martensitic matrices [218]. Given the numerous microstructural factors that can also compete with each other depending on thermomechanical histories, having a complete picture of what actually governs the stability of retained austenite during deformation still remains a challenge. Note that this is in part due to technical difficulties in *in situ* tracking of sub-micron scale retained austenite and mapping its strain with proper resolution. The presence of multiple phases in different volumes and configurations also increases complexity, hindering systematic evaluation of the individual effects. Furthermore, such challenges regarding understanding the retained austenite behaviors create similar difficulties in understanding the behavior of mechanically induced martensite, which is essential in the later stage of deformation as ductile damage develops. An improved understanding of the characteristics of both retained austenite and mechanically induced martensite is thus beneficial for toughness of steels as well.

In this study, we carried out comprehensive microstructural investigations with *in situ* high resolution SEM/EBSD-based microscopic digital image correlation (µ-DIC) and *in situ* synchrotron X-ray diffraction (SXRD), to fill these gaps in our understanding. More specifically, the following questions will be addressed. First, what is the micromechanical role of neighborhood microstructure in determining the mechanical stability of retained austenite? Second, how does the strain accommodating capability of mechanically induced martensite depend on its surroundings? More quantitatively, how does the strain partitioned into mechanically induced martensite vary with its locations? Finally, in this kind of TRIP-assisted multi-phase steels, what are the critical strain localization mechanism and microstructural configuration that result in cracking? The study was carried out on a QP steel that contains multiple microstructural constituents such as ferrite, bainite, tempered martensite, fresh martensite, and retained austenite. The pre- and post-transformation behaviors of retained austenite were resolved and analyzed by µ-DIC. Our results demonstrate strong micromechanical influences on the mechanical stability of retained austenite that can even exceed the elemental partitioning or orientation effects and further reveal the critical role of ferrite in controlling the transformation. On the basis of our observations, microstructure design strategies to further optimize strength-ductility combinations by better control of MIMT will be proposed.

5.2 Characterization of as-received microstructure

The detailed characterization results summarized in Fig. 5-1 reveal the as-received microstructure of the ferrite-containing QP steel in the study is a mixture of multiple phase constituents including the metastable retained austenite. Its mechanical properties are also shown in Fig. 5-2 and shared in the caption. Fig. 5-1(a) shows the phase map obtained from EBSD, which highlights the RA as green and the rest of the BCC/BCT phases as red. The orientations of all the phases are shown in Fig. 5-1(b). In total, the four microstructure constituents are identified and subjected to investigation: ferrite (F), bainite and tempered martensite (B/TM), fresh martensite (FM), and retained austenite (RA). Note that B and TM are grouped into one category, referred to as B/TM, since the spatial resolution of SEM imaging is insufficient to distinguish lower bainite and tempered martensite under the imaging conditions adopted for the *in situ* characterization. The BSE micrograph shown in Fig. 5-1(c) shows the detailed features of how these four identified microstructure groups are distributed.

In this work, a BSE image, and EBSD phase and image quality (IQ) maps were employed for accurate measurements of fraction and size of the four microstructural components. For instance, F and FM phases were manually separated from the BSE image using Adobe Photoshop 2021, while the area fraction of RA was obtained from the EBSD dataset calculated in OIM software. However, note that, despite nital etching, complete separation of RA from B/TM is still challenging in the spatial resolution where we performed the *in situ* SEM characterization. Thus, the area fraction of B/TM was calculated by subtracting the fraction of RA from the summed fraction of B/TM and RA. Unidentified points were excluded from the phase fraction statistics. The sizes of F and RA grains and FM islands were measured by BSE (for FM islands) and EBSD (for F and RA grains). Specifically, the number of pixels of each island or grain was first exported from BSE or EBSD images and converted to the area (µm^2). The sizes were calculated from the area under the assumption that the grains or islands are circular.

Figs. 5-1(d)-(g) shows the fractions of the four microstructural constituents (i.e., F, B/TM, FM, and RA) and their distributions in the microstructure. In this local area, the area fractions of F, B/TM, FM, and RA is 45.5%, 32.3%, 5.5%, and 10.1% as also summarized in Table 5.1. A couple of precautions are needed to have a correct interpretation of the RA fraction in this analysis. First, the RA discussed in this study, unless specified, represents blocky RA only, as capturing the thin-film RA, is in general beyond the resolution of EBSD. The total amount of RA including both blocky and thin-film RA can be measured by SXRD, which will be discussed later in Section 5.3. Second, the RA fraction (10.1%) shown in Fig. 5-1 is the area fraction calculated from the EBSD measurement of the microstructural area selected for the *in situ* SEM characterization. Note that this area is etched to facilitate phase boundary detection. The actual average fraction of RA in this alloy can be better estimated by EBSD on an as-polished surface, without etching, in multiple locations. The average value of RA obtained from five EBSD measurements at different positions suggests that the actual RA fraction in this material can be 11.4% (± 1.2), which is slightly higher than 10.1%.

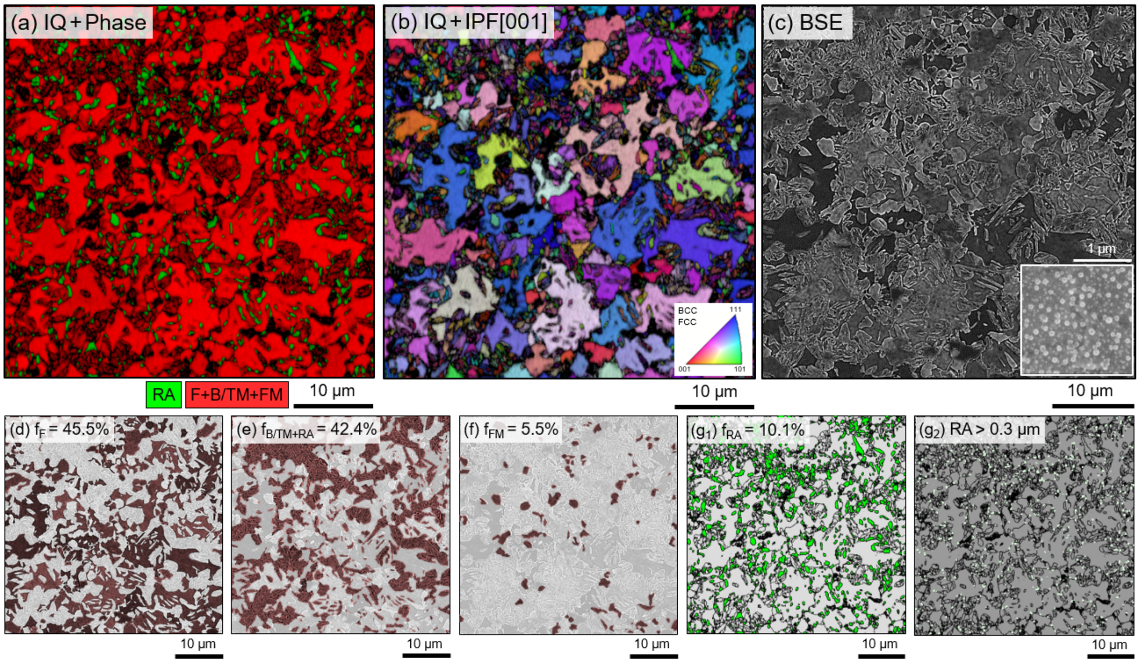

Figure 5-1: Characterization of as-received microstructure. (a) IQ + Phase and (b) IQ + IPF [001] maps and (c) BSE micrograph of the initial microstructure selected for *in situ* SEM/EBSD characterization. The in-beam SE image in the inset of (c) shows the distribution of colloidal silica particle employed for the µ-DIC. The phase separation results showing (d) ferrite (F), (e) bainite (B), tempered martensite (TM), and retained austenite (RA), and (f) fresh martensite (FM). The microstructural area that belongs to each phase is highlighted in the BSE images. Note that the image (e) includes both B/TM and RA since despite etching the boundaries between RA and B/TM remain unclear. (g) EBSD phase maps of (g_1) all RA grains (green) and (g_2) RA whose grain size is larger than 0.3 µm (white).

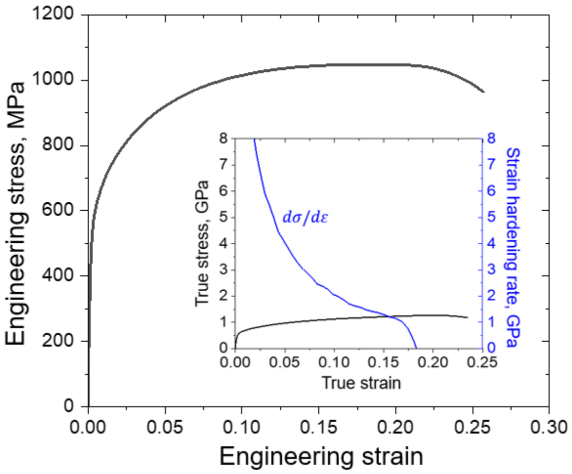

Figure 5-2: Room-temperature mechanical property of the QP steel. Engineering stress-strain curve (617 MPa yield strength, 1048 MPa ultimate tensile strength, 18.4% uniform elongation. The inset shows the true stress-strain curve with the strain hardening rate (dσ/dε).

Table 5.1: Abbreviation and area fraction of the microstructural constituents of as-received QP steel.

Phase	Abbreviation	Fraction, %
Ferrite	F	48.7
Bainite, tempered martensite, and retained austenite	-	45.4
Bainite and tempered martensite	B/TM	35.3
Fresh martensite	FM	5.9
Retained austenite	RA	10.1

Also, the EBSD phase map in Fig. 5-1(a) shows that the RA grains in this material are well distributed throughout the microstructure, embedded in different phases. Although not fully homogeneously dispersed, a statistically sufficient amount of RA is found in different surroundings, for example, in F, in B/TM, or next to FM. The area fraction of the retained austenite enclosed by F grains is about 25% of all RA present in the microstructure. Based on its surroundings, RA can be categorized into the following three types: (i) retained austenite embedded in ferrite grains (RA in F), (ii) retained austenite enclosed by bainite and tempered martensite regions (RA in B/TM), and (iii) retained austenite located next to fresh martensite (RA next to FM).

The representative sizes of the microstructural constituents in this microstructure were also quantified. Table 5.2 includes the summarized result of the average sizes of

FM islands (1.45 ± 0.49 µm), F grains (3.24 ± 1.87 µm), and RA (0.36 ± 0.23 µm). Note that the standard deviation of the size of the F grains is relatively high, due to the presence of large F grains (> 5µm), although the number of such large F grains is limited. Furthermore, an interesting observation is that the size of RA varies with its location. The average grain size of the RA embedded in F grains is found to be larger (0.66 ± 0.0.16 µm) in general compared to the average size of the total RA in the microstructure (0.36 ± 0.23 µm).

Table 5.2: Average size of fresh martensite island and ferrite and retained austenite grains.

Phase		Size, µm
Fresh martensite island		1.45 ± 0.49
Ferrite grain		3.24 ± 1.87
Retained austenite	All grains	0.36 ± 0.23
	Embedded in ferrite grains	0.66 ± 0.16

Furthermore, nanohardness measurements performed on these four microstructural constituents, i.e., F, B/TM, FM, and RA, reveal a wide spectrum of their mechanical strength. For example, the nanohardness distribution in Fig. 5-3(a) indicates that F is the softest, FM is the hardest, and B/TM is in between. RA exhibits hardness values similar to those of B/TM. Note that post-EBSD characterization confirms that no transformation occurred during the indentation, which suggests that the transformation effects are not included in the measured hardness of RA. However, this is, of course, within the resolution of EBSD. Therefore, the nanohardness values of RA measured in this work can be safely assumed to represent RA only since much higher values, close to those of FM, would be achieved (based on the measured nanohardness of FM) if RA transforms to martensite upon indentation [206]. The Box-and-whisker plot in Fig. 5-3(b) also confirms that there is little overlap between the nanohardness values except for RA and B/TM. The values inside the box are within the first quartile and the third quartile (i.e. 25-75 percentile), the whiskers indicate 10 percentile and 90 percentile, and the horizontal line (or the red diamond symbol) in the box corresponds to the mean. Slightly low average nanohardness is observed in RA in comparison to that of B/TM, but, in general, the values of RA and B/TM are in the comparable range. The indentation results are summarized in Tab 5.3, including the number of indents considered to calculate the average nanohardness values and the resulting ratio of the values. The hardest phase, FM, has about two times higher nanohardness value (10.3 ± 0.9) than F (4.7 ± 0.4), while that of B/TM (6.7 ± 0.7) is 1.4 times higher. These measured values are in the range of previously reported values in steels with a similar C content [219–221]. Moreover, although the nanoindentation of RA in the literature often shows largely scattered values depending on its fraction, morphology, and composition [207, 221–223], the real nanohardness values of RA are considered between those of martensite and ferrite [224–227].

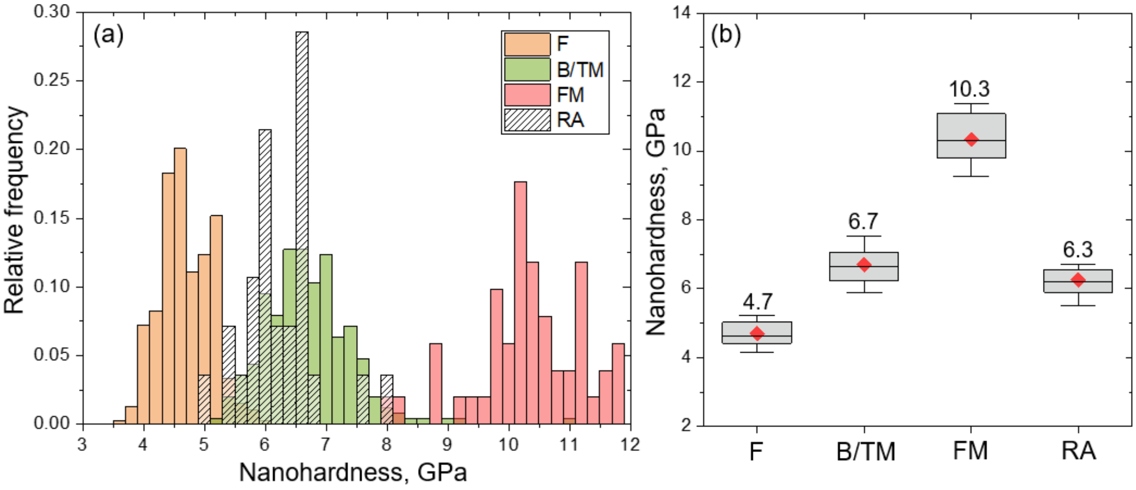

Figure 5-3: Nanohardness values of ferrite (F), bainite and tempered martensite (B/TM), fresh martensite (FM), and retained austenite (RA). Nanohardness distribution shown in (a) relative frequency histogram and (b) Box and Whisker Plot. The box are drawn from the first quartile to the third quartile (i.e. 25-75 percentile), the whiskers represents 10 percentile and 90 percentile, and the horizontal line (or red diamond symbol) corresponds to the mean of each dataset.

Table 5.3: Summary of nanohardness measurements. Number of indents, average nanohardness values, and their ratios.

Phase	# of indents	H_{nano}, GPa	H_{nano} ratio
F	389	4.7 ± 0.4	1
B/TM	252	6.7 ± 0.7	1.4
FM	51	10.3 ± 0.9	2.2
RA	28	6.3 ± 0.6	1.3

5.3 *In situ* SEM/EBSD/SXRD tensile deformation

The *in situ* SEM/EBSD characterization coupled with µ-DIC was carried out on the microstructure shown in Fig. 5-1 to study the influences of neighborhood microstructure on the behaviors of RA and mechanically induced martensite. The local strain maps of corresponding deformation stages were calculated by correlating a series of in-beam SE images in GOM Correlate software with facet size and facet distance of 366 nm (30 pixels) and 122 nm (10 pixels), respectively. The SXRD experiments were performed to monitor the global transformation of RA in the alloy, including both blocky and thin-film RA, as a function of applied strain. In this section, we elaborate the comprehensive results of these two *in situ* experiments with a particular focus on the following three aspects: (i) strain partitioning, (ii) retained austenite transformation, and (iii) surface cracking.

Strain partitioning

An important aspect of this study is to find a quantitative correlation between the macroscopically applied strain and the microscopically partitioned strain. Besides engineering strain ($\varepsilon_{\mathrm{eng}}$) to plot a stress-strain curve, in the following text, local strain ($\varepsilon_{\mathrm{local}}$) and average strain ($\varepsilon_{\mathrm{avg}}$) definitions are used. The engineering strain was calculated by measuring the distance of two points on the gauge of a tensile specimen by optical DIC. The local strain, on the other hand, is the microscopic, phase-partitioned strain, captured by the µ-DIC. The average strain corresponds to the mean value of the local strain histogram at each stage of deformation, representing the average deformation level of the local microstructural area analyzed by the µ-DIC. Note that up to the onset of necking, the average strain can be assumed to be comparable to the engineering strain. The quantitative strain analyses performed in this study utilize two types of representative strains: (i) equivalent von Mises strain ($\varepsilon_{\mathrm{local,vM}}$ or $\varepsilon_{\mathrm{avg,vM}}$) and (ii) the strain component along the tensile axis ($\varepsilon_{\mathrm{local,xx}}$ or $\varepsilon_{\mathrm{avg,xx}}$).

Local strain maps and histograms (Figs. 5-4(b_1-b_3)) calculated from in-beam

SE images at each deformation step provided a qualitative indication of local strain partitioning. The most evident trend is the significant role of F in accommodating plastic strain in this alloy. More quantitative evaluation of this phase-dependent strain partitioning as a function of the average strain level is provided in Fig. 5-4(c). The strain-partitioning plot demonstrates that large amount of local strain is partitioned into F. More specifically, F tends to accommodate three times more strain ($\varepsilon_{\text{local,xx}} = 0.21$) than FM ($\varepsilon_{\text{local,xx}} = 0.07$) at $\varepsilon_{\text{avg,xx}}$ ~0.17. The B/TM group carries a medium amount of strain accounting for $\varepsilon_{\text{local,xx}}$ of 0.14 at the same strain level. Note that this strain-partitioning tendency between these phases, i.e., $\varepsilon_{\text{local,xx}}$: F > B/TM > FM, is somewhat expected from the nanohardness measurements, i.e., H_{nano}: F < B/TM < FM. An interesting observation is about the local strain evolution of RA relative to those of the other stable phases. Contrary to the near-linear development of the local strain observed in the three stable microstructural constituents (F, B/TM, and FM), the slope of the local strain of RA tends to decrease with deformation. The overall strain level of RA locates between those of F and FM, similar to the strain partitioned into B/TM. In analyzing Fig. 5-4(d), it should also be considered that RA data points were selected before deformation, and those points were tracked throughout the following stages of deformation. As a consequence, these data also include the behaviors of mechanically induced martensitic regions that have formed. This point will be discussed in more detail in Section 5.5.

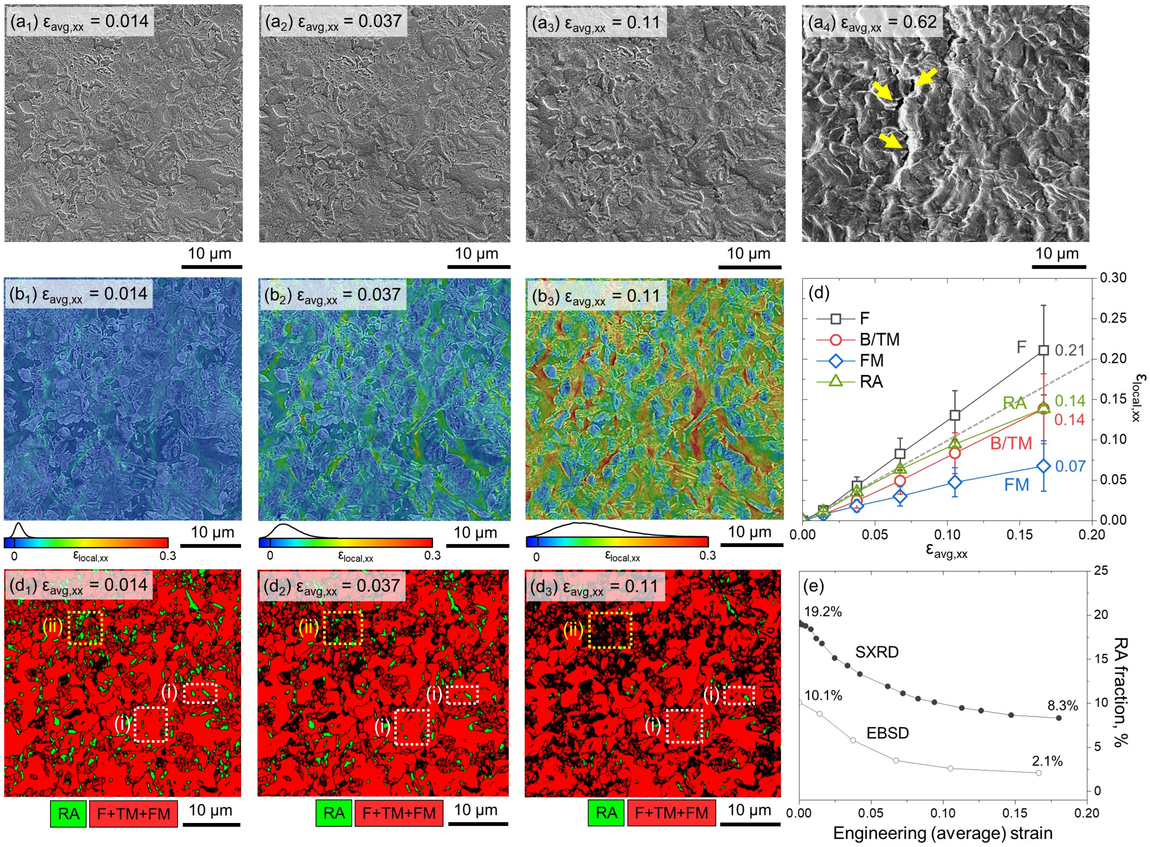

Figure 5-4: ***In situ* SEM/EBSD/SXRD characterization results.** (a) SE images, (b) *in situ* strain maps, and (c) phase maps at the average strain levels of (a_1-c_1) 0.014, (a_2-c_2) 0.037, and (a_3-c_3) 0.11. (a_4) SE micrograph at $\varepsilon_{avg,xx} = 0.62$ with the surface cracks highlighted by the arrows. (d) Local strain-partitioning plot. The dashed line corresponds to the equi-partition line. (e) Evolution of retained austenite fraction as a function of applied strain measured by *in situ* EBSD and SXRD experiments.

Retained austenite transformation

The evolution of the RA fraction as a function of applied strain was measured by *in situ* EBSD (in area fraction) and *in situ* SXRD (in volume fraction), as shown in Fig. 5-4(e). Regarding the initial fraction of RA, although the value obtained from EBSD indicates the presence of ~10% blocky RA, the SXRD results reveal that extra 9% of thin-film interlath RA exists in this alloy that is not captured by EBSD. The approximate fraction of the total RA is thus approximately 19%. However, as can be seen from the transformation kinetics measured by these two methods (Fig. 5-4(e)), approximately ~9% of thin-film RA is highly stable, barely transforming to martensite during deformation. For example, the amount of the RA stable at around uniform elongation ($\varepsilon_{\mathrm{eng}}\sim0.18$) is ~8% in the SXRD data and ~2% in the EBSD data, respectively. The difference between these values, ~6%, thus should be explained by the amount of stable thin-film interlath RA. This indicates that at best, 2-3% of the interlath film type RA may have transformed into martensite until uniform elongation. Although the limited field of view in the *in situ* EBSD measurements can be a potential source of error in this estimation, the comparable shapes of the two curves, i.e., similar slope decrease in the EBSD and SXRD data, also support that both curves mainly reflect the transformation kinetics of blocky RA. Furthermore, surface roughness that develops during *in situ* SEM deformation can underestimate the RA fraction, which requires further validation. To evaluate this surface effect, post-mortem EBSD measurements were performed on a different tensile sample deformed to $\varepsilon_{\mathrm{avg}}\sim0.2$. The results in Fig. 5-5 show that about 2.3% of RA is still stable, which is comparable to the RA fraction measured *in situ* (~2.1%).

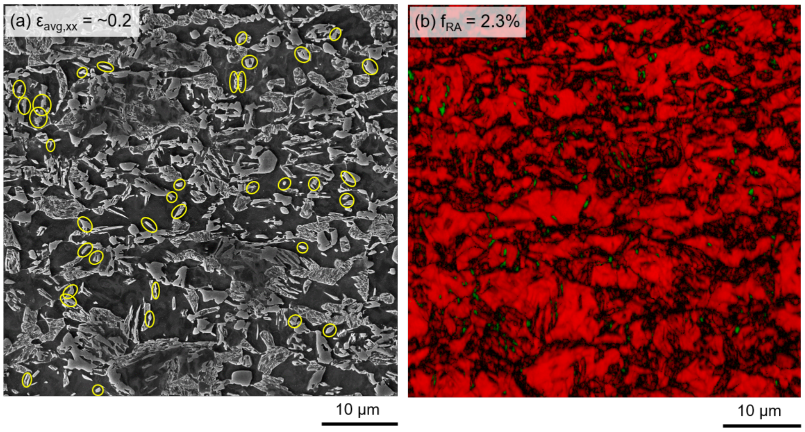

Figure 5-5: Post-mortem characterization of highly deformed microstructure. (a) SE images and (b) EBSD phase maps at $\varepsilon_{\mathrm{avg,xx}} = \sim0.2$ Note that the characterization was performed on an etched surface, and the lower CI points (CI < 0.05) were excluded from the phase fraction calculation. The phase fractions of remaining retained austenite at this deformation level corresponds to $f_{\mathrm{RA}} = 2.3\%$. The retained austenite in ferrite grains are highlighted by yellow circles in (a).

Furthermore, EBSD phase maps (Figs. 5-4(d_1-d_3)) can also provide information on neighborhood dependence of the mechanical stability of RA. This surrounding microstructure effect can be qualitatively examined by comparing the transformed area of RA at different locations. The RA grains in box (i), for instance, are fully enclosed by a F grain, stable up to the average strain level of 0.11. On the other hand, the other type of RA, the one embedded in a B/TM region, highlighted as box (ii), starts to transform at the early strain level, around 0.037 $\varepsilon_{\mathrm{avg,xx}}$, resulting in the loss of index at low strain levels.

A more quantitative evaluation of such neighborhood dependency on the transformation of RA was carried out with the *in situ* EBSD phase maps (Figs. 5-4(d_1-d_3)) by tracking the changes in the area fractions of RA in different neighborhoods. Following the classification of the retained austenite based on its neighborhood microstructure as described in Section 5.2, three types of RA were evaluated: (i) RA embedded in F (referred to as RA in F), (ii) RA surrounded by B/TM (referred to as RA in B/TM), and (iii) RA next to FM (referred to as RA next to FM). In total, 30, 42, and 19 RA grains were selected to represent each category, (i), (ii), and (iii), respectively. Note that the number of grains included in (iii) was smaller than (i) and (ii) types due to the small fraction of FM. The average grain sizes of RA show some variations depending on its neighbor, corresponding to 0.658 ± 0.159 µm for (i), 0.525 ± 0.111 µm for (ii), and 0.483 ± 0.086 µm for (iii). In this quantitative analysis, the areas of the RA grains of each type were summed and normalized to the total area of the RA measured before the deformation. As RA transforms to martensite, the number of RA indices decreases, leading to a gradual reduction in its area. It should be noted that this analysis assumes that the loss of RA indices in EBSD is mainly caused by MIMT, disregarding the possible loss of index due to plasticity of RA.

The results presented in Fig. 5-6 demonstrate a clear neighborhood dependency on the stability of RA, showing that RA grains embedded in the middle of F grains tend to transform less at the same strain level compared to others. Note that this stability difference becomes noticeable from $\varepsilon_{\mathrm{avg,xx}}\sim 0.03$, while negligible in the early plastic regime ($\varepsilon_{\mathrm{avg,xx}}\sim 0.01$). The fractions of the remaining RA are 20 % higher in RA in F than in RA in B/TM in most of the average strain levels from 0.037 to 0.11. The distinction between RA in B/TM and RA next to FM is unclear, in general, partially due to the limited sample size of RA next to FM. Furthermore, it should be noted that this observation was made on the surface, which requires further validation of the bulk microstructure. EBSD characterization results of the deformed tensile specimen performed after polishing and etching (Fig. 5-5) also exhibit the consistent outcome, showing a higher amount of RA within F grains even at $\varepsilon_{avg,xx}$ = ~0.2.

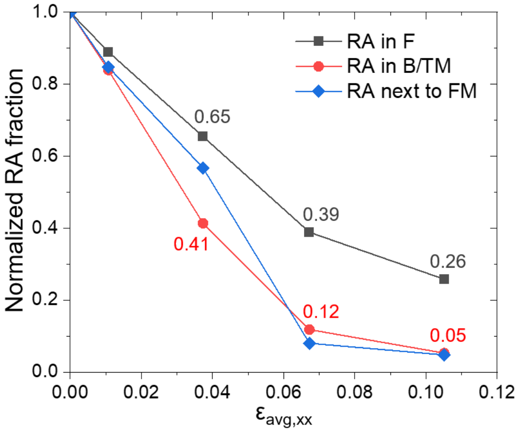

Figure 5-6: Neighborhood-dependent retained austenite fraction evolution as a function of the average strain. Note that in each curve, the phase fraction is normalized by the area of the retained austenite grains measured at an undeformed state.

Surface cracking

Upon further straining approaching fracture, surface cracks start to form along phase interfaces. Figs. 5-4(a_1-a_3) display the surface topology development during the deformation, and the last image, Fig. 5-4(a_4), captured at the heavily deformed state ($\varepsilon_{avg,xx}$ = 0.62), exhibits that the surface roughness that develops upon straining can lead up surface cracking as highlighted by the arrows. The more detailed characterization of these cracks is provided in Fig. 5-7. Fig. 5-7(a) shows the BSE image of the initial microstructure, and the post-deformation state of the equivalent area is shown in Fig. 5-7(b). Due to significant surface topology development, cracks were identified in the in-beam SE images, where such roughness effects can be minimized due to the detector being aligned parallel to the electron gun [36]. By coupling the phase identification analysis shown in Figs. 5-1 (d-g), it is clearly observed that most surface cracking incidents occur at the phase interfaces where FM is involved, although the fraction of FM is limited (~5.5% as shown in Fig. 5-1(f)). In this local area, the most frequently observed type of surface crack is the cracking at the interface between F and FM which correspond to the softest and the hardest phases in the microstructure, respectively. In the 50×50 µm^2 area subjected to the *in situ* SEM/EBSD characterization, in total 30 surface cracks were observed. The detailed statistical results of these surface cracks will be provided in Section 5.6 and discussed in the context of strain localization.

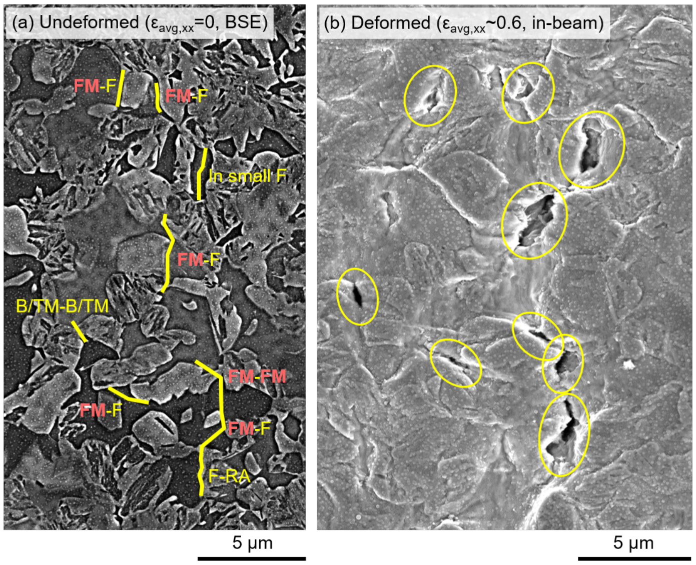

Figure 5-7: Surface cracks. (a) BSE image of the initial microstructure. (b) In-beam image of the same area as (a) after 60% of tensile deformation

Summary of the *in situ* observations

The comprehensive characterizations performed through the *in situ* SEM/EBSD characterization and *in situ* SXRD tensile testing provide the following indications. First, as expected from the nanohardness measurements, i.e., H_{nano}: F < B/TM < FM, the local strain partitioning among different stable microstructural components is highly phase-dependent, exhibiting i.e., $\varepsilon_{local,xx}$: F > B/TM > FM. The mean local strain of RA is slightly higher than that of B/TM in most of the deformation stages, but the difference becomes smaller as the overall strain level increases. Furthermore, in general, thin-film interlath RA is stable throughout the deformation, implicating that it is mostly blocky RA that transforms to martensite during the deformation. This implies that the TRIP effects of this alloy primarily arise from MIMT of blocky RA, and thus understanding the governing factors for the transformation of blocky RA is of crucial importance in better designing strain hardenability. A controlling factor observed in the study is the neighborhood microstructure: the RA embedded in the F grains is apt to transform less at the same strain level (or to transform slowly upon deformation). In the following sections, we will investigate the microstructural origin of these experimental results from the following perspectives: (i) composition and orientation (Section 5.4) and (ii) neighborhood microstructure (Section 5.5). A higher probability of surface cracking at the phase interfaces associated with fresh martensite will be explained by strain localization and damage micro-mechanisms with detailed statistical examinations (Section 5.6). Lastly, based on all discussions, microstructure design strategies to better utilize mechanically induced martensitic transformation will be proposed (Section 5.7).

5.4 Composition and orientation effects

It has generally been accepted that RA embedded in F has less C than RA surrounded by B/TM [228–230]. This is because if RA is enclosed by the C-depleted F phase, less amount of C diffuses into RA during partitioning heat treatments than into the RA surrounded by the C-rich B/TM matrix. Quantitative investigations by atom probe tomography (APT) in a similarly processed QP steel also revealed that $\sim$0.3 wt% less C is partitioned into RA in F than RA in B/TM [230]. Therefore, the high stability of RA in F observed in this study (Fig. 5-6) is somewhat unexpected from a composition perspective. We also measured the average Mn concentration in RA at different locations by EDS. The result summarized in Table 5.4 shows a slightly lower amount of Mn in RA in F, about 0.2 wt% less than that of RA in B/TM, similar to the previous APT [230] and TEM-EDS [231] measurements. Line profiles for Mn distributions across different phases are provided in Fig. 5-8. The lower Mn content of RA in F, in addition to the expected smaller C content, predicts that RA in F is unstable compared to RA in B/TM, which is opposite to our observation (Fig. 5-6). This again indicates that the compositional effects alone cannot explain the high stability of RA in F.

Table 5.4: Average Mn concentration at different locations.

Location	F	B/TM	RA in F	RA in B/TM
Mn wt%	1.67 ± 0.16	2.49 ± 0.13	2.44 ± 0.30	2.65 ± 0.29

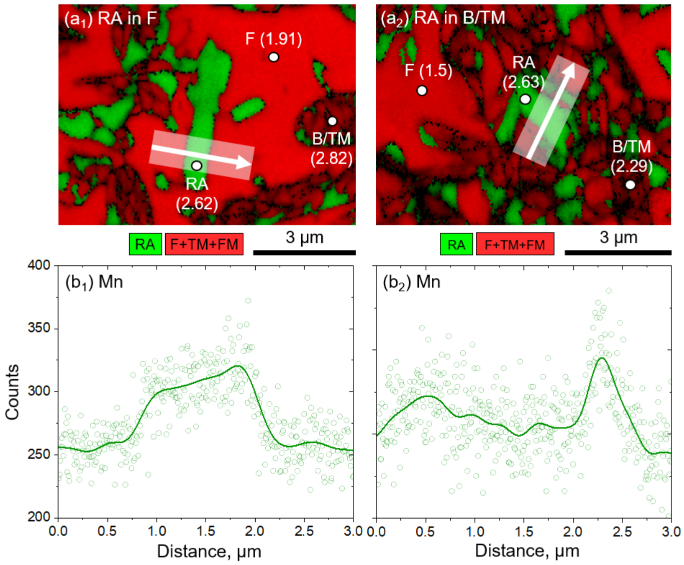

Figure 5-8: Mn enrichment in retained austenite. EBSD phase maps showing (a_1) RA embedded in F and (a_1) RA surrounded by B/TM. The Mn contents (in wt%) measured at different points (labeled as '∘') are shown in each phase map. Mn distribution (1 μm line width) along the arrows in (a_1-a_2) obtained from EDS line scans are shown in (b_1-b_2), respectively.

The crystal plasticity effects arising from the crystallographic orientation of RA also need to be considered to understand the presented observations. Many experimental and modeling studies have shown that RA grains with the {200} planes aligned near-parallel (∼0°) or near-perpendicular (∼90°) to a loading direction easily transform due to high resolved shear stress, resulting in the standard deformation texture of the {111} component parallel to the tensile axis [42, 202, 203, 232]. In fact, the overall texture evolution exported from the *in situ* EBSD and SXRD data in this study also shows that this trend holds (Fig. 5-9).

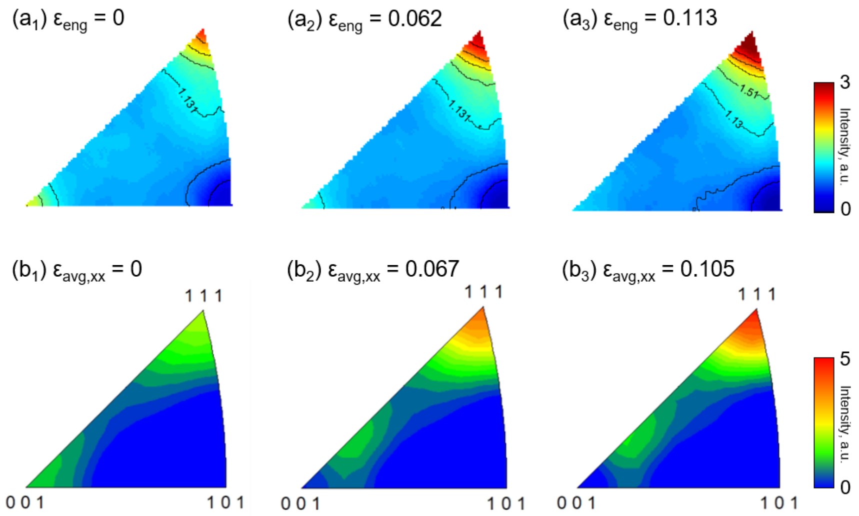

Figure 5-9: Texture evolution of retained austenite. Inverse pole figures (IPFs) of retained austenite at different strain levels, measured by (a) *in situ* SXRD and (b) *in situ* SEM/EBSD tensile deformation.

However, our detailed crystallographic analyses of RA at different locations indicate that the orientation of RA cannot fully explain the higher mechanical stability of RA in F. In other words, in this microstructure, the orientation of RA is not neighborhood-dependent. This point can be validated by Schmid factor (SF) analyses of FCC $\{111\} < 1\bar{1}0 >$ slip systems. For example, one can qualitatively acknowledge the negligible difference in initial texture between RA in F and RA in B/TM from the SF map of RA in Fig. 5-10(a). A more quantitative evaluation was performed by calculating the maximum SF among all FCC $\{111\} < 1\bar{1}0 >$ slip systems, as shown in Fig. 5-10(b). The grain number cumulative distribution functions (CDFs) of Schmid factors demonstrate that there is no statistically significant difference in the maximum SFs between these RA grains. For example, the number fraction of RA grains whose SFs are equal to or greater than 0.45 is approximately 0.5 for both RA in F and RA in B/TM. Moreover, even between the RA grains in F, there is no clear orientation dependence on the transformation (Fig. 5-10(c)). This point leads us next to consider the micromechanical boundary conditions arising from the neighborhood microstructure.

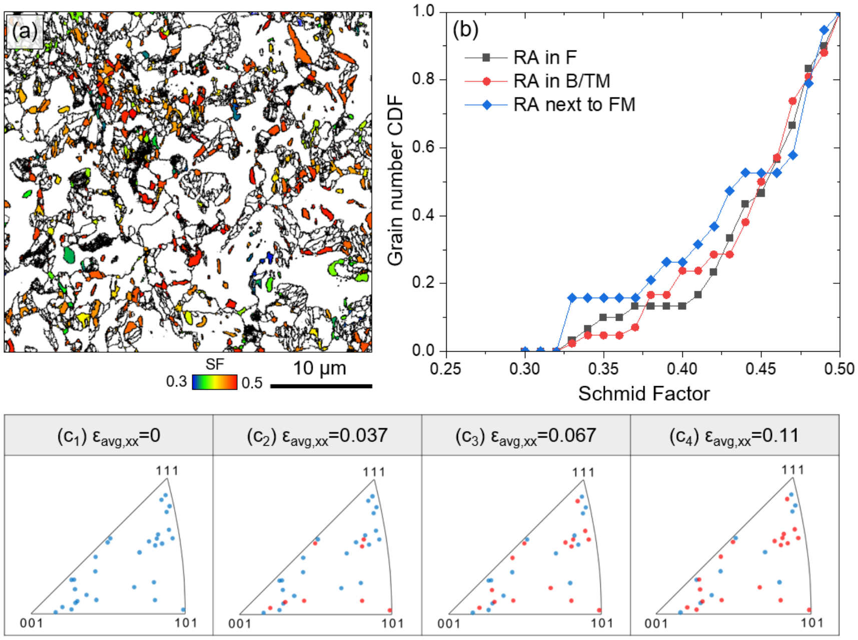

Figure 5-10: Orientation of retained austenite grains. (a) FCC Schmid factor map of retained austenite in the microstructural area where the *in situ* characterization was performed. The map was obtained from the OIM software (b) Grain number cumulative distribution functions (CDFs) of Schmid factors of retained austenite grains at different locations, i.e., RA in F, RA in B/TM, and RA next to FM. Only maximum Schmid factor of $\{111\} < 1\bar{1}0 >$ slip systems of a grain is employed to construct the CDF plots. (c) IPFs of RA in F included in the statistical analysis in Fig. 5-6. The blue dots in (c$_1$) shows the initial orientation of the RA grains in F. The RA grains transformed more than 80% of their grain areas are labeled as red dots.

5.5 Neighborhood effects

Heterogeneous deformation is a common phenomenon in polycrystals under load [31, 84, 233, 234]. Presence of phases with distinct mechanical characteristics can intensify such strain heterogeneity, and as a result, a considerably different amount of local strain is partitioned into different phases as studied in these references [33, 235–237]. Such phase dependency on strain partitioning is also observed in our work, i.e., $\varepsilon_{\text{local,xx}}$: F > B/TM > FM shown in Fig. 5-4(d), demonstrating that the micromechanical effects are active in this QP steel. Furthermore, for F, the softest phase, a more severe strain heterogeneity develops within a grain, as shown in Fig. 5-4(b).

To explore the effects of these phase-dependent strain partitioning and intragranular strain heterogeneity of F on pre- and post-transformation behaviors of RA, local strain profiles of RA at different locations were exported. The following four RA grains were subjected to the analysis: (i) untransformed RA in F, (ii) transformed RA in F, (iii) transformed RA in B/TM, and (iv) transformed RA next to FM. Note that terminology, 'transformed RA' represents the RA that is confirmed to be transformed to martensite up to $\varepsilon_{\mathrm{avg,xx}} = 0.11$. Thus, the strain profiles contain all strain contributions that RA can provide, such as plasticity of RA, phase transformation strain, and deformation of mechanically induced martensite (onward referred to as 'MM').

The strain profiles in Figs. 5-11(b_1-b_2) demonstrate that there is a clear difference between the local strain evolution of the untransformed and transformed RA grains even though the two RA grains are placed in the same F grain. Limited strain is partitioned into the untransformed RA (Fig. 5-11(b_1)), for instance, and this leads to significant strain heterogeneity that develops between the untransformed RA and the neighboring F. On the other hand, the transformed RA (Fig. 5-11(b_2)) plastically deforms together with the surrounding F, contributing to homogeneous strain distribution up to $\varepsilon_{\mathrm{avg,xx}} = 0.11$. However, in a later stage of deformation, e.g., $\varepsilon_{\mathrm{avg,xx}} = 0.17$ (close to the onset of necking), the strain that the transformed RA in F accommodates starts to decrease, resulting in the stepwise strain profile (Fig. 5-11(b_2)). For RA in B/TM (Fig. 5-11(b_3)), a relatively horizontal strain distribution develops, indicating that the transformation results in homogeneous deformation in this region until $\varepsilon_{\mathrm{avg,xx}} = 0.11$, similar to the case of the transformed RA in F (Fig. 5-11(b_2)). However, the local strain of MM in B/TM starts to increase at $\varepsilon_{\mathrm{avg,xx}} = 0.17$, as shown in Fig. 5-11($b_3$). The local strain of the last case, transformed RA next to FM, develops gradually with increasing strain level (Fig. 5-11(b_4)). Unlike the substantial strain incompatibility that occurs between F and FM, as indicated by the sharp strain gradient between these two phases, smooth strain gradient is observed between FM and RA.

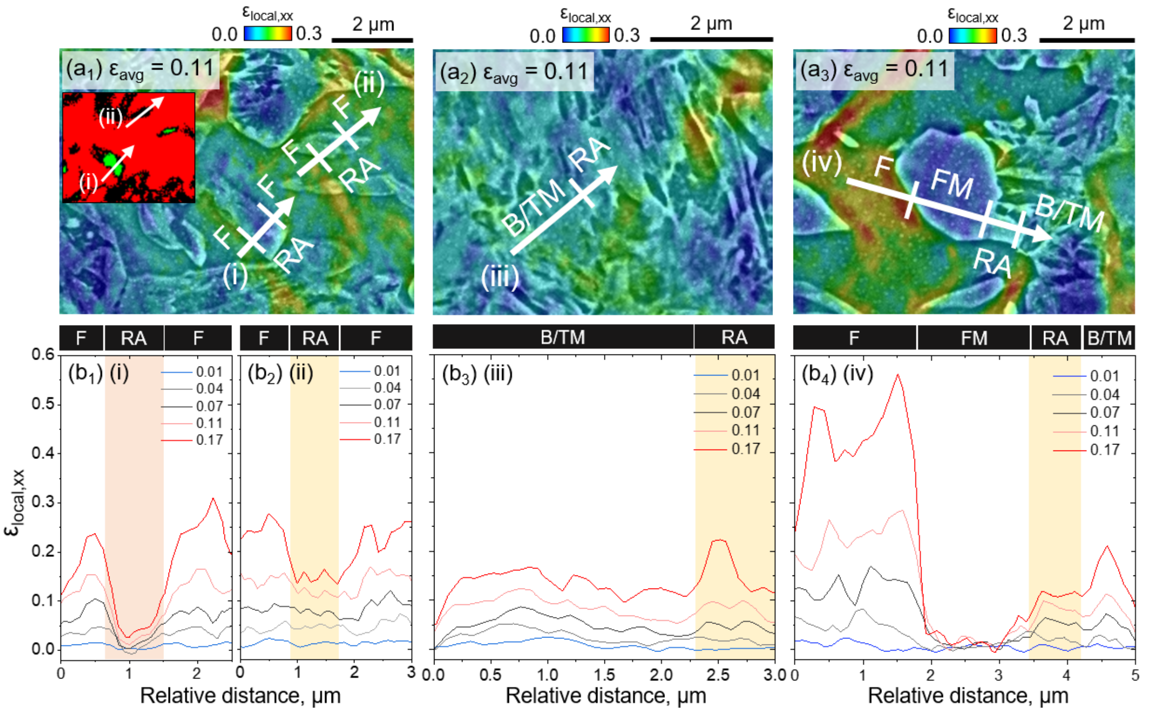

Figure 5-11: Local strain profiles across retained austenite grains and its surroundings. Local strain maps of retained austenite (RA) (a_1) enclosed by ferrite (F), (a_2) embedded in bainite and tempered martensite (B/TM) regions, and (a_3) next to fresh martensite (FM) at $\varepsilon_{avg,xx} = 0.11$. Local strain profiles along the arrows drawn across (b_1) untransformed RA in F (line (i) in (a_1)), (b_2) transformed RA in F (line (ii) in (a_1)), (b_3) transformed RA in B/TM (line (iii) in (a_2)), and (b_4) transformed RA neighboring FM in (line (iv) in (a_3)). The inset in (a_1) corresponds to the EBSD phase map recorded at $\varepsilon_{avg,xx} = 0.11$, showing (i) untransformed and (ii) transformed RA grains.

This local strain evaluation (Fig. 5-11) indicates that in addition to the mechanical stability of RA, the local strain partitioned into the transformed product, that is, mechanically induced martensite, is also neighborhood dependent. This argument is further statistically validated by examining the average local strain evolution of RA at different locations, as presented in Fig. 5-12. Schematic in Fig. 5-12(a) explains how the mean local strain values of RA and mechanically induced martensite (MM) at different locations were exported from RA grains that gradually transform to martensite. Starting from three grains of RA (γ_A, γ_B, and γ_C) in an undeformed state (ε_0), for instance, only the transformed area of RA is considered, since it represents the cumulative amount of strain of RA arising from deformation of RA and MM after it transforms (red line labeled as 'RA-MM' in Fig. 5-4(a)). On the other hand, the strain partitioned into RA that never transforms to martensite belongs to the other category (green line labeled as 'RA'). This local strain exportation methodology was applied to all RA grains included in the calculation of the RA fraction (Fig. 5-6). A representative local strain value of an RA grain was obtained by averaging the five local strain data points per grain. The mean local strain values were calculated from the local strain values of the RA grains, and the error bars here correspond to the standard error of the mean. The calculated local strain evolution of RA is plotted together with those of its neighboring microstructural constituents in Figs. 5-12(b_1-b_3).

For RA in F, as similarly observed from Fig. 5-11(b_1), the total strain of the untransformed RA remains low (RA in Fig. 5-12(b_1)). This low strain imposed on RA may inhibit its transformation. For the transformed RA in F (RA-MM in Fig. 5-12(b_1)), several interesting phenomena are observed. First, its overall strain is lower than that of F, which can be explained by the high strength of RA compared to that of F (Fig. 5-3). Second, it accommodates a much higher amount of strain than the untransformed RA, partially due to additional plasticity arising from the TRIP effects. Third, the slope of the total strain of transformed RA in F (RA-MM) gradually decreases, leading to the increasing discrepancy between the partitioned strain of F and MM. To fully understand the second and third points, the contribution of MM was separated from the total strain of RA. The blue curve, MM, in Fig. 5-12(b_1), represents the evolution of the MM observed at $\varepsilon_{avg,xx} = 0.037$. Although the first data point of the blue curve includes all kinds of strain contributors, such as dislocation plasticity of RA, transformation strain, and deformation of MM, it can be safely assumed that the evolution of the curve from the first point onwards reflects the deformation of MM only. It is clearly seen that the local strain evolution curve of MM almost overlaps with that of RA-MM. This is somewhat surprising, which should be understood together with the transformation rate (Fig. 5-6). At $\varepsilon_{avg,xx} = 0.067$ (the second point of the blue curve), the majority of RA in F (more than 60%) already transformed to martensite. This means that at low strains, the accumulated RA-MM curve is close to the behavior of plasticity deforming RA, and at high strains, the same curve mostly represents that of MM. As more RA transforms, the strain partitioning occurs between soft F and hard MM, resulting in a gradual reduction in the slope of the total local strain (RA-MM). This point can lead to further deduction about the behavior of transforming RA. Fully resolving the local strain of transforming RA, i.e., the RA soon to be transformed to MM as the strain level increases, is difficult, but considering the slope decrease caused by MM, the local strain of transforming RA can be higher than the RA-MM curve.

In contrast to RA in F (Fig. 5-12(b_1)), the local strain evolution of RA in B/TM (Fig. 5-12(b_2)) does not exhibit such a continuous slope decrease. Rather, the local strain values of RA-MM and MM in B/TM increase linearly with the applied strain. The strain values of RA-MM and MM are comparable in this case, which can be described similarly to those of RA in F, by the high transformation rate in the early stages of deformation. Another intriguing point in RA in B/TM is that the local strain evolution curves of RA-MM, MM, and TM have similar slopes, meaning that the local strain values of RA-MM and MM tend to increase together with that of B/TM. On the other hand, in the case of RA next to FM (Fig. 5-12(b_3)), the discrepancy between RA-MM and FM increases further with more deformation. These observed differences in the accumulated behaviors of RA between RA in B/TM and RA next to FM can be explained by the substantial hardness difference between B/TM and FM with respect to RA (Fig. 5-3). The similarity in the mechanical strength of RA and B/TM leads to a relatively homogeneous deformation between these phases, while the presence of the hardest FM next RA forces RA to an increase in the degree of strain heterogeneity.

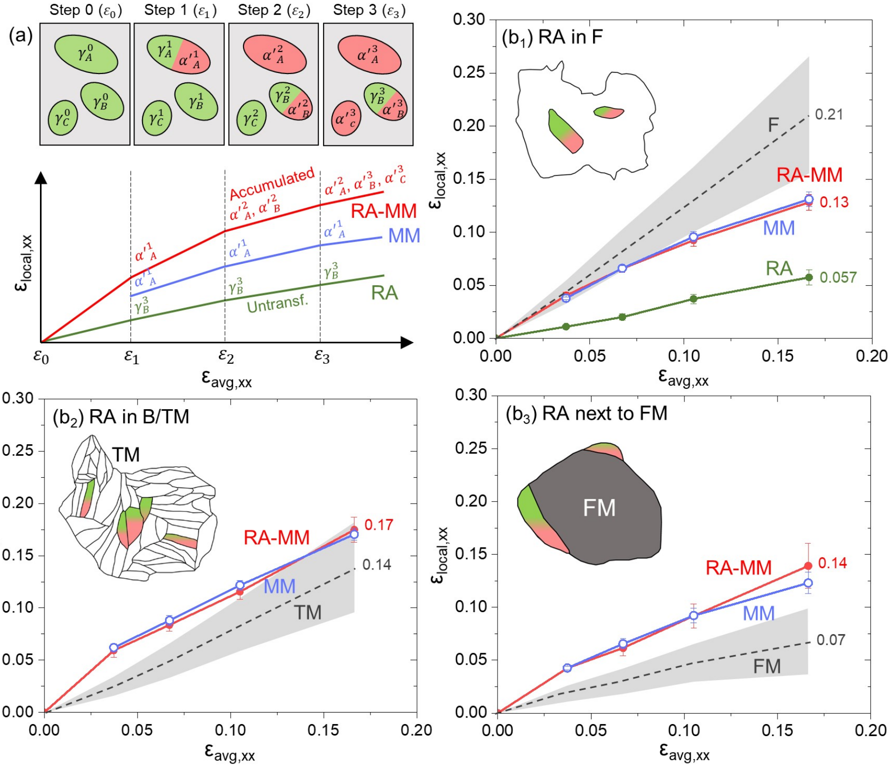

Figure 5-12: Neighborhood dependency of local strain evolution of retained austenite and transformed martensite. (a) Schematic representation of exporting the mean local strain of transforming retained austenite and transformed martensite (RA-MM) and untransformed retained austenite (RA). Local strain evolution of (b$_1$) retained austenite enclosed by ferrite (RA in F), (b$_2$) retained austenite surrounded by bainite and tempered martensite matrix (RA in B/TM) and (b$_3$) retained austenite next to fresh martensite (RA next to FM).

With regard to the effects of the neighborhood microstructure on the mechanical stability of RA, the governance of individual factors or their combinations is still a matter of controversy. Some studies claimed that in addition to the higher C content [198–200], hydrostatic pressure and stress shielding imposed by surrounding bainitic or martensitic matrices can further increase the stability of interlath RA [238,239]. On the contrary, Tomota *et al.* [240] proposed that blocky RA in F can be more stable due to stress relaxation of F, also similarly observed by Tirumalasetty et al. [232] One of the evident reasons for these inconsistencies in the literature is different compositions and thermomechanical histories, leading to a wide spectrum of mechanical properties of existing phases. Variation in temperature and time for partitioning or tempering heat treatments can result in significantly different relative strengths of RA, B, TM, and FM, and thus the stability of RA. In our work, RA and B/TM exhibit similar nanohardness (or slightly lower in RA), and under this condition, no significant stress shielding from B/TM is applied to RA, and thus the transformation of RA in B/TM is facilitated. In this case, a homogeneous strain distribution can develop, as similarly observed by Wang *et al.* [218] Even after the transformation, MM can continue to deform and accommodate a large amount of strain, exhibiting little contribution to the initiation of cracks between RA and B/TM.

5.6 Strain localization and damage micro-mechanisms

Despite the dependency of local strain of RA on its surrounding microstructure (Fig. 5-12), on average, RA exhibits good deformability, whose mean strain is close to the average strain imposed on the microstructure (Fig. 5-4(d)). It was initially expected that RA can contribute to final failure as it transforms to hard martensite. However, our qualitative observations of the surface cracks in Fig. 5-7 rather implicate the presence of chunky FM islands, which are thermally induced, as a precursor to damage, suggesting little impact from RA or MM. To validate this point more statistically, we further classified 30 surface cracking events that were identified in the area of our interest (Fig. 5-1) in detail. These cracking incidents were grouped into the following four categories: cracking (i) in the middle of a F grain, (ii) in a F grain next to a hard phase (X), (iii) in a F grain between two hard phases (X_1 and X_2), and (iv) between two hard phases (X_1 and X_2) without the presence of F. The result in Fig. 5-13 demonstrates that despite the limited fraction of FM (less than 6%), its contribution to cracking is substantial, involved in almost two thirds of cracking incidents. Note that the effects of MM are indirectly included in the statistics of RA. RA or MM is less likely to crack, unless it is located next to FM.

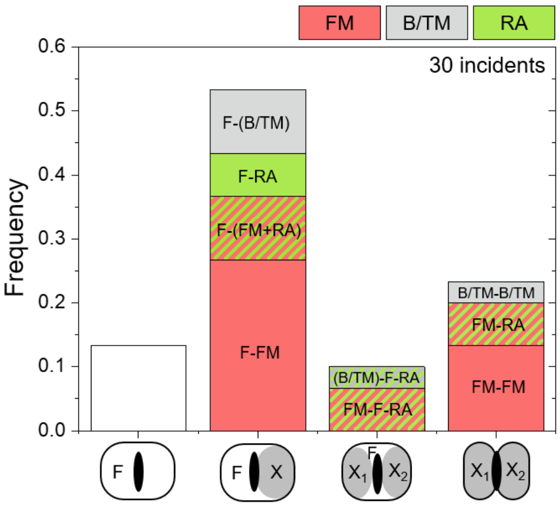

Figure 5-13: Statistics of the neighborhood dependency on surface cracking. The hard phases are colored as red (FM: fresh martensite), grey (B/TM: bainite and tempered martensite), and green (RA: retained austenite). The cracking events where two hard phases are involved are highlighted by multiple colors representing each phase.

Given that microscopic strain localization sites are regarded as likely microstructural features where damage initiates [93,94], the in-depth analyses of such sites (referred to as strain localization incidents onwards) can provide meaningful information on detrimental microstructural configurations. From the *in situ* strain maps, strain localization incidents are defined as the top 4% most strained subset [16], which corresponds to $\varepsilon_{\mathrm{avg,vM}} \geq 0.43$ at $\varepsilon_{\mathrm{avg,xx}} = 0.17$. Figs. 5-14(a-b) show the isolated strain localization incidents as a result of this criterion. The determined strain localization incidents are displayed on top of the deformed BSE image (Fig. 5-14(a)) and pre-deformed EBSD phase map (Fig. 5-14(b)) to better visualize their locations. Qualitative observation of Figs. 5-14(a-b) indicates that most strain localization incidents are found inside soft F grains adjacent to hard phases such as FM, B, or TM.

These strain localization incidents were subjected to detailed classification based on their configuration with respect to the surrounding microstructure. To better connect microscopic strain localization and surface crack formation, the criteria used for classifying the cracks (Fig. 5-13) were also adopted in strain localization incidents as shown in Fig. 5-14(c). The type (i) incidents are the strain localization events that occur in the middle of F grains, whereas types (ii) and (iii) are the ones in F but either (ii) next to or (iii) between hard phases. The last type, (iv), is the strain localization observed at the phase boundaries shared by hard phases other than F. Among these four types, type (ii) and (iii) exhibit the highest mean local strain values as shown in Fig. 5-14(d), implying the critical role of these two microstructural configurations in local strain development. Furthermore, among all possible neighbors that can constitute hard phases in types (ii) and (iii), the presence of FM turns out to be the most critical than the other phases. Figs. 5-14(e-f), for instance, show the mean local strain values of the strain localization incidents depending on the types of hard phase such as F, B/TM, and RA. These plots show that among the top 4% most strained subset, the strain localization incidents where FM is involved reveal the highest local strain values. On the other hand, RA which later transforms to MM does not seem to be a critical factor in promoting local strain than other hard phases. In other words, whether RA can be detrimental or not is also neighborhood-dependent. For example, RA in B/TM is considered a safe configuration, since it causes no cracking. This can also be explained by the homogeneous strain distribution due to the comparable mechanical strength of RA and B/TM. The interfaces between RA and F can show some cracking as well in specific cases, but the frequency of such cracks is limited (6.7%). Most cracks where RA is involved are correlated with the presence of FM near or next to RA (23%). Note that such a limited impact of RA on final failure was also reported by Salehiyan et al. [217]

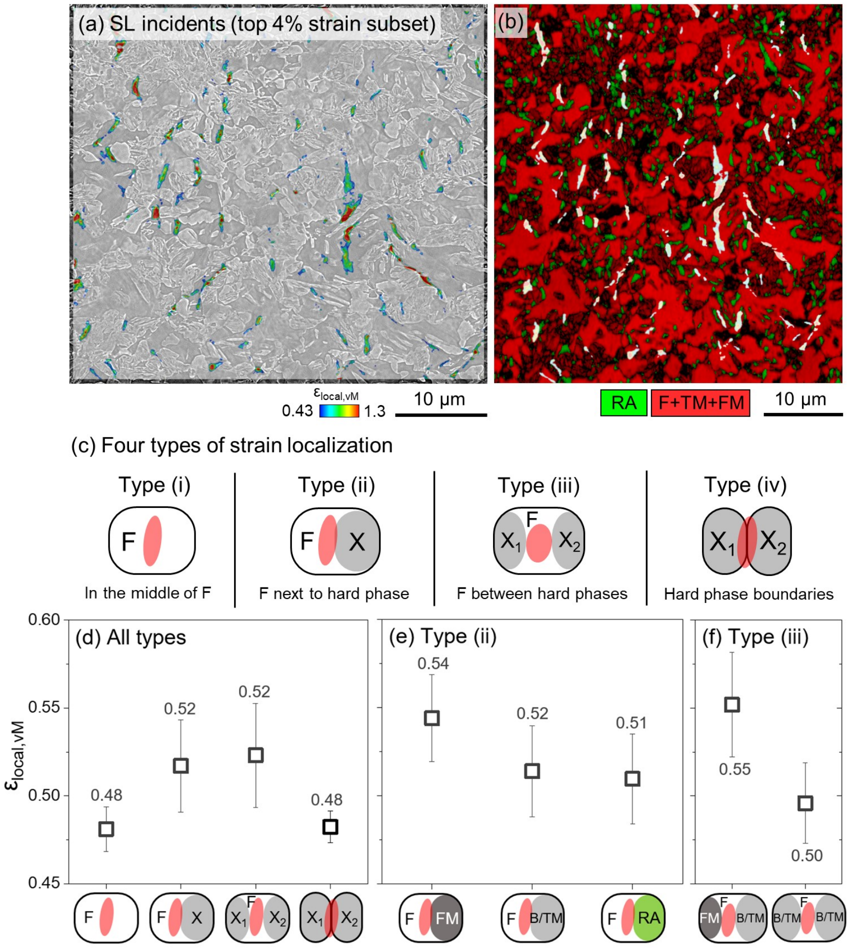

Figure 5-14: Classification of strain localization incidents based on the neighborhood microstructure. Identified strain localization incidents (top 4% most strained subset, i.e., $\varepsilon_{\mathrm{local,vM}} \geq 0.43$) overlaid on (a) BSE image ($\varepsilon_{\mathrm{avg,xx}} = 0.17$) and (b) pre-deformation EBSD phase map. (c) Classification of the strain localization incidents into four types: strain localization (i) in the middle of ferrite grain, (ii) in the ferrite next to hard phase, (iii) in the ferrite between two hard phases, and (iv) between hard phase boundaries. (c) Mean local strain values of four types of strain localization. Mean local strain values of (d) type (ii) and type (iii) strain localization incidents depending on neighboring microstructural constituents.

5.7 Micromechanically guided microstructure design

Based on the micromechanical understandings that are developed in this study, as a last discussion point, we aim to propose several microstructure strategies to better optimize strength-ductility combinations for this type of ferrite-containing QP steels. First, in addition to the amount of C transferred from C-rich martensite to RA, partitioning or tempering heat treatments should be executed with extra consideration of the desired relative strengths (or yield strength) of RA and B/TM. If the strength of RA is comparable to that of surrounding B/TM, RA can easily transform, substantially contributing to strain hardening, especially in the early stages of deformation. If the B/TM matrix is too strong, on the other hand, RA can be highly stable throughout the deformation [193]. Controlling the defect density in B or TM can be a primary focus. In the work of He et al. [241], it was observed that a decrease in the dislocation density of a bainitic matrix can enhance the transformation of RA in a low C bainitic steel, seemingly due to released compressive stress field of the bainitic matrix and increased stress onto RA. More delicate control of composition is also desired, as in addition to the average C content, the amount of alloying additives such as Si, Al, Mn, Mo, and Cr can have an impact on the partitioning of C, partial transformation of RA to B, and also the tempering level of martensite [242–246]. All of these can affect individual phase strength and thus strain and stress partitioning.

Controlling initial yield strength and strain hardening behavior of F by solid solution strengthening can be another strategy that can be employed. Note that the contribution of RA in F to strain hardenability and ductility is somewhat different from that of RA in B/TM. Even though the strain partitioned into RA in F over the deformation is smaller than that of RA in B/TM, its relatively slow transformation rate has some potential to be utilized to sustain the TRIP effects at later stages of deformation. In the modeling work done by Tjahjanto *et al.* [247], a higher strain hardening of a ferritic matrix increases the stability of RA as F carries higher load and thus less stress is partitioned to RA. Adjusting the amount of Si in F can be an available processing approach to control the solid solution strengthening of the ferritic matrix, as experimentally validated by Jacques et al. [248]. Our observation further reveals the influence of the heterogeneous intragranular plastic flow inside F on the stability of RA. We expect that this can be more significant as F size increase, but it should also be noted that this intragranular strain distribution can also be influenced by the presence of RA grains. Modeling studies can be effective on this matter, allowing one to determine how the aspect ratio, size, and fraction of RA in F affect the strain distribution inside F. In addition, even with the same amount of blocky RA, depending on its distribution, specifically, the relative fractions of RA in F and B/TM, will cause significant difference in strain hardening behavior. Finding an optimal distribution of RA calls for further investigation.

Lastly, our strain localization and surface crack analyses (Figs. 5-13-5-14) make a clear point about the detrimental impacts of FM on promoting strain incompatibility. Despite its limited fraction in the microstructure, FM plays a critical role in cracking at the interfaces with F. Therefore, one of the key strategies to improve ductility as well as formability of this alloy is to reduce both the fraction and size of FM. Given that FM forms during final quenching, an appropriately positioned and applied controlled induction treatment may assist in tempering any FM that forms in the final cooling segment of a heat treat line. Several strain localization and damage micro-mechanism studies performed in a dual-phase steel [16,33,34,249] can also be extended to this alloy to some extent. For instance, given the fixed amount of F (e.g., 40-50% as recommended to maintain ductility and formability), refining F grain size can facilitate ductile fracture mechanisms [15,250].

5.8 Conclusion

In this work, we explored neighborhood microstructure effects on the mechanical stability of retained austenite and deformation behaviors of mechanically induced martensite (MM). The study was performed on a ferrite-containing QP steel consisting of ferrite (F), bainite (B), tempered martensite (TM), fresh martensite (FM), and retained austenite (RA). The local strain partitioned to these microstructural constituents were tracked throughout the deformation by *in situ* strain mapping techniques. The main results and conclusions are as follows.

(1) The local strain analyses show that the amount of strain partitioned into each phase are $\varepsilon_{\mathrm{local,xx}}$: F $>$ RA $\simeq$ B/TM $>$ FM. The total amount of strain that RA accommodates is slightly higher than that of B/TM but unlikely to other stable phase, the slope of the local strain evolution curve of RA gradually decreases with deformation.

(2) The *in situ* SEM/EBSD characterizations demonstrates that the onset of mechanically induced martensitic transformation depends on the neighboring microstructure of RA. RA surrounded by B/TM transforms faster than RA embedded in F at the same strain level. In most strain levels from 0.037 to 0.11, The area fraction of the remaining RA is 20% greater in RA in F than in RA in B/TM. This facilitated transformation of RA in B/TM can be explained by similar mechanical strengths of RA and B/TM, as measured by nanoindentation.

(3) The local strain partitioned into mechanically induced martensite and thus the total strain accommodated by RA is also neighborhood-dependent. RA in B/TM carried the highest amount of strain than RA in F and RA next to FM. Homogeneous distribution can develop in RA-B/TM mixtures. On the other hand, for RA in F, the amount of local strain that MM can accommodates gradually reduces with increasing deformation.

(4) Despite the finite fraction of fresh martensite ($< 6\%$), its contribution to final failure is predicted to be critical. Among 30 surface cracks, more than 60% of surface cracks are associated with the presence of fresh martensite. Little correlation between RA and surface damage was found, showing very limited number of cracks at RA and F interfaces.

Chapter 6

Conclusions and outlook

6.1 Thesis summary and conclusions

To expand our understanding of strain localization and damage micro-mechanisms in multi-phase alloys, this thesis presents the understanding of the three important microstructural effects in metals, e.g., local texture (Chapter 3), mechanical twinning (Chapter 4), and mechanically-induced phase transformation (Chapter 5). A comprehensive correlative approach was adopted to investigate the micromechanical response of phases, using the high-resolution *in situ* microstructure-based strain mapping technique and *in situ* synchrotron X-ray diffraction. Through this extensive screening of microstructure development during deformation, the contributions of individual phases, their plasticity mechanisms, and microstructural neighborhoods to strain heterogeneity were statistically and quantitatively evaluated. We envision that the correlations established in this thesis, between phase properties, partitioned local strain or stress, and macroscopically applied strain, can not only expand our scientific understandings but also propose desirable microstructural configurations to enhance the damage resistance of multi-phase alloys. The main findings of this thesis are summarized as follows:

In Chapter 3:

- The local crystallographic orientation of the α crystals plays a critical role in the activation of two characteristic strain localization mechanisms in a two-phase titanium alloy: (i) intragranular strain band in soft grains (multi-grain strain localization) and (ii) intergranular strain localization along boundaries (boundary strain localization).

- The multi-grain strain localization results from the local co-alignment of primary HCP slip systems. In this study, the alignment of pyramidal I <a> and prismatic <a> having high Schmid factors is found to be responsible for the formation of intragranular strain localization across neighboring α grains.

- Intensive strain localization can develop along boundaries when the direction of prismatic slip in a soft α grain is aligned near-parallel to a boundary, since in such a crystallographic configuration, effective barriers for mobile dislocations are lacking.

- Statistically, more strain localization incidents are found near the boundaries surrounded by soft and hard α grains. A significant accumulation of strain is also observed at this type of boundary, implying that this configuration may result in a high risk of damage nucleation.

- Damage evolution curves and cross-sectional micrographs demonstrate that this two-phase titanium alloy exhibits a long nucleation regime up to the strain level much higher than the onset of necking. The phase boundaries act as common paths for micro-void nucleation and growth.

- The α and β phases generally tend to co-deform, leading to a similar amount of strain partitioned into each phase. However, substantial difference in load partitioning between the two phases suggests that the α/β interfaces can be preferential sites for damage nucleation.

In Chapter 4:

- Mechanical twinning can spatially and temporally modulate the dominant strain localization mechanisms in the course of deformation. In an early plasticity regime, before the activation of mechanical twinning, sharp strain bands form along the traces of pyramidal I <c+a> slip, whereas the nucleation and propagation of $\{10\bar{1}2\}$ twins result in the formation of thick strain bands. Due to the substantial reorientation of the lattice accompanied by $\{10\bar{1}2\}$ twinning ($\sim 85°$), prismatic <a> slip is favored and thus activated in the twin domains, leading to vertical slip traces. A significant strain concentration is observed at the locations where such prismatic slip traces and phase boundaries are encountered.

- A series of coordinate transformations that transform the displacement gradient tensor of the twinning shear from the twin reference frame to the sample reference frame demonstrate that the quantitative contribution of the $(\bar{1}102)[1\bar{1}01]$ twinning shear corresponds to $\sim$6% of the local strain along the loading axis.

- Quantitative evaluation of the average size of damage incidents as a function of applied strain shows that the operation of $\{10\bar{1}2\}$ twinning can delay the onset of damage processes, suggesting the potential use of twinning to improve the damage resistance of HCP metals.

In Chapter 5:

- Local strain values exported from *in situ* strain maps demonstrate that the amount of strain partitioned into phases exhibits an inverse correlation with their nanohardness values, showing $\varepsilon_{\mathrm{local,xx}}$: ferrite > retained austenite $\simeq$ bainite and tempered martensite > fresh martensite. In contrast to the local strain evolution of other stable phases, the increment of local strain gradually decreases in retained austenite as the applied strain level increases.

- The *in situ* observations unravel strong neighborhood microstructure effects on the stability of the retained austenite. The transformation of retained austenite is facilitated when it is surrounded by bainite and tempered martensite matrix, while the retained austenite embedded in a ferrite grain is relatively stable and transforms less at the same global strain.

- The local strain evolution of retained austenite is also neighborhood-dependent. The total amount of strain accommodated by retained austenite is the highest when it is enclosed by bainite and tempered martensite matrices. The transformation of retained austenite in general leads to a homogeneous strain distribution in both a ferrite grain and bainite and tempered martensite matrices, but as the overall deformation level increases, the co-deformability of retained austenite and its surroundings decreases in a ferrite grain.
- Despite the limited fraction of fresh martensite in this steel, its contribution to cracking is substantial, as most surface cracks are observed near fresh martensite. Little correlation is observed between the presence of retained austenite and surface cracking.

6.2 Directions for future research

In this thesis, we answer many questions about the origin of microscopic strain localization by comprehensive microstructure inspections through *in situ* SEM/SXRD experiments with titanium and ferrous alloys as model materials. As with all research in science and engineering, new discoveries open up other questions and directions to be addressed. In the following list, we propose further steps to extend the knowledge established in this thesis to broader scientific and engineering studies.

- **Strain localization studies in high microstructural variety.** Although the model materials were carefully chosen for the *in situ* experiments in this thesis, it should also be noted that most quantitative results, such as local strain values, length scales, and frequencies of strain localization incidents, can vary sensitively on microstructure, even for the same bulk concentrations. This indicates that many different microstructural variations have been left for future studies. In particular, morphology, size, and fraction of phases can create a substantial difference in strain distribution. In the two-phase titanium alloy, for example, a more evident strain partitioning is expected between the α and β phases, as the morphology of the β phase becomes circular and island-shaped, and its size and fraction increase.

- **Effects of complex loading conditions on strain distribution.** Another important extension of this thesis is exploring the effects of more complex loading conditions or strain paths, for example, biaxial tension or plane strain tension, other than uniaxial tension. Understanding such strain path effects on microscopic strain localization is fundamentally important for the automotive industry in predicting and enhancing the formability of steels. Studying complex strain path effects is also important since in most forming operations, the strain path that a part undergoes is changing during the processes. For QP steels, as an example, how the mechanical stability and local strain evolution of retained austenite depend on the strain paths would be an interesting topic of future research.

- **Universal features of strain localization.** Another scientific question that emerges from this kind of *in situ* strain mapping is about universality in microscopic strain localization. In most *in situ* strain maps, what has been commonly observed is a lognormal distribution of local strain histograms. Such a distribution tends to possess a long tail towards high local strain values, which may reflect characteristics of strain localization. Studying similarity and non-similarity in strain distributions would also be interesting. A series of local strain histograms in Chapter 4 already suggest that the sudden increase in local strain due to mechanical twinning (or possibly mechanically-induced phase transformation) can generate local strain histograms far from lognormality.

- **High-throughput generation of *in situ* strain dataset.** *In situ* SEM characterization is time-consuming. It requires a substantial amount of time and effort in sample preparation as well as imaging. Therefore, future work may concern how to generate *in situ* strain maps in a more high-throughput manner. One idea could be employing advanced manufacturing techniques capable of local microstructure control, for instance, using laser or electron beam sources. With these techniques, widely adopted in additive manufacturing, different types of microstructure can be produced on one tensile bar, which makes it feasible to screen various microstructural effects in a single *in situ* test.

- **Prediction of critical microstructural features.** With the latest advances in high-resolution *in situ* SEM characterization, there have been an increasing number of quantitative studies on the heterogeneous strain distribution in metals and alloys. As a result, a considerable amount of *in situ* strain map datasets are expected to be generated. An obvious question that arises from this prospect is how to better utilize these datasets to predict safe or detrimental microstructural configurations with high accuracy. This calls for more computational efforts in data mining, including statistical modeling, machine learning, and image processing to capture statistically significant features in the datasets.

Bibliography

[1] T. Nanda, V. Singh, V. Singh, A. Chakraborty, and S. Sharma. Third generation of advanced high-strength steels: Processing routes and properties. *Proceedings of the Institution of Mechanical Engineers, Part L: Journal of Materials: Design and Applications*, 233(2):209–238, 2019.

[2] T. Nanda, V. Singh, G. Singh, M. Singh, and B. R. Kumar. Processing routes, resulting microstructures, and strain rate dependent deformation behaviour of advanced high strength steels for automotive applications. *Archives of Civil and Mechanical Engineering*, 21(1):1–24, 2021.

[3] A. Kalhor, A. Karimi Taheri, H. Mirzadeh, and V. Uthaisangsuk. Processing, microstructure adjustments, and mechanical properties of dual phase steels: a review. *Materials Science and Technology (United Kingdom)*, 37(6):561–591, 2021.

[4] M. R. Bache. A review of dwell sensitive fatigue in titanium alloys: The role of microstructure, texture and operating conditions. *International Journal of Fatigue*, 25(9-11):1079–1087, 9 2003.

[5] M. Peters, J. Kumpfert, C. Ward, and C. Leyens. Titanium Alloys for Aerospace Applications. *Advanced Engineering Materials*, 5(6):419–427, 6 2003.

[6] J. C. Williams and R. R. Boyer. Opportunities and Issues in the Application of Titanium Alloys for Aerospace Components. *Metals*, 10(6):705, 5 2020.

[7] A.-A. Tavassoli. Present limits and improvements of structural materials for fusion reactors – a review. *Journal of Nuclear Materials*, 302(2-3):73–88, 4 2002.

[8] S. J. Zinkle. Advanced materials for fusion technology. *Fusion Engineering and Design*, 74(1-4):31–40, 2005.

[9] K. L. Murty and I. Charit. Structural materials for Gen-IV nuclear reactors: Challenges and opportunities. *Journal of Nuclear Materials*, 383(1-2):189–195, 2008.

[10] M. S. El-Genk and J. M. Tournier. A review of refractory metal alloys and mechanically alloyed-oxide dispersion strengthened steels for space nuclear power systems. *Journal of Nuclear Materials*, 340(1):93–112, 2005.

[11] S. A. Turnage, M. Rajagopalan, K. A. Darling, P. Garg, C. Kale, B. G. Bazehhour, I. Adlakha, B. C. Hornbuckle, C. L. Williams, P. Peralta, and K. N. Solanki. Anomalous mechanical behavior of nanocrystalline binary alloys under extreme conditions. *Nature Communications*, 9(1):1–10, 2018.

[12] I. G. Brodova, V. I. Zel'dovich, and I. V. Khomskaya. Structure–Phase Transformations and Properties of Non-Ferrous Metals and Alloys under Extreme Conditions. *Physics of Metals and Metallography*, 121(7):631–663, 2020.

[13] V. V. Mishakin, K. V. Kurashkin, and A. V. Gonchar. Mechanical behavior investigation of constructional steels applied in amphibious all-terrain vehicle at different temperatures. *IOP Conference Series: Materials Science and Engineering*, 709(3), 2020.

[14] C. C. Tasan, M. Diehl, D. Yan, M. Bechtold, F. Roters, L. Schemmann, C. Zheng, N. Peranio, D. Ponge, M. Koyama, K. Tsuzaki, and D. Raabe. An Overview of Dual-Phase Steels: Advances in Microstructure-Oriented Processing and Micromechanically Guided Design. *Annual Review of Materials Research*, 45:391–431, 2015.

[15] M. Calcagnotto, Y. Adachi, D. Ponge, and D. Raabe. Deformation and fracture mechanisms in fine- and ultrafine-grained ferrite/martensite dual-phase steels and the effect of aging. *Acta Materialia*, 59(2):658–670, 2011.

[16] H. S. Oh, K. Biggs, O. Güvenç, H. Ghassemi-Armaki, N. Pottore, and C. C. Tasan. In-situ investigation of strain partitioning and microstructural strain path development up to and beyond necking. *Acta Materialia*, 215, 2021.

[17] P. J. Jacques, E. Girault, P. Harlet, and F. Delannay. The Developments of Cold-rolled TRIP-assisted Multiphase Steels. Low Silicon TRIP-assisted Multiphase Steels. *ISIJ International*, 41(9):1061–1067, 2001.

[18] P. Jacques. Transformation-induced plasticity for high strength formable steels. *Current Opinion in Solid State and Materials Science*, 8(3-4):259–265, 6 2004.

[19] M. Soleimani, A. Kalhor, and H. Mirzadeh. Transformation-induced plasticity (TRIP) in advanced steels: A review. *Materials Science and Engineering A*, 795(August), 2020.

[20] D. Eylon, S. Fujishiro, P. J. Postans, and F. H. Froes. High-Temperature Titanium Alloys—A Review. *JOM*, 36(11):55–62, 11 1984.

[21] S. L. Semiatin. An Overview of the Thermomechanical Processing of α/β Titanium Alloys: Current Status and Future Research Opportunities. *Metallurgical and Materials Transactions A*, 51(6):2593–2625, 2020.

[22] S. Hémery, P. Villechaise, and D. Banerjee. Microplasticity at Room Temperature in α/β Titanium Alloys. *Metallurgical and Materials Transactions A: Physical Metallurgy and Materials Science*, 51(10):4931–4969, 2020.

[23] T. M. Pollock and S. Tin. Nickel-Based Superalloys for Advanced Turbine Engines: Chemistry, Microstructure and Properties. *Journal of Propulsion and Power*, 22(2):361–374, 3 2006.

[24] A. Baldan. Review Progress in Ostwald ripening theories and their applications to the γ-precipitates in nickel-base superalloys Part II Nickel-base superalloys. *Journal of Materials Science*, 37(12):2379–2405, 2002.

[25] Wikimedia Commons contributors. "File:Boeing 787 first flight.jpg". https://commons.wikimedia.org/w/index.php?title=File:Boeing_787_first_flight.jpg&oldid=482415265. *Wikimedia Commons, the free media repository*, (accessed August 17, 2022).

[26] T. K. Heckel and H.-J. Christ. Isothermal and thermomechanical fatigue of titanium alloys. *Procedia Engineering*, 2(1):845–854, 4 2010.

[27] Wikimedia Commons contributors. "File:2009-03-20 Red car NB on S Lasalle St in Durham.jpg". https://commons.wikimedia.org/w/index.php?title=File:2009-03-20_Red_car_NB_on_S_Lasalle_St_in_Durham.jpg&oldid=671645191. *Wikimedia Commons, the free media repository*, (accessed August 17, 2022).

[28] S. Han, P. Eisenlohr, and M. A. Crimp. ECCI based characterization of dislocation shear in polycrystalline arrays during heterogeneous deformation of commercially pure titanium. *Materials Characterization*, 142(June):504–514, 2018.

[29] S. Wei, J. Kim, and C. C. Tasan. Boundary micro-cracking in metastable Fe45Mn35Co10Cr10 high-entropy alloys. *Acta Materialia*, 168:76–86, 2019.

[30] R. Liu, Z. J. Zhang, L. L. Li, X. H. An, and Z. F. Zhang. Microscopic mechanisms contributing to the synchronous improvement of strength and plasticity (SISP) for TWIP copper alloys. *Scientific Reports*, 5:1–7, 2015.

[31] T. R. Bieler, P. Eisenlohr, F. Roters, D. Kumar, D. E. Mason, M. A. Crimp, and D. Raabe. The role of heterogeneous deformation on damage nucleation at grain boundaries in single phase metals. *International Journal of Plasticity*, 25(9):1655–1683, 2009.

[32] A. E. Tekkaya, P.-O. Bouchard, S. Bruschi, and C. C. Tasan. Damage in metal forming. *CIRP Annals*, 69(2):600–623, 2020.

[33] C. Tasan, M. Diehl, D. Yan, C. Zambaldi, P. Shanthraj, F. Roters, and D. Raabe. Integrated experimental–simulation analysis of stress and strain partitioning in multiphase alloys. *Acta Materialia*, 81:386–400, 12 2014.

[34] J. P. M. Hoefnagels, C. C. Tasan, F. Maresca, F. J. Peters, and V. G. Kouznetsova. Retardation of plastic instability via damage-enabled microstrain delocalization. *Journal of Materials Science*, 50(21):6882–6897, 2015.

[35] C. Tasan, J. Hoefnagels, M. Diehl, D. Yan, F. Roters, and D. Raabe. Strain localization and damage in dual phase steels investigated by coupled in-situ deformation experiments and crystal plasticity simulations. *International Journal of Plasticity*, 63:198–210, 12 2014.

[36] D. Yan, C. C. Tasan, and D. Raabe. High resolution in situ mapping of microstrain and microstructure evolution reveals damage resistance criteria in dual phase steels. *Acta Materialia*, 96:399–409, 2015.

[37] M.-M. Wang, C. C. Tasan, D. Ponge, A.-C. Dippel, and D. Raabe. Nanolaminate transformation-induced plasticity–twinning-induced plasticity steel with dynamic strain partitioning and enhanced damage resistance. *Acta Materialia*, 85:216–228, 2015.

[38] Z. Chen, W. Lenthe, J. C. Stinville, M. Echlin, T. M. Pollock, and S. Daly. High-Resolution Deformation Mapping Across Large Fields of View Using Scanning Electron Microscopy and Digital Image Correlation. *Experimental Mechanics*, 58(9):1407–1421, 2018.

[39] J. C. Stinville, N. Vanderesse, F. Bridier, P. Bocher, and T. M. Pollock. High resolution mapping of strain localization near twin boundaries in a nickel-based superalloy. *Acta Materialia*, 98:29–42, 2015.

[40] A. P. Hammersley. FIT2D: an introduction and overview. *European synchrotron radiation facility internal report ESRF97HA02T*, 68:58, 1997.

[41] R. T. Ott, F. Sansoz, J. F. Molinari, J. Almer, K. T. Ramesh, and T. C. Hufnagel. Micromechanics of deformation of metallic-glass–matrix composites from in situ synchrotron strain measurements and finite element modeling. *Acta Materialia*, 53(7):1883–1893, 2005.

[42] R. Blondé, E. Jimenez-Melero, L. Zhao, J. P. Wright, E. Brück, S. Van Der Zwaag, and N. H. Van Dijk. High-energy X-ray diffraction study on the temperature-dependent mechanical stability of retained austenite in low-alloyed TRIP steels. *Acta Materialia*, 60(2):565–577, 2012.

[43] L. Ma, L. Wang, Z. Nie, F. Wang, Y. Xue, J. Zhou, T. Cao, Y. Wang, and Y. Ren. Reversible deformation-induced martensitic transformation in Al 0 . 6 CoCrFeNi high-entropy alloy investigated by in situ synchrotron- based high-energy X-ray diffraction. *Acta Materialia*, 128:12–21, 2017.

[44] M. Zhang, L. Li, J. Ding, Q. Wu, Y. D. Wang, J. Almer, F. Guo, and Y. Ren. Temperature-dependent micromechanical behavior of medium-Mn transformation-induced-plasticity steel studied by in situ synchrotron X-ray diffraction. *Acta Materialia*, 141:294–303, 2017.

[45] L. Lutterotti, M. Bortolotti, G. Ischia, I. Lonardelli, and H. R. Wenk. Rietveld texture analysis from diffraction images. *Zeitschrift fur Kristallographie, Supplement*, 1(26):125–130, 2007.

[46] L. Lutterotti. Total pattern fitting for the combined size-strain-stress-texture determination in thin film diffraction. *Nuclear Instruments and Methods in Physics Research, Section B: Beam Interactions with Materials and Atoms*, 268(3-4):334–340, 2010.

[47] L. Lutterotti, R. Vasin, and H.-R. R. Wenk. Rietveld texture analysis from synchrotron diffraction images. I. Calibration and basic analysis. *Powder Diffraction*, 29(1):76–84, 2014.

[48] H.-R. Wenk, L. Lutterotti, P. Kaercher, W. Kanitpanyacharoen, L. Miyagi, and R. Vasin. Rietveld texture analysis from synchrotron diffraction images. II. Complex multiphase materials and diamond anvil cell experiments. *Powder Diffraction*, 29(3):220–232, 2014.

[49] T. H. de Keijser, J. I. Langford, E. J. Mittemeijer, and A. B. P. Vogels. Use of the Voigt function in a single-line method for the analysis of X-ray diffraction line broadening. *Journal of Applied Crystallography*, 15(3):308–314, 1982.

[50] R. Delhez, T. H. de Keijser, J. I. Langford, D. Louer, E. J. Mittemeijer, and E. J. Sonneveld. Crystal imperfection broadening and peak shape in the Rietveld method. *The Rietveld Method*, pages 132–166, 1993.

[51] L. Lutterotti, D. Chateigner, S. Ferrari, and J. Ricote. Texture, residual stress and structural analysis of thin films using a combined X-ray analysis. *Thin Solid Films*, 450(1):34–41, 2004.

[52] W. C. Oliver and G. M. Pharr. An improved technique for determining hardness and elastic madulus using load and displacement. *J Mater Res*, 7(1):1564–1583, 1992.

[53] M. Peters and C. Leyens. Non-Aerospace Applications of Titanium and Titanium Alloys. In *Titanium and Titanium Alloys*, chapter 15, pages 393–422. Wiley-VCH Verlag GmbH & Co. KGaA, Weinheim, FRG, 1 2005.

[54] D. Banerjee and J. C. Williams. Perspectives on Titanium Science and Technology. *Acta Materialia*, 61(3):844–879, 2013.

[55] S. Wei, L. Huang, X. Li, Y. Jiao, W. Ren, and L. Geng. Network-Strengthened Ti-6Al-4V/(TiC+TiB) Composites: Powder Metallurgy Processing and Enhanced Tensile Properties at Elevated Temperatures. *Metallurgical and Materials Transactions A*, 50(8):3629–3645, 2019.

[56] I. Weiss and S. L. Semiatin. Thermomechanical processing of beta titanium alloys - An overview. *Materials Science and Engineering A*, 243(1-2):46–65, 1998.

[57] S. L. Semiatin, V. Seetharaman, and I. Weiss. The thermomechanical processing of alpha/beta titanium alloys. *JOM*, 49(6):33–39, 1997.

[58] S. L. Semiatin, S. L. Knisley, P. N. Fagin, D. R. Barker, and F. Zhang. Microstructure evolution during alpha-beta heat treatment of Ti-6Al-4V. *Metallurgical and Materials Transactions A*, 34(10):2377–2386, 2003.

[59] T. S. Jun, G. Sernicola, F. P. Dunne, and T. B. Britton. Local deformation mechanisms of two-phase Ti alloy. *Materials Science and Engineering A*, 649:39–47, 2016.

[60] F. P. E. Dunne, A. Walker, and D. Rugg. A systematic study of hcp crystal orientation and morphology effects in polycrystal deformation and fatigue. *Proceedings of the Royal Society A: Mathematical, Physical and Engineering Sciences*, 463(2082):1467–1489, 6 2007.

[61] F. Bridier, P. Villechaise, and J. Mendez. Analysis of the different slip systems activated by tension in a α/β titanium alloy in relation with local crystallographic orientation. *Acta Materialia*, 53(3):555–567, 2005.

[62] M. A. Meyers, G. Subhash, B. K. Kad, and L. Prasad. Evolution of microstructure and shear-band formation in α-hcp titanium. *Mechanics of Materials*, 17:175–193, 1994.

[63] H. Abdolvand and A. J. Wilkinson. Assessment of residual stress fields at deformation twin tips and the surrounding environments. *Acta Materialia*, 105:219–231, 2016.

[64] M. Arul Kumar, I. J. Beyerlein, and C. N. Tomé. Effect of local stress fields on twin characteristics in HCP metals. *Acta Materialia*, 116:143–154, 2016.

[65] S. Wang, Y. Zhang, C. Schuman, J.-S. Lecomte, X. Zhao, L. Zuo, M.-J. Philippe, and C. Esling. Study of twinning/detwinning behaviors of Ti by interrupted in situ tensile tests. *Acta Materialia*, 82:424–436, 2015.

[66] Y. Chong, T. Bhattacharjee, M.-H. Park, A. Shibata, and N. Tsuji. Factors determining room temperature mechanical properties of bimodal microstructures in Ti-6Al-4V alloy. *Materials Science and Engineering: A*, 730:217–222, 2018.

[67] L. Choisez, L. Ding, M. Marteleur, H. Idrissi, T. Pardoen, and P. J. Jacques. High temperature rise dominated cracking mechanisms in ultra-ductile and tough titanium alloy. *Nature Communications*, 11(1):1–8, 2020.

[68] Z. Zhang, D. Lunt, H. Abdolvand, A. J. Wilkinson, M. Preuss, and F. P. E. Dunne. Quantitative investigation of micro slip and localization in polycrystalline materials under uniaxial tension. *International Journal of Plasticity*, 108:88–106, 2018.

[69] Y. Guo, T. B. Britton, and A. J. Wilkinson. Slip band–grain boundary interactions in commercial-purity titanium. *Acta Materialia*, 76:1–12, 2014.

[70] Y. Guo, D. M. Collins, E. Tarleton, F. Hofmann, A. J. Wilkinson, and T. B. Britton. Dislocation density distribution at slip band-grain boundary intersections. *Acta Materialia*, 182:172–183, 2020.

[71] M. F. Savage, J. Tatalovich, M. Zupan, K. J. Hemker, and M. J. Mills. Deformation mechanisms and microtensile behavior of single colony Ti–6242Si. *Materials Science and Engineering: A*, 319-321:398–403, 2001.

[72] A. K. Ackerman, V. A. Vorontsov, I. Bantounas, Y. Zheng, Y. Chang, T. McAuliffe, W. A. Clark, H. L. Fraser, B. Gault, D. Rugg, and D. Dye. Interface characteristics in an α+β titanium alloy. *Physical Review Materials*, 4(1):1–7, 1 2020.

[73] M. F. Savage, J. Tatalovich, and M. J. Mills. Anisotropy in the room-temperature deformation of α–β colonies in titanium alloys: role of the α–β interface. *Philosophical Magazine*, 84(11):1127–1154, 4 2004.

[74] Z. Zhang, T.-S. Jun, T. B. Britton, and F. P. E. Dunne. Determination of Ti-6242 α and β slip properties using micro-pillar test and computational crystal plasticity. *Journal of the Mechanics and Physics of Solids*, 95:393–410, 2016.

[75] Z. Zheng, S. Waheed, D. S. Balint, and F. P. E. Dunne. Slip transfer across phase boundaries in dual phase titanium alloys and the effect on strain rate sensitivity. *International Journal of Plasticity*, 104(October 2017):23–38, 2018.

[76] T. R. Bieler, P. Eisenlohr, C. Zhang, H. J. Phukan, and M. A. Crimp. Grain boundaries and interfaces in slip transfer. *Current Opinion in Solid State and Materials Science*, 18(4):212–226, 2014.

[77] Z. Yan, K. Wang, Y. Zhou, X. Zhu, R. Xin, and Q. Liu. Crystallographic orientation dependent crack nucleation during the compression of a widmannstätten-structure α/β titanium alloy. *Scripta Materialia*, 156:110–114, 2018.

[78] J. R. Seal, M. A. Crimp, T. R. Bieler, and C. J. Boehlert. Analysis of slip transfer and deformation behavior across the α/β interface in Ti–5Al–2.5Sn (wt.%) with an equiaxed microstructure. *Materials Science and Engineering: A*, 552:61–68, 2012.

[79] S. R. Kalidindi, A. Bhattacharyya, and R. D. Doherty. Detailed Analyses of Grain-Scale Plastic Deformation in Columnar Polycrystalline Aluminium Using Orientation Image Mapping and Crystal Plasticity Models. *Proceedings: Mathematical, Physical and Engineering Sciences*, 460(2047):1935–1956, 11 2004.

[80] T. R. Bieler, M. A. Crimp, Y. Yang, L. Wang, P. Eisenlohr, D. E. Mason, W. Liu, and G. E. Ice. Strain heterogeneity and damage nucleation at grain boundaries during monotonic deformation in commercial purity titanium. *JOM*, 61(12):45–52, 2009.

[81] M. Zubair, S. Sandlöbes-Haut, M. A. Wollenweber, K. Bugelnig, C. F. Kusche, G. Requena, and S. Korte-Kerzel. Strain heterogeneity and micro-damage nucleation under tensile stresses in an Mg–5Al–3Ca alloy with an intermetallic skeleton. *Materials Science and Engineering: A*, 767:138414, 2019.

[82] H. Ghadbeigi, C. Pinna, S. Celotto, and J. R. Yates. Local plastic strain evolution in a high strength dual-phase steel. *Materials Science and Engineering: A*, 527(18):5026–5032, 2010.

[83] T. Zhang, J. Jiang, B. A. Shollock, T. B. Britton, and F. P. E. Dunne. Slip localization and fatigue crack nucleation near a non-metallic inclusion in polycrystalline nickel-based superalloy. *Materials Science and Engineering: A*, 641:328–339, 2015.

[84] D. Raabe, M. Sachtleber, Z. Zhao, F. Roters, and S. Zaefferer. Micromechanical and macromechanical effects in grain scale polycrystal plasticity experimentation and simulation. *Acta Materialia*, 49(17):3433–3441, 2001.

[85] S. K. Mishra, P. Pant, K. Narasimhan, A. D. Rollett, and I. Samajdar. On the widths of orientation gradient zones adjacent to grain boundaries. *Scripta Materialia*, 61(3):273–276, 2009.

[86] J. S. Weaver, M. W. Priddy, D. L. McDowell, and S. R. Kalidindi. On capturing the grain-scale elastic and plastic anisotropy of alpha-Ti with spherical nanoindentation and electron back-scattered diffraction. *Acta Materialia*, 117:23–34, 2016.

[87] P. Baudoin, T. Hama, and H. Takuda. Influence of critical resolved shear stress ratios on the response of a commercially pure titanium oligocrystal: Crystal plasticity simulations and experiment. *International Journal of Plasticity*, 115(June 2018):111–131, 2019.

[88] J. L. Warwick, N. G. Jones, K. M. Rahman, and D. Dye. Lattice strain evolution during tensile and compressive loading of CP Ti. *Acta Materialia*, 60(19):6720–6731, 2012.

[89] J. C. Williams, R. G. Baggerly, and N. E. Paton. Deformation behavior of HCP Ti-Al alloy single crystals. *Metallurgical and Materials Transactions A*, 33(3):837–850, 2002.

[90] H. Li, D. E. Mason, T. R. Bieler, C. J. Boehlert, and M. A. Crimp. Methodology for estimating the critical resolved shear stress ratios of α-phase Ti using EBSD-based trace analysis. *Acta Materialia*, 61(20):7555–7567, 2013.

[91] J. W. Won, C. H. Park, J. Hong, C. S. Lee, and S. G. Hong. Simultaneous Improvement in the Strength and Formability of Commercially Pure Titanium via Twinning-induced Crystallographic Texture Control. *Scientific Reports*, 9(1):1–11, 2019.

[92] M. A. Kumar and I. J. Beyerlein. Local microstructure and micromechanical stress evolution during deformation twinning in hexagonal polycrystals. *Journal of Materials Research*, 35(3):217–241, 2020.

[93] D. Lunt, R. Thomas, M. D. Atkinson, A. Smith, R. Sandala, J. Q. da Fonseca, and M. Preuss. Understanding the role of local texture variation on slip activity in a two-phase titanium alloy. *Acta Materialia*, 216:117111, 2021.

[94] S. Zhang, W. Zeng, Q. Zhao, L. Ge, and M. Zhang. In situ SEM study of tensile deformation of a near-β titanium alloy. *Materials Science and Engineering: A*, 708(September):574–581, 2017.

[95] F. Benmessaoud, M. Cheikh, V. Velay, V. Vidal, and H. Matsumoto. Role of grain size and crystallographic texture on tensile behavior induced by sliding mechanism in Ti-6Al-4V alloy. *Materials Science and Engineering: A*, 774(October 2019):138835, 2020.

[96] H. Abdolvand, J. Wright, and A. J. Wilkinson. Strong grain neighbour effects in polycrystals. *Nature Communications*, 9(1):171, 2018.

[97] Z. Zheng, D. S. Balint, and F. P. E. Dunne. Dwell fatigue in two Ti alloys: An integrated crystal plasticity and discrete dislocation study. *Journal of the Mechanics and Physics of Solids*, 96:411–427, 11 2016.

[98] Z. Zheng, D. S. Balint, and F. P. E. Dunne. Investigation of slip transfer across HCP grain boundaries with application to cold dwell facet fatigue. *Acta Materialia*, 127:43–53, 2017.

[99] J. D. Eshelby, F. C. Frank, and F. R. N. Nabarro. XLI. The equilibrium of linear arrays of dislocations. *The London, Edinburgh, and Dublin Philosophical Magazine and Journal of Science*, 42(327):351–364, 4 1951.

[100] T. Benjamin Britton and A. J. Wilkinson. Stress fields and geometrically necessary dislocation density distributions near the head of a blocked slip band. *Acta Materialia*, 60(16):5773–5782, 2012.

[101] M. P. Echlin, J. C. Stinville, V. M. Miller, W. C. Lenthe, and T. M. Pollock. Incipient slip and long range plastic strain localization in microtextured Ti-6Al-4V titanium. *Acta Materialia*, 114:164–175, 2016.

[102] M. Kasemer, M. P. Echlin, J. C. Stinville, T. M. Pollock, and P. Dawson. On slip initiation in equiaxed α/β Ti-6Al-4V. *Acta Materialia*, 136:288–302, 2017.

[103] S. Wei, J. Kim, and C. C. Tasan. In-situ investigation of plasticity in a Ti-Al-V-Fe (α+β) alloy: Slip mechanisms, strain localization, and partitioning. *International Journal of Plasticity*, 148:103131, 1 2022.

[104] T. R. Bieler, P. D. Nicolaou, and S. L. Semiatin. An experimental and theoretical investigation of the effect of local colony orientations and misorientation on cavitation during hot working of Ti-6Al-4V. *Metallurgical and Materials Transactions A*, 36(1):129, 2005.

[105] P. D. Nicolaou, J. D. Miller, and S. L. Semiatin. Cavitation during hot-torsion testing of Ti-6Al-4V. *Metallurgical and Materials Transactions A*, 36(12):3461, 2005.

[106] A. C. Lewis, S. M. Qidwai, and A. B. Geltmacher. Slip Systems and Initiation of Plasticity in a Body-Centered-Cubic Titanium Alloy. *Metallurgical and Materials Transactions A*, 41(10):2522–2531, 2010.

[107] D. Raabe. Simulation of rolling textures of b.c.c. metals considering grain interactions and crystallographic slip on {110}, {112} and {123} planes. *Materials Science and Engineering: A*, 197(1):31–37, 1995.

[108] P. J. Ashton, T.-S. Jun, Z. Zhang, T. B. Britton, A. M. Harte, S. B. Leen, and F. P. E. Dunne. The effect of the beta phase on the micromechanical response of dual-phase titanium alloys. *International Journal of Fatigue*, 100:377–387, 2017.

[109] J.-M. Oh, J.-W. Lim, B.-G. Lee, C.-Y. Suh, S.-W. Cho, S.-W. Lee, and G.-S. Choi. Grain Refinement and Hardness Increase of Titanium via Trace Element Addition. *MATERIALS TRANSACTIONS*, 51(11):2009–2012, 2010.

[110] S. James, Y. Kosaka, R. Thomas, and P. Garratt. Timetal® 407: A Titanium Alloy to Enable Cost Reduction. *Proceedings of the 13th World Conference on Titanium*, pages 721–725, 5 2016.

[111] A. A. Salem, S. R. Kalidindi, R. D. Doherty, and S. L. Semiatin. Strain hardening due to deformation twinning in α-titanium: Mechanisms. *Metallurgical and Materials Transactions A*, 37(1):259–268, 2006.

[112] S. Wei, G. Zhu, and C. C. Tasan. Slip-twinning interdependent activation across phase boundaries: An in-situ investigation of a Ti-Al-V-Fe (α+β) alloy. *Acta Materialia*, 206:116520, 2021.

[113] J. L. W. Warwick, J. Coakley, S. L. Raghunathan, R. J. Talling, and D. Dye. Effect of texture on load partitioning in Ti-6Al-4V. *Acta Materialia*, 60(10):4117–4127, 2012.

[114] S. R. Agnew, A. Singh, C. A. Calhoun, R. P. Mulay, J. J. Bhattacharyya, H. Somekawa, T. Mukai, B. Clausen, and P. D. Wu. In-situ neutron diffraction of a quasicrystal-containing Mg alloy interpreted using a new polycrystal plasticity model of hardening due to {10.2} tensile twinning. *International Journal of Plasticity*, 100:34–51, 2018.

[115] H. El Kadiri, J. C. Baird, J. Kapil, A. L. Oppedal, M. Cherkaoui, and S. C. Vogel. Flow asymmetry and nucleation stresses of {101¯2} twinning and non-basal slip in magnesium. *International Journal of Plasticity*, 44:111–120, 2013.

[116] S. Wang, C. Schuman, L. Bao, J. S. Lecomte, Y. Zhang, J. M. Raulot, M. J. Philippe, X. Zhao, and C. Esling. Variant selection criterion for twin variants in titanium alloys deformed by rolling. *Acta Materialia*, 60(9):3912–3919, 2012.

[117] D. Zhang, L. Wang, H. Zhang, A. Maldar, G. Zhu, W. Chen, J.-S. Park, J. Wang, and X. Zeng. Effect of heat treatment on the tensile behavior of selective laser melted Ti-6Al-4V by in situ X-ray characterization. *Acta Materialia*, 189:93–104, 2020.

[118] P. R. Dawson, D. E. Boyce, J.-S. Park, E. Wielewski, and M. P. Miller. Determining the strengths of HCP slip systems using harmonic analyses of lattice strain distributions. *Acta Materialia*, 144:92–106, 2018.

[119] S. L. Raghunathan, A. M. Stapleton, R. J. Dashwood, M. Jackson, and D. Dye. Micromechanics of Ti–10V–2Fe–3Al: In situ synchrotron characterisation and modelling. *Acta Materialia*, 55(20):6861–6872, 2007.

[120] A. M. Stapleton, S. L. Raghunathan, I. Bantounas, H. J. Stone, T. C. Lindley, and D. Dye. Evolution of lattice strain in Ti–6Al–4V during tensile loading at room temperature. *Acta Materialia*, 56(20):6186–6196, 2008.

[121] C. Tekoğlu, J. W. Hutchinson, and T. Pardoen. On localization and void coalescence as a precursor to ductile fracture. *Philosophical Transactions of the Royal Society A: Mathematical, Physical and Engineering Sciences*, 373(2038):20140121, 3 2015.

[122] T. R. Bieler, R. Alizadeh, M. Peña-Ortega, and J. Llorca. An analysis of (the lack of) slip transfer between near-cube oriented grains in pure Al. *International Journal of Plasticity*, 118:269–290, 2019.

[123] S. Wei, S. J. Kim, J. Kang, Y. Zhang, Y. Zhang, T. Furuhara, E. S. Park, and C. C. Tasan. Natural-mixing guided design of refractory high-entropy alloys with as-cast tensile ductility. *Nature Materials*, 19(11):1175–1181, 2020.

[124] S. Wei and C. C. Tasan. Deformation faulting in a metastable CoCrNiW complex concentrated alloy: A case of negative intrinsic stacking fault energy? *Acta Materialia*, 200:992–1007, 11 2020.

[125] T.-S. Jun, X. Maeder, A. Bhowmik, G. Guillonneau, J. Michler, F. Giuliani, and T. B. Britton. The role of β-titanium ligaments in the deformation of dual phase titanium alloys. *Materials Science and Engineering: A*, 746:394–405, 2019.

[126] Z. Kloenne, G. Viswanathan, S. Fox, M. Loretto, and H. L. Fraser. Interface and colony boundary sliding as a deformation mechanism in a novel titanium alloy. *Scripta Materialia*, 178:418–421, 2020.

[127] C. K. Dolph, D. J. da Silva, M. J. Swenson, and J. P. Wharry. Plastic zone size for nanoindentation of irradiated Fe—9%Cr ODS. *Journal of Nuclear Materials*, 481:33–45, 2016.

[128] B. E. Warren and B. L. Averbach. The Separation of Cold-Work Distortion and Particle Size Broadening in X-Ray Patterns. *Journal of Applied Physics*, 23(4):497, 4 1952.

[129] G. K. Williamson and W. H. Hall. X-ray line broadening from filed aluminium and wolfram. *Acta metallurgica*, 1(1):22–31, 1953.

[130] M. H. Yoo. Slip, twinning, and fracture in hexagonal close-packed metals. *Metallurgical Transactions A*, 12(3):409–418, 3 1981.

[131] I. J. Beyerlein, X. Zhang, and A. Misra. Growth Twins and Deformation Twins in Metals. *Annual Review of Materials Research*, 44(1):329–363, 2014.

[132] I. J. Beyerlein and M. Arul Kumar. The Stochastic Nature of Deformation Twinning: Application to HCP Materials. In *Handbook of Materials Modeling*, pages 1–39. Springer International Publishing, Cham, 2018.

[133] M. R. Barnett. Twinning and the ductility of magnesium alloys. Part I: "Tension" twins. *Materials Science and Engineering A*, 464(1-2):1–7, 2007.

[134] M. R. Barnett. Twinning and the ductility of magnesium alloys. Part II. "Contraction" twins. *Materials Science and Engineering A*, 464(1-2):8–16, 2007.

[135] K. D. Molodov, T. Al-Samman, D. A. Molodov, and G. Gottstein. Mechanisms of exceptional ductility of magnesium single crystal during deformation at room temperature: Multiple twinning and dynamic recrystallization. *Acta Materialia*, 76:314–330, 2014.

[136] S. H. Park, S. G. Hong, and C. S. Lee. Enhanced stretch formability of rolled Mg-3Al-1Zn alloy at room temperature by initial {10-12} twins. *Materials Science and Engineering A*, 578:271–276, 2013.

[137] M. Arul Kumar, I. J. Beyerlein, and C. N. Tomé. A measure of plastic anisotropy for hexagonal close packed metals: Application to alloying effects on the formability of Mg. *Journal of Alloys and Compounds*, 695:1488–1497, 2017.

[138] F. Yang, S. M. Yin, S. X. Li, and Z. F. Zhang. Crack initiation mechanism of extruded AZ31 magnesium alloy in the very high cycle fatigue regime. *Materials Science and Engineering A*, 491(1-2):131–136, 2008.

[139] S. M. Yin, F. Yang, X. M. Yang, S. D. Wu, S. X. Li, and G. Y. Li. The role of twinning-detwinning on fatigue fracture morphology of Mg-3%Al-1%Zn alloy. *Materials Science and Engineering A*, 494(1-2):397–400, 2008.

[140] N. Bosh, C. Müller, and H. Mozaffari-Jovein. Deformation twinning in cp-Ti and its effect on fatigue cracking. *Materials Characterization*, 155(July), 2019.

[141] D. Ando, J. Koike, and Y. Sutou. The role of deformation twinning in the fracture behavior and mechanism of basal textured magnesium alloys. *Materials Science and Engineering A*, 600:145–152, 2014.

[142] B. A. Simkin, B. C. Ng, M. A. Crimp, and T. R. Bieler. Crack opening due to deformation twin shear at grain boundaries in near-γ TiAl. *Intermetallics*, 15(1):55–60, 2007.

[143] W. F. Hosford. On Orientation Changes Accompanying Slip and Twinning. *Texture of Crystalline Solids*, 2(3):175–182, 1 1977.

[144] G. Winther, L. Margulies, S. Schmidt, and H. F. Poulsen. Lattice rotations of individual bulk grains Part II: Correlation with initial orientation and model comparison. *Acta Materialia*, 52(10):2863–2872, 2004.

[145] P. Chen, S. C. Mao, Y. Liu, F. Wang, Y. F. Zhang, Z. Zhang, and X. D. Han. In-situ EBSD study of the active slip systems and lattice rotation behavior of surface grains in aluminum alloy during tensile deformation. *Materials Science and Engineering A*, 580:114–124, 2013.

[146] J. Jiang, A. Godfrey, W. Liu, and Q. Liu. Microtexture evolution via deformation twinning and slip during compression of magnesium alloy AZ31. *Materials Science and Engineering A*, 483-484(1-2 C):576–579, 2008.

[147] D. Culbertson, Q. Yu, and Y. Jiang. In situ observation of cross-grain twin pair formation in pure magnesium. *Philosophical Magazine Letters*, 98(4):139–146, 2018.

[148] A. A. Salem, S. R. Kalidindi, and R. D. Doherty. Strain hardening of titanium: Role of deformation twinning. *Acta Materialia*, 51(14):4225–4237, 2003.

[149] S. K. Sahoo, S. Biswas, L. S. Toth, P. C. Gautam, and B. Beausir. Strain hardening, twinning and texture evolution in magnesium alloy using the all twin variant polycrystal modelling approach. *International Journal of Plasticity*, 128(January):102660, 2020.

[150] L. Balogh, S. R. Niezgoda, A. K. Kanjarla, D. W. Brown, B. Clausen, W. Liu, and C. N. Tomé. Spatially resolved in situ strain measurements from an interior twinned grain in bulk polycrystalline AZ31 alloy. *Acta Materialia*, 61(10):3612–3620, 2013.

[151] I. B. Üçel, E. Kapan, O. Türkoğlu, and C. C. Aydiner. In situ investigation of strain heterogeneity and microstructural shear bands in rolled Magnesium AZ31. *International Journal of Plasticity*, 118(February):233–251, 2019.

[152] N. Shafaghi, E. Kapan, and C. C. Aydıner. Cyclic Strain Heterogeneity and Damage Formation in Rolled Magnesium Via In Situ Microscopic Image Correlation. *Experimental Mechanics*, 60(6):735–751, 2020.

[153] L. Wang, Y. Yang, P. Eisenlohr, T. R. Bieler, M. A. Crimp, and D. E. Mason. Twin Nucleation by Slip Transfer across Grain Boundaries in Commercial Purity Titanium. *Metallurgical and Materials Transactions A*, 41(2):421, 2009.

[154] F. Wang, S. Sandlöbes, M. Diehl, L. Sharma, F. Roters, and D. Raabe. In situ observation of collective grain-scale mechanics in Mg and Mg-rare earth alloys. *Acta Materialia*, 80:77–93, 2014.

[155] H.-J. Bunge. Orientation of Individual Crystallites. In H.-J. B. T. T. A. i. M. S. Bunge, editor, *Texture Analysis in Materials Science*, chapter 2, pages 3–41. Elsevier, 1982.

[156] O. MATSUMURA, Y. SAKUMA, and H. TAKECHI. Enhancement of elongation by retained austenite in intercritical annealed 0.4C-1.5Si-0.8Mn steel. *Transactions of the Iron and Steel Institute of Japan*, 27(7):570–579, 1987.

[157] Y. Sakuma, D. K. Matlock, and G. Krauss. Intercritically annealed and isothermally transformed 0.15 Pct C steels containing 1.2 Pct Si-1.5 Pct Mn and 4 Pct Ni: Part I. transformation, microstructure, and room-temperature mechanical properties. *Metallurgical Transactions A*, 23(4):1221–1232, 4 1992.

[158] P. Jacques, X. Cornet, P. Harlet, J. Ladriere, and F. Delannay. Enhancement of the mechanical properties of a low-carbon, low-silicon steel by formation of a multiphased microstructure containing retained austenite. *Metallurgical and Materials Transactions A: Physical Metallurgy and Materials Science*, 29(9):2383–2393, 1998.

[159] B. De Cooman. Structure–properties relationship in TRIP steels containing carbide-free bainite. *Current Opinion in Solid State and Materials Science*, 8(3-4):285–303, 6 2004.

[160] Y. Sakuma, O. Matsumura, and O. Akisue. Influence of C Content and annealing Temperature on Microstructure and Mechanical Properties of 400.DEG.C. Transformed Steel Containing Retained Austenite. *ISIJ International*, 31(11):1348–1353, 1991.

[161] J. Speer, D. K. Matlock, B. C. De Cooman, and J. G. Schroth. Carbon partitioning into austenite after martensite transformation. *Acta Materialia*, 51(9):2611–2622, 2003.

[162] J. G. Speer, D. V. Edmonds, F. C. Rizzo, and D. K. Matlock. Partitioning of carbon from supersaturated plates of ferrite, with application to steel processing and fundamentals of the bainite transformation. *Current Opinion in Solid State and Materials Science*, 8(3-4):219–237, 2004.

[163] B. C. De Cooman and J. G. Speer. Quench and partitioning steel: A new AHSS concept for automotive anti-intrusion applications. *Steel Research International*, 77(9-10):634–640, 2006.

[164] M. J. Santofimia, L. Zhao, R. Petrov, C. Kwakernaak, W. G. Sloof, and J. Sietsma. Microstructural development during the quenching and partitioning process in a newly designed low-carbon steel. *Acta Materialia*, 59(15):6059–6068, 2011.

[165] H. S. Zhao, X. Zhu, W. Li, X. J. Jin, L. Wang, H. Jiao, and D. M. Jiang. Austenite stability for quenching and partitioning treated steel revealed by colour tint-etching method. *Materials Science and Technology (United Kingdom)*, 30(9):1008–1013, 2014.

[166] M. Carpio, J. Calvo, O. García, J. P. Pedraza, and J. M. Cabrera. Heat treatment design for a QP steel: Effect of partitioning temperature. *Metals*, 11(7):1–15, 2021.

[167] J. Patel and M. Cohen. Criterion for the action of applied stress in the martensitic transformation. *Acta Metallurgica*, 1(5):531–538, 9 1953.

[168] I. Tamura. Deformation-induced martensitic transformation and transformation-induced plasticity in steels. *Metal Science*, 16(5):245–253, 5 1982.

[169] S. Chatterjee and H. K. D. H. Bhadeshia. Transformation induced plasticity assisted steels: stress or strain affected martensitic transformation? *Materials Science and Technology*, 23(9):1101–1104, 9 2007.

[170] H. Geijselaers and E. Perdahcıoğlu. Mechanically induced martensitic transformation as a stress-driven process. *Scripta Materialia*, 60(1):29–31, 1 2009.

[171] G. Olson and M. Cohen. A mechanism for the strain-induced nucleation of martensitic transformations. *Journal of the Less Common Metals*, 28(1):107–118, 7 1972.

[172] G. B. Olson and M. Cohen. Kinetics of strain-induced martensitic nucleation. *Metallurgical Transactions A*, 6(4):791–795, 4 1975.

[173] R. Stringfellow, D. Parks, and G. Olson. A constitutive model for transformation plasticity accompanying strain-induced martensitic transformations in metastable austenitic steels. *Acta Metallurgica et Materialia*, 40(7):1703–1716, 7 1992.

[174] X. Chen, C. Niu, C. Lian, and J. Lin. The Evaluation of Formability of the 3rd Generation Advanced High Strength Steels QP980 based on Digital Image Correlation Method. *Procedia Engineering*, 207:556–561, 2017.

[175] J. Cramer, D. Adams, M. P. Miles, D. T. Fullwood, E. R. Homer, T. Brown, R. Misha, and A. Sachdev. Effect of strain path on forming limits and retained austenite transformation in Q&P 1180 steel. *Materials Science and Engineering A*, 734(May):192–199, 2018.

[176] S. Han, Y. Chang, C. Wang, Y. Han, and H. Dong. Experimental and Numerical Investigations on the Damage Induced in the Shearing Process for QP980 Steel. *Materials*, 15(9), 2022.

[177] K.-i. Sugimoto, K. Nakano, S.-m. Song, and T. Kashima. Retained Austenite Characteristics and Stretch-flangeability of High-strength Low-alloy TRIP Type Bainitic Sheet Steels. *ISIJ International*, 42(4):450–455, 2002.

[178] A. M. Streicher, J. G. Speer, and D. K. Matlock. Forming response of retained austenite in a C-Si-Mn high strength TRIP sheet steel. *Steel Research*, 73(6-7):287–293, 2002.

[179] H. N. Han, C. G. Lee, C. S. Oh, T. H. Lee, and S. J. Kim. A model for deformation behavior and mechanically induced martensitic transformation of metastable austenitic steel. *Acta Materialia*, 52(17):5203–5214, 2004.

[180] M. G. Lee, S. J. Kim, and H. N. Han. Crystal plasticity finite element modeling of mechanically induced martensitic transformation (MIMT) in metastable austenite. *International Journal of Plasticity*, 26(5):688–710, 2010.

[181] E. S. ROWLAND and S. R. LYLE. THE APPLICATION OF MS POINTS TO CASE DEPTH MEASUREMENT. *TRANSACTIONS OF THE AMERICAN SOCIETY FOR METALS*, 37:27–47, 1946.

[182] W. Steven. The temperature of formation of martensite and bainite in low alloy steels, some effects of chemical composition. *Journal of the Iron and Steel Institute*, 183:349–359, 1956.

[183] K. W. Andrews. Empirical formulae for the calculation of some transformation temperatures. *J. Iron Steel Inst.*, pages 721–727, 1965.

[184] D. Barbier. Extension of the Martensite Transformation Temperature Relation to Larger Alloying Elements and Contents. *Advanced Engineering Materials*, 16(1):122–127, 1 2014.

[185] Y. Sakuma, D. K. Matlock, and G. Krauss. Mechanical behavior of an intercritically annealed and isothermally transformed low C alloy steel with Ferrite-Bainite-Austenite microstructures. *Journal of Heat Treating*, 8(2):109–120, 9 1990.

[186] N. H. Van Dijk, A. M. Butt, L. Zhao, J. Sietsma, S. E. Offerman, J. P. Wright, and S. Van Der Zwaag. Thermal stability of retained austenite in TRIP steels studied by synchrotron X-ray diffraction during cooling. *Acta Materialia*, 53(20):5439–5447, 2005.

[187] E. Jimenez-Melero, N. H. van Dijk, L. Zhao, J. Sietsma, S. E. Offerman, J. P. Wright, and S. van der Zwaag. Characterization of individual retained austenite grains and their stability in low-alloyed TRIP steels. *Acta Materialia*, 55(20):6713–6723, 2007.

[188] E. De Moor, S. Lacroix, A. Clarke, J. Penning, and J. Speer. Effect of Retained Austenite Stabilized via Quench and Partitioning on the Strain Hardening of Martensitic Steels. *Metallurgical and Materials Transactions A*, 39(11):2586–2595, 11 2008.

[189] G. R. Speich, V. A. Demarest, and R. L. Miller. Formation of Austenite During Intercritical Annealing of Dual-Phase Steels. *Metallurgical and Materials Transactions A*, 12(8):1419–1428, 8 1981.

[190] E. De Moor, D. K. Matlock, J. G. Speera, and M. J. Merwin. Austenite stabilization through manganese enrichment. *Scripta Materialia*, 64(2):185–188, 2011.

[191] E. J. Seo, L. Cho, and B. C. De Cooman. Kinetics of the partitioning of carbon and substitutional alloying elements during quenching and partitioning (Q&P) processing of medium Mn steel. *Acta Materialia*, 107:354–365, 2016.

[192] C. Zhang, C. Liu, H. Guo, S. Sun, H. Chen, Y. Liu, and R. Ding. Chemical heterogeneity enables austenite stabilization in a Si-/Al-free Fe-0.2C-2Mn steel. *Scripta Materialia*, 218(March):114822, 9 2022.

[193] X. Tan, D. Ponge, W. Lu, Y. Xu, X. Yang, X. Rao, D. Wu, and D. Raabe. Carbon and strain partitioning in a quenched and partitioned steel containing ferrite. *Acta Materialia*, 165:561–576, 2019.

[194] X. Tan, D. Ponge, W. Lu, Y. Xu, H. He, J. Yan, D. Wu, and D. Raabe. Joint investigation of strain partitioning and chemical partitioning in ferrite-containing TRIP-assisted steels. *Acta Materialia*, 186:374–388, 2020.

[195] H. Bhadeshia and D. V. Edmonds. Bainite in silicon steels: new composition-property approach Part 1. *Metal Science*, 17(September):411–419, 1983.

[196] E. Girault, A. Mertens, P. Jacques, Y. Houbaert, B. Verlinden, and J. Van Humbeeck. Comparison of the effects of silicon and aluminium on the tensile behaviour of multiphase TRIP-assisted steels. *Scripta Materialia*, 44(6):885–892, 2001.

[197] H. Xue and T. N. Baker. Influence of aluminium on carbide precipitation in low carbon microalloyed steels. *Materials Science and Technology (United Kingdom)*, 9(5):424–429, 1993.

[198] V. T. T. Miihkinen and D. V. Edmonds. Tensile deformation of two experimental high-strength bainitic low-alloy steels containing silicon. *Materials Science and Technology*, 3(6):432–440, 6 1987.

[199] H. S. Park, J. C. Han, N. S. Lim, and C. G. Park. Nano-scale observation on the transformation behavior and mechanical stability of individual retained austenite in CMnSiAl TRIP steels. *Materials Science and Engineering A*, 627:262–269, 2015.

[200] N. Tsuchida, T. Tanaka, and Y. Toji. Effect of deformation temperature on mechanical properties in 1-gpa-grade trip steels with different retained austenite morphologies. *ISIJ International*, 61(2):564–571, 2021.

[201] S. v. d. Zwaag, L. Zhao, S. O. Kruijver, and J. Sietsma. Thermal and Mechanical Stability of Retained Austenite in Aluminum-containing Multiphase TRIP Steels. *ISIJ International*, 42(12):1565–1570, 2002.

[202] E. Jimenez-Melero, N. H. van Dijk, L. Zhao, J. Sietsma, J. P. Wright, and S. van der Zwaag. In situ synchrotron study on the interplay between martensite formation, texture evolution and load partitioning in low-alloyed TRIP steels. *Materials Science and Engineering A*, 528(21):6407–6416, 2011.

[203] T. Yamashita, N. Koga, and O. Umezawa. Influence of deformability of retained austenite on martensitic transformation in tension for low alloy steel at low temperatures. *ISIJ International*, 58(6):1155–1161, 2018.

[204] S. Wei, J. Kim, J. L. Cann, R. Gholizadeh, N. Tsuji, and C. C. Tasan. Plastic strain-induced sequential martensitic transformation. *Scripta Materialia*, 185:36–41, 2020.

[205] X. D. Wang, B. X. Huang, Y. H. Rong, and L. Wang. Microstructures and stability of retained austenite in TRIP steels. *Materials Science and Engineering A*, 438-440(SPEC. ISS.):300–305, 2006.

[206] Z. Xiong, A. A. Saleh, G. Casillas, S. Cui, and E. V. Pereloma. Phase-specific properties in a low-alloyed TRIP steel investigated using correlative nanoindentation measurements and electron microscopy. *Journal of Materials Science*, 55(6):2578–2587, 2020.

[207] B. B. He and S. Pan. Revealing the intrinsic nanohardness of retained austenite grain in a medium Mn steel with heterogeneous structure. *Materials Characterization*, 171(July 2020), 2021.

[208] Y. Tomota, K. Kuroki, T. Mori, and I. Tamura. Tensile deformation of two-ductile-phase alloys: Flow curves of α-γ Fe-Cr-Ni alloys. *Materials Science and Engineering*, 24(1):85–94, 7 1976.

[209] Q. Furnémont, G. Lacroix, S. Godet, K. Conlon, and P. Jacques. Critical Assessment of the Micromechanical Behaviour of Dual Phase and Trip-Assisted Multiphase Steels. *Canadian Metallurgical Quarterly*, 43(1):35–42, 1 2004.

[210] I. De Diego-Calderón, M. J. Santofimia, J. M. Molina-Aldareguia, M. A. Monclús, and I. Sabirov. Deformation behavior of a high strength multiphase steel at macro- and micro-scales. *Materials Science and Engineering A*, 611:201–211, 2014.

[211] J. H. Ryu, D. I. Kim, H. S. Kim, H. K. Bhadeshia, and D. W. Suh. Strain partitioning and mechanical stability of retained austenite. *Scripta Materialia*, 63(3):297–299, 2010.

[212] H. S. Zhao, W. Li, X. Zhu, X. H. Lu, L. Wang, S. Zhou, and X. J. Jin. Analysis of the relationship between retained austenite locations and the deformation behavior of quenching and partitioning treated steels. *Materials Science and Engineering A*, 649:18–26, 2016.

[213] X. Long, R. Zhang, F. Zhang, G. Du, and X. Zhao. Study on quasi-in-situ tensile deformation behavior in medium-carbon carbide-free bainitic steel. *Materials Science and Engineering A*, 760(February):158–164, 2019.

[214] N. Koga, T. Yamashita, and O. Umezawa. Strain Distribution and Deformation-induced Martensitic Transformation in Tension for a TRIP Steel Plate. *ISIJ International*, 60(9):2083–2089, 9 2020.

[215] F. Zhao, P. Chen, B. Xu, Q. Yu, R. D. K. Misra, G. Wang, and H. Yi. Martensite transformation of retained austenite with diverse stability and strain partitioning during tensile deformation of a carbide-free Bainitic steel. *Materials Characterization*, 179(June):111327, 2021.

[216] Y. Li, M. Wang, and M. Huang. In-situ measurement of plastic strain in martensite matrix induced by austenite-to-martensite transformation. *Materials Science and Engineering: A*, 811(December 2020):141061, 4 2021.

[217] D. Salehiyan, J. Samei, B. S. Amirkhiz, L. G. Hector, and D. S. Wilkinson. Microstructural Evolution During Deformation of a QP980 Steel. *Metallurgical and Materials Transactions A: Physical Metallurgy and Materials Science*, 51(9):4524–4539, 2020.

[218] M. M. Wang, J. C. Hell, and C. C. Tasan. Martensite size effects on damage in quenching and partitioning steels. *Scripta Materialia*, 138:1–5, 2017.

[219] E. A. A. Echeverri, A. S. Nishikawa, M. Masoumi, H. B. Pereira, N. G. Marulanda, A. M. Rossy, H. Goldenstein, and A. P. Tschiptschin. In Situ Synchrotron X-ray Diffraction and Microstructural Studies on Cold and Hot Stamping Combined with Quenching and Partitioning Processing for Development of Third-Generation Advanced High Strength Steels. *Metals*, 12(2), 2022.

[220] Y. Chang, M. Lin, U. Hangen, S. Richter, C. Haase, and W. Bleck. Revealing the relation between microstructural heterogeneities and local mechanical properties of complex-phase steel by correlative electron microscopy and nanoindentation characterization. *Materials and Design*, 203:109620, 2021.

[221] M. C. Taboada, M. R. Elizalde, and D. Jorge-Badiola. Austempering in low-C steels: microstructure development and nanohardness characterization. *Journal of Materials Science*, 54(6):5044–5060, 2019.

[222] X. Lu, W. Li, H. Zhao, and X. Jin. Local plastic indentation resistance of retained austenite in bearing steel. *ISIJ International*, 56(5):851–854, 2016.

[223] T. Man, T. Ohmura, and Y. Tomota. Mechanical behavior of individual retained austenite grains in high carbon quenched-tempered steel. *ISIJ International*, 59(3):559–566, 2019.

[224] Q. Furnémont, M. Kempf, P. J. Jacques, M. Göken, and F. Delannay. On the measurement of the nanohardness of the constitutive phases of TRIP-assisted multiphase steels. *Materials Science and Engineering A*, 328(1):26–32, 2002.

[225] B. B. He, M. X. Huang, Z. Y. Liang, A. H. Ngan, H. W. Luo, J. Shi, W. Q. Cao, and H. Dong. Nanoindentation investigation on the mechanical stability of individual austenite grains in a medium-Mn transformation-induced plasticity steel. *Scripta Materialia*, 69(3):215–218, 2013.

[226] R. Hossain, F. Pahlevani, and V. Sahajwalla. Stability of retained austenite in high carbon steel – Effect of post-tempering heat treatment. *Materials Characterization*, 149(November 2018):239–247, 2019.

[227] B. B. He and S. Pan. Correlation Between Martensitic Transformation and Strain Burst in Retained Austenite Grains During Nanoindentation Investigation. *Metals and Materials International*, 28(3):573–578, 2022.

[228] I. Timokhina, P. Hodgson, and E. Pereloma. Effect of microstructure on the stability of retained austenite in TRIP steels. *Metallurgical and Materials Transactions A*, 35(8):2331–2340, 2004.

[229] S. Zhang and K. O. Findley. Quantitative assessment of the effects of microstructure on the stability of retained austenite in TRIP steels. *Acta Materialia*, 61(6):1895–1903, 2013.

[230] A. Devaraj, Z. Xu, F. Abu-Farha, X. Sun, and L. G. Hector. Nanoscale Solute Partitioning and Carbide Precipitation in a Multiphase TRIP Steel Analyzed by Atom Probe Tomography. *Jom*, 70(9):1752–1757, 2018.

[231] Z. J. Xie, Y. Q. Ren, W. H. Zhou, J. R. Yang, C. J. Shang, and R. D. Misra. Stability of retained austenite in multi-phase microstructure during austempering and its effect on the ductility of a low carbon steel. *Materials Science and Engineering A*, 603:69–75, 2014.

[232] G. K. Tirumalasetty, M. A. Van Huis, C. Kwakernaak, J. Sietsma, W. G. Sloof, and H. W. Zandbergen. Deformation-induced austenite grain rotation and transformation in TRIP-assisted steel. *Acta Materialia*, 60(3):1311–1321, 2012.

[233] N. Clément, D. Caillard, and J. Martin. Heterogeneous deformation of concentrated NiCr F.C.C. alloys: Macroscopic and microscopic behaviour. *Acta Metallurgica*, 32(6):961–975, 6 1984.

[234] L. Wang, R. I. Barabash, Y. Yang, T. R. Bieler, M. A. Crimp, P. Eisenlohr, W. Liu, and G. E. Ice. Experimental characterization and crystal plasticity modeling of heterogeneous deformation in polycrystalline α-Ti. *Metallurgical and Materials Transactions A: Physical Metallurgy and Materials Science*, 42(3):626–635, 2011.

[235] H. J. Jeong, N. S. Lim, B. H. Lee, C. G. Park, S. Lee, S. H. Kang, H. W. Lee, and H. S. Kim. Local and Global Stress–Strain Behaviors of Transformation-Induced Plasticity Steel Using the Combined Nanoindentation and Finite Element Analysis Method. *Metallurgical and Materials Transactions A: Physical Metallurgy and Materials Science*, 45(13):6008–6015, 2014.

[236] M. I. Latypov, S. Shin, B. C. De Cooman, and H. S. Kim. Micromechanical finite element analysis of strain partitioning in multiphase medium manganese TWIP+TRIP steel. *Acta Materialia*, 108:219–228, 2016.

[237] R. Maeda, Z. L. Wang, T. Ogawa, and Y. Adachi. Stress–strain partitioning behavior and mechanical properties of dual-phase steel using finite element analysis. *Materials Today Communications*, 25(September):101658, 2020.

[238] S. T. Oh, K. K. Park, H. N. Han, S. H. Park, and K. H. Oh. In-situ deformation behavior of Retained Austenite on TRIP steel. *Materials Science Forum*, 408-412(II):1341–1346, 2002.

[239] X. C. Xiong, B. Chen, M. X. Huang, J. F. Wang, and L. Wang. The effect of morphology on the stability of retained austenite in a quenched and partitioned steel. *Scripta Materialia*, 68(5):321–324, 2013.

[240] Y. Tomota, H. Tokuda, Y. Adachi, M. Wakita, N. Minakawa, A. Moriai, and Y. Morii. Tensile behavior of TRIP-aided multi-phase steels studied by in situ neutron diffraction. *Acta Materialia*, 52(20):5737–5745, 2004.

[241] S. H. He, B. B. He, K. Y. Zhu, R. Ding, H. Chen, and M. X. Huang. Revealing the role of dislocations on the stability of retained austenite in a tempered bainite. *Scripta Materialia*, 168:23–27, 2019.

[242] E. D. Moor, J. G. Speer, D. K. Matlock, C. Föjer, I. Gent, O. Nv, J. Penning, E. De Moor, J. G. Speer, D. K. Matlock, C. Föjer, and J. Penning. Effect of Si, Al and Mo alloying on tensile properties obtained by quenching and partitioning. *Materials Science and Technology Conference and Exhibition 2009, MS and T'09*, 3:1554–1563, 1 2009.

[243] M. J. Kähkönen, E. De Moor, J. Speer, and G. Thomas. Carbon and Manganese Effects on Quenching and Partitioning Response of CMnSi-Steels. *SAE International Journal of Materials and Manufacturing*, 8(2):419–424, 2015.

[244] D. T. Pierce, D. R. Coughlin, K. D. Clarke, E. De Moor, J. Poplawsky, D. L. Williamson, B. Mazumder, J. G. Speer, A. Hood, and A. J. Clarke. Microstructural evolution during quenching and partitioning of 0.2C-1.5Mn-1.3Si steels with Cr or Ni additions. *Acta Materialia*, 151:454–469, 2018.

[245] K. Zhu, C. Mager, and M. Huang. Effect of substitution of Si by Al on the microstructure and mechanical properties of bainitic transformation-induced plasticity steels. *Journal of Materials Science and Technology*, 33(12):1475–1486, 2017.

[246] K. Zhu, H. Shi, H. Chen, and C. Jung. Effect of Al on martensite tempering: comparison with Si. *Journal of Materials Science*, 53(9):6951–6967, 2018.

[247] D. Tjahjanto, A. Suiker, S. Turteltaub, P. Rivera Diaz del Castillo, and S. van der Zwaag. Micromechanical predictions of TRIP steel behavior as a function of microstructural parameters. *Computational Materials Science*, 41(1):107–116, 11 2007.

[248] P. J. Jacques, F. Delannay, and J. Ladrière. On the influence of interactions between phases on the mechanical stability of retained austenite in transformation-induced plasticity multiphase steels. *Metallurgical and Materials Transactions A*, 32(11):2759–2768, 11 2001.

[249] H. Toda, A. Takijiri, M. Azuma, S. Yabu, K. Hayashi, D. Seo, M. Kobayashi, K. Hirayama, A. Takeuchi, and K. Uesugi. Damage micromechanisms in dual-phase steel investigated with combined phase- and absorption-contrast tomography. *Acta Materialia*, 126:401–412, 2017.

[250] M. Calcagnotto, D. Ponge, and D. Raabe. Effect of grain refinement to 1μm on strength and toughness of dual-phase steels. *Materials Science and Engineering A*, 527(29-30):7832–7840, 2010.